

DISSERTATION

THIN FILM INTEGRATED OPTICAL WAVEGUIDES FOR BIOSENSING USING LOCAL
EVANESCENT FIELD DETECTION

Submitted by

Matthew David Stephens

Department of Chemical and Biological Engineering

In partial fulfillment of the requirements

For the Degree Doctor of Philosophy

Colorado State University

Fort Collins, Colorado

Spring 2010

COLORADO STATE UNIVERSITY

August 26, 2009

WE HEREBY RECOMMEND THAT THE DISSERTATION PREPARED UNDER OUR SUPERVISION BY MATTHEW DAVID STEPHENS ENTITLED THIN FILM INTEGRATED OPTICAL WAVEGUIDES FOR BIOSENSING USING LOCAL EVANESCENT FIELD DETECTION BE ACCEPTED AS FULFILLING IN PART REQUIREMENTS FOR THE DEGREE DOCTOR OF PHILOSOPHY.

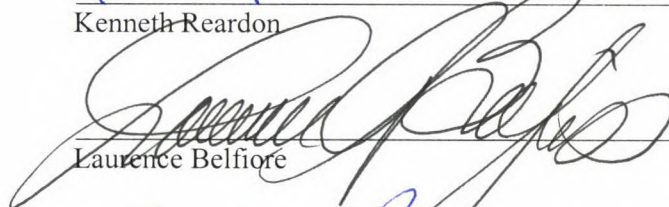
Committee on Graduate work



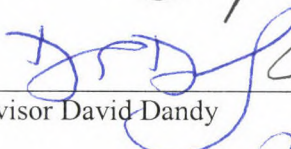
Kevin Lear



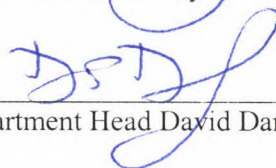
Kenneth Reardon



Laurence Belfiore



Advisor David Dandy



Department Head David Dandy

ABSTRACT OF DISSERTATION
THIN FILM INTEGRATED OPTICAL WAVEGUIDES FOR BIOSENSING USING LOCAL
EVANESCENT FIELD DETECTION

A waveguide is a high refractive index material that is surrounded by lower refractive index cladding. This waveguide structure can be used to carry light confined to the high refractive index core. Surrounding the core of the waveguide is a decaying evanescent light field that extends into the cladding layers. The intensity profile of the evanescent field is dependent on the refractive index of the cladding. The changes in the local intensity of the evanescent field can be used to detect refractive index changes near the core of the waveguide.

A high refractive index film deposited on a flat, low refractive index substrate can be used to form a waveguide with a planar geometry. The planar design allows the upper cladding refractive index to be modified by attaching proteins or patterning organic films. This design also allows the evanescent field intensity to be measured using near field scanning optical microscopy or a silicon photo detector array.

The fabrication and characterization of a waveguide device with a coupled light source was accomplished. The evanescent field response to thin films of patterned photoresist was found using NSOM. Light intensity measured at the surface of the sample showed significant response to the presence of the photoresist features. Light response to a protein affinity assay was found and results indicated that protein concentration could be inferred from local evanescent field measurements. A buried silicon photo detector was fabricated and characterized. The results show the field responds in a significant matter to uniform and pattered features on the waveguide core.

Matthew David Stephens
Department of Chemical and Biological Engineering
Colorado State University
Fort Collins CO, 80523
Spring 2010

Acknowledgements

This work was supported by the National Institute of Health grant number EB00726. The author would like to thank his advisor, David Dandy and committee members Kevin Lear, Kenneth Reardon, and Laurence Belfiore for their help with this project. The author would like to thank Guangwei Yuan and Rongjin Yan who were graduate students in the Colorado State University (CSU) Electrical and Computer Engineering (ECE) department for their collaborative help with the BeamPROP simulations. The author would like to thank Larry Rea and Holly Cross from Inverness Medical Professional Diagnostics (formerly of ThermoElectro Biostar) for their help with silicon nitride deposition. The author would also like to thank the following people for their assistance:

- Xinya He and Brian Murphy – Immunoassay patterning
- Ahmad N. Al-Omari – CSU buried detector mask drawing
- Phil Nikkel and co-workers – Avago buried detector device fabrication
- Tom Chen, Charles Thangaraj, Bob Pownall and David Sehart – ECE students and faculty who assisted with device fabrication or lent materials to this project

Table of Contents

ACKNOWLEDGEMENTS	1
TABLE OF CONTENTS	2
CHAPTER 1 – AFFINITY CHEMISTRY AND EVANESCENT FIELD DETECTION	4
1.1 INTRODUCTION AND MOTIVATION	4
1.2 AFFINITY CHEMISTRY	5
1.3 IMMUNOASSAYS	6
1.4 IMMUNOASSAY MICROARRAYS	8
1.5 LEAC SENSOR CONCEPT	9
1.6 WAVEGUIDE OPTICAL THEORY	11
1.7 ANALYTE DETECTION METHOD	12
1.8 PLANAR WAVEGUIDES	13
1.9 EVANESCENT FIELD DETECTION	15
1.10 RESEARCH AIMS	17
CHAPTER 2 – OPTICAL WAVEGUIDES	20
2.1 LEAC WAVEGUIDES	20
2.2 THE EVANESCENT FIELD	20
2.3 DEPOSITION OF THE NITRIDE FILM	23
2.4 PROTOTYPE WAVEGUIDE DESIGNS	23
2.5 NEAR FIELD SCANNING OPTICAL MICROSCOPY (NSOM)	28
2.6 WAVEGUIDE GEOMETRY AND MODES	30
2.7 FABRICATION SUMMARY	31
2.8 CONCLUSION	36
CHAPTER 3 – FEATURES ON THE WAVEGUIDE	37
3.1 FABRICATION OF HIGH INDEX FEATURES ON THE WAVEGUIDE SURFACE	37
3.2 S/N AND POWER MODULATION FOR NSOM RESULTS.....	37
3.3 NSOM RESULTS FOR HIGH REFRACTIVE INDEX FEATURES	39
3.4 NUMERICAL SIMULATION OF FIELD RESPONSE TO HIGH REFRACTIVE INDEX FEATURE.....	44
3.5 SUMMARY OF EXPERIMENTAL RESULTS FOR HIGH REFRACTIVE INDEX FEATURES	44
3.6 EVANESCENT FIELD RESPONSE TO PHOTORESIST FEATURES	46
3.7 CREATING THE PHOTORESIST FEATURES ON THE WAVEGUIDE	47
3.8 MEASURING LIGHT RESPONSE	48
3.9 MODELING FIELD DISTRIBUTION USING THE BEAM PROPAGATION METHOD.....	50
3.10 RESULTS AND DISCUSSION.....	50
3.11 CONCLUSION	57
CHAPTER 4 – PROTEIN IMMUNOASSAY ON THE WAVEGUIDE	59
4.1 INTRODUCTION	59
4.2 PROTEIN CONCENTRATION ASSAY USING EVANESCENT FIELD RESPONSE.....	60
4.3 WAVEGUIDE FABRICATION.....	62
4.4 IMMUNOASSAY PATTERNING	62
4.5 NSOM OF PROTEIN PATTERNS	63
4.6 EVANESCENT FIELD RESPONSE	64
4.7 CONCLUSION	69

CHAPTER 5 – BURIED DETECTOR SENSING	70
5.1 ON CHIP EVANESCENT FIELD DETECTION	70
5.2 BURIED DETECTOR CONCEPT	70
5.3 CSU DETECTOR ARRAY FABRICATION.....	73
5.4 CSU DETECTOR RESPONSE	77
5.5 AVAGO DETECTOR DESIGN	82
5.6 RESULTS FROM AVAGO DETECTOR.....	83
5.7 CONCLUSION	84
CHAPTER 6 – CONCLUSIONS AND FUTURE WORK	85
6.1 INTRODUCTION.....	85
6.2 WAVEGUIDE DESIGN	85
6.3 EVANESCENT RESPONSE TO CORE THICKNESS CHANGES.....	87
6.4 EVANESCENT RESPONSE TO PATTERNED POLYMER FEATURES.....	88
6.5 QUANTITATIVE IMMUNOASSAY	90
6.6 ON-CHIP EVANESCENT DETECTION	91
6.7 BURIED DETECTOR IMPROVEMENTS	92
6.8 WAVEGUIDE MODIFICATIONS	94
6.9 DEVICE IMPROVEMENTS.....	95
6.10 CONCLUSION	97
6.11 FURTHER EXPERIMENTS	97
REFERENCES	99
APPENDIX A: CLEANROOM PROCEDURES	106
A.1 LITHOGRAPHY FOR WAVEGUIDE FABRICATION.....	106
A.2 MICRO RIE ETCHING	108
APPENDIX B: MATLAB CODE	110
B.1 DATA PLOTTING AND BACKGROUND SUBTRACTION USING MATLAB	110
B.2 POWER MODULATION CALCULATION CODE.....	111
B.3 NOISE AND S/N CALCULATION CODE.....	112
B.4 CALCULATION OF LIMIT OF DETECTION	113

Chapter 1 – Affinity chemistry and evanescent field detection

1.1 Introduction and Motivation

The work described in this dissertation involves the fabrication of a novel biosensor device based on using affinity chemistry as a selective sensing technique. An optical method to determine binding between probe and analyte was employed. This optical technique detects binding of the target analyte directly by using local evanescent array coupled (LEAC) detection of the light field surrounding the core of a thin, planar waveguide (see Figure 1.1). A waveguide device confines and guides light through total internal reflection using a refractive index difference between a core

region of high refractive index and cladding region(s) that have lower refractive index. The approach here is reagentless, such that the binding events are detected without the use of any fluorescent tags or radiolabels. The evanescent wave around the core of the waveguide shifts spatially in response to the binding between probes immobilized

on the surface and targets (analytes) in the solution above the waveguide. Previous research has

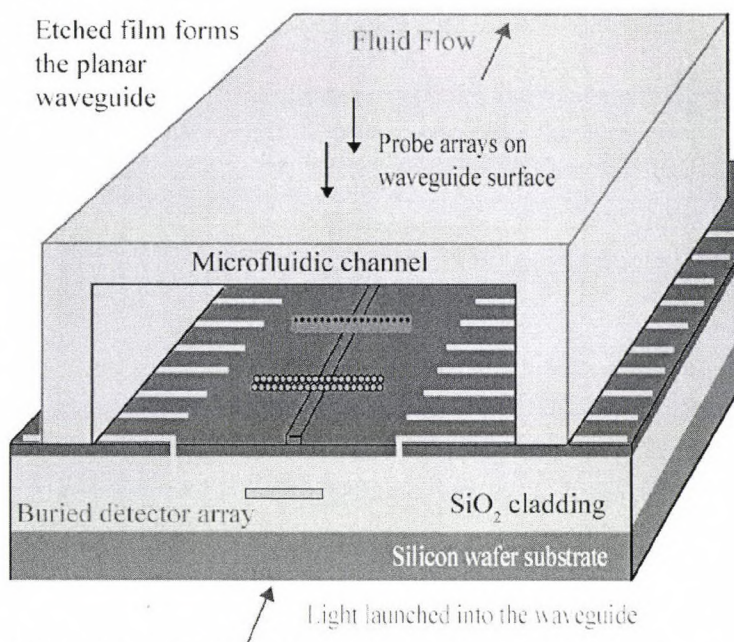


Figure 1.1: LEAC sensing device. Waveguide built on a wafer with buried detector array for real-time detection of local evanescent field changes due to analyte binding to probe regions. Poly(dimethylsiloxane) microfluidic network allows a liquid sample to contact the probe regions.

shown that DNA and antibodies or other proteins can be used to capture specific analytes [1-15]. There are capture regions on these molecules that can specifically bind to only one type or a small number of types of target molecules. This specificity of binding between these species can be used to form a sensor to detect these target molecules. A flat surface area can be used to immobilize these capture molecules or probes in regions as small as 10 to 20 μm in diameter. Multiple, distinct probe regions can be patterned on the surface to form a sensor that can bind multiple types of analytes. However, the binding between the attached probes and the analytes in solution must be quantified. The evanescent field surrounding the core of a planar optical waveguide is sensitive enough to respond to the binding events and can be quantified accurately to determine the initial concentration of each analyte. The following sections will introduce affinity chemistry and optical waveguide design and explain the advantages that make the combination of the two an effective biosensing concept.

1.2 Affinity chemistry

An example of affinity chemistry is the antibody/antigen interaction. Antibodies are molecules that are part of an immune system that have specific binding pockets called epitopes. These epitopes are a series of amino acids that form a unique binding structure that will specifically bind with an infection generating agent like a flu virus or other pathogenic or mutagenic molecule. If the epitope will bind to one specific type of antigen (antibody generator), the antibody is called monoclonal. If a larger class of molecules will bind with the antibody, the antibody is a polyclonal antibody. An example of a monoclonal antibody would be an antibody that would preferentially capture *E. coli* O157:H7 out of a solution. However if the antibody would bind with any type of *E. coli*, it would be polyclonal. There are other proteins that can form a probe/analyte pair that can be used in affinity binding. For example, a protein pair that is used in linking chemistry is the avidin/biotin interaction. Avidin has four binding sites that can each bind one of the smaller biotin molecules. Also, affinity binding takes place between a strand of nucleic acid base pairs and its complementary strand. Any of these specific binding

interactions can be used to form a sensing device that is able to capture one or more target molecules from a mixture of similar species. Therefore, affinity binding chemistry is any binding mechanism where one probe specifically prefers to bind to one analyte type or one class of analytes. This sensor uses affinity chemistry as a selective capture technique and any number of pairs of probes/analytes can be incorporated into the design in order to form tests for the particular molecules.

1.3 Immunoassays

Many analytical tools have been developed that use antibody-antigen interactions called immunoassays [6-13]. Immunoassays can detect any chemical, protein, polysaccharide, or pathogen that causes an immune response in a human or animal [14]. When an animal or human experiences an immune response, the antibodies that have been produced in the blood specifically attach to the antigen and label it for destruction by white blood cells [15]. The phenomenon exploited by the various immunoassays demonstrates this fact: the monoclonal antibody will only bind to one specific chemical, protein, polysaccharide, or pathogen [16]. The primary difference between the various immunoassays is the way the different tests determine when an antibody/antigen binding event has occurred. Some of the most common ways to detect an antibody-antigen binding event include color change of a test surface [17], colored solution [18], or expression of a fluorescing molecule [9].

The use of monoclonal antibodies (antibodies that will bind to only one fairly specific type of analyte) as an analytical method for determining the presence of a specific antigen has been well established. There have been kits available to carry out Enzyme-Linked ImmunoSorbant Assays (ELISA) for a number of years [19]. There are two different ways to determine the concentration of a particular antigen using an ELISA test. The first method shown in figure 1.2 [20] is called the sandwich assay. It is called this because two antibodies bind to the antigen. One antibody is attached to the well and the other is labeled with an enzyme and attaches to the bound antigen. This assay is for antigens that are large enough to have two epitopes that

will easily allow two antibodies to bind to the antigen. An epitope is the area of an antigen molecule that binds with an antibody and is also known as the antigenic determinant site [21].

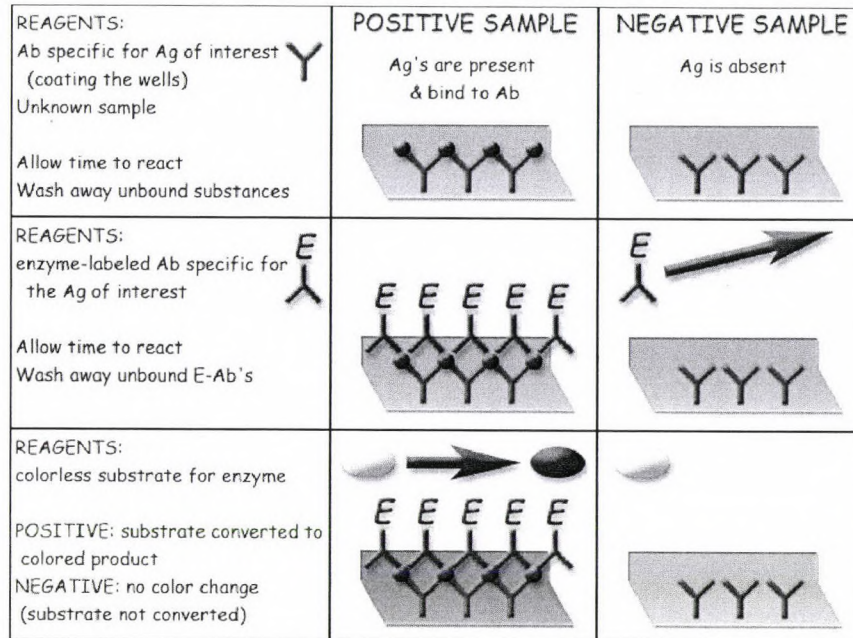


Figure 1.2: Binding steps for a specific immunoassay test called the sandwich ELISA. Antigens bind to antibodies attached to a solid surface (top). Enzyme linked antibodies are added and form a sandwich by binding with captured antigen (middle). Substrate is added that reacts with the enzyme to cause a color change that is proportional to antigen concentration (bottom) [20].

The second type of ELISA that is used to detect analytes is shown in Figure 1.3 [22].

This type is called the competitive binding assay. It is called this because any antigen in the unknown sample must compete with enzyme labeled antibodies that are added to the test. The particular benefit of this assay is for the detection of small antigens that have only one epitope or have closely spaced epitopes. The competitive binding format is also able to detect small concentrations of antigen.

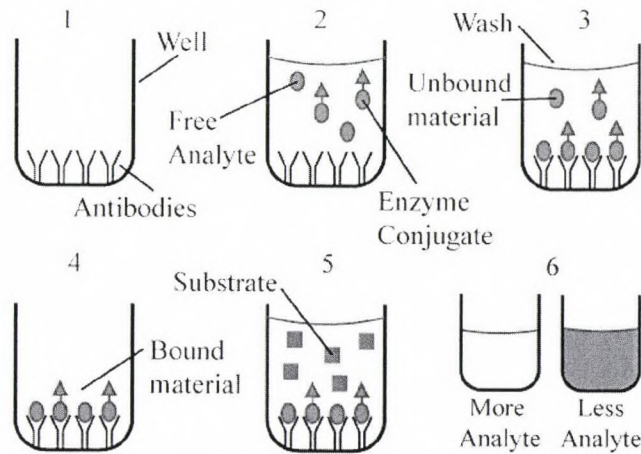


Figure 1.3: Competitive Binding ELISA. 1) Antibodies are attached to the well surface. 2) Sample solution is introduced containing possible analyte and enzyme labeled analyte. 3) The analyte in the sample solution competes for binding locations with the labeled analyte. 4) The well is rinsed to remove any unbound material. 5) Substrate is added, which reacts with the enzyme linked analyte. 6) Degree of color change is inversely proportional to sample analyte concentration [22].

The shortcomings of the ELISA test are that it may take 1 to 2 hours to run, it tests for a single analyte, needs an absorbance spectrophotometer to quantify results, and requires specific labeled reagents. If different antibodies were covalently attached in regions on a plate then the test would be multi-analyte. If the specific binding properties of antibodies could be used in a multi-analyte assay employing a label free binding detection mechanism, the test would be much more versatile.

1.4 Immunoassay Microarrays

An improvement to the design of the ELISA tests are the various immunoassays that use antibodies covalently attached to a thick-film waveguide and using the sandwich assay with antibodies labeled with fluorescent tags. An example of this type of system is shown in Figure 1.4 and is representative of the different designs produced by the researchers at the Center for Bio/Molecular Science and Engineering located at the Naval Research Laboratory [25]. This biosensor is based around a glass cover slip that functions as a thick waveguide. Several types of antibodies are patterned on the cover slip and light is coupled into it. The resulting evanescent field provides the excitation for the labeled antibodies. Fluorescent emission from the waveguide surface is focused by a graded index lens array (GRIN) through optical filters onto a Peltier-

cooled CCD imaging array. This system does have multi-analyte capability but it also has the disadvantage of requiring the addition of antibodies that have fluorescent tags in order to recognize antigen/antibody binding events. In addition, for small antigens, the sandwich method does not

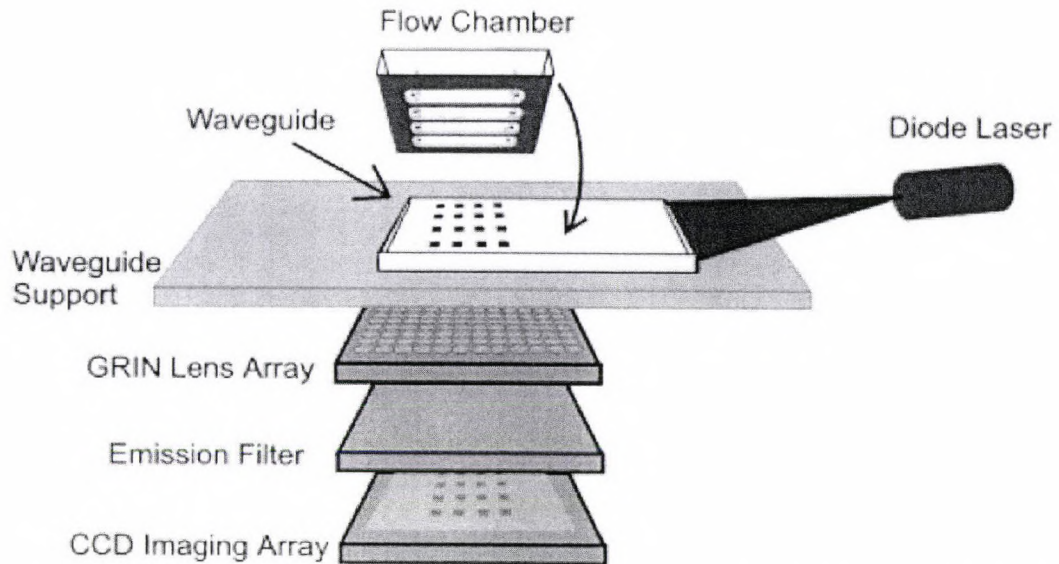


Figure 1.4: Immunoassay based on fluorescently labeled antibodies and the sandwich assay. Sample is confined to the surface using PDMS channels and fluorescent excitation is caused by light in a glass slide functioning as a thick slab waveguide. Analyte concentration is measured by detecting fluorescence with a CCD element [25].

exhibit good performance and the reagents would need to be changed to operate on a competitive binding assay format.

1.5 LEAC sensor concept

The technique of spatially patterning antibodies has been established [23-25]. However, the detection technique used in this research to identify probe/analyte binding events has not been incorporated into any known biosensor device. This new detection method is based on measuring the changes in the evanescent wave field intensity surrounding the core of an optical waveguide. When light is guided down an optical fiber or planar waveguide by total internal reflection, the electromagnetic field intensity does not immediately drop to zero at the core/cladding interface. A small amount of the light escapes the surface and, if not coupled away, exists outside the waveguide core. This field of light outside of the core is called the evanescent wave field. For a

very thin waveguide, most of the optical energy is contained in the evanescent field. For a waveguide with a thickness of 100 nm, the exponentially decaying evanescent field extends approximately 1 μm into the cladding layer. The evanescent field profile depends on several factors including the thickness of the core, the indices of refraction of the core and cladding regions, as well as the wavelength of the propagating light. Therefore, by correlating the evanescent field strength with refractive index changes in the upper cladding, the presence of captured analyte can be detected and the extent of filled antibody-antigen binding sites can be determined. From this information, the concentration of the desired analytes in the original sample can be found.

The optical waveguide developed in this study consists of core optical films 50 to 100 nm thick in original designs with attached regions of different specific capture probes sensitive to various analytes of relevance and practical interest (see figure 1.5). The waveguide is contained in a fluid reservoir that serves as a method for introducing the test analyte as well as acting as the optical cladding layer on the upper

surface of the waveguide. Coupled light is guided down the core and through any immobilized probe layers. The adjacent aqueous phase has a lower refractive index, $n_f=1.33$, causing total internal reflection of the light. However, evanescent, non-propagating optical fields tail out exponentially into the cladding

outside the waveguide core and can be detected by introducing higher index probes that intercept the non-propagating optical field and guide it to external photodetectors. One example of such a

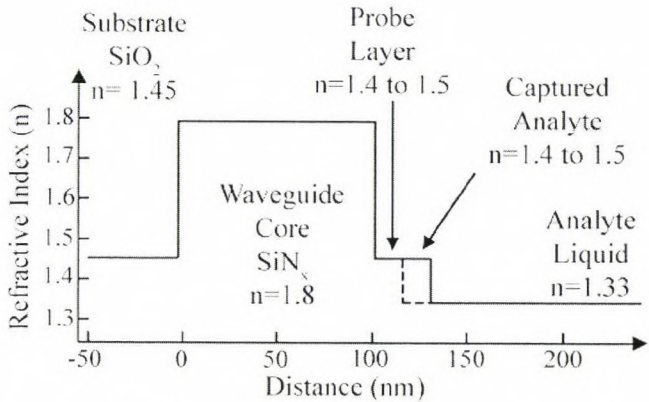


Figure 1.5: Refractive index profile for an asymmetrical silicon nitride waveguide on silicon dioxide with attached probe & analyte.

detection apparatus is a near-field scanning optical microscopy (NSOM) tip. More conventional detection utilizes common solid-state arrays (CCDs) and other photosensitive solid-state devices.

When analyte binds to the attached capture layer, the thickness of the organic layer effectively increases by 5 to 20 nm or more depending on the type of analyte. Since the bound antibody-analyte layer's typical refractive index of $n_p = 1.45$ is higher than the surrounding fluid, it combines with the optical film to function as the waveguide core. The field strength in the cladding is a function of the refractive indices of all the layers and the thickness of the core layers. Specifically, adsorption of the analyte layer increases the effective core thickness, reducing the penetration of the evanescent optical fields into the adjacent fluid regions. Thus, changes in the penetration of the optical fields into the fluid can be sensed to determine the presence or absence of specific analytes. By monitoring changes in the evanescent field penetration surrounding each region of immobilized antibodies, a number of analytes can be detected and quantified simultaneously.

1.6 Waveguide Optical Theory

Light propagating down a planar waveguide does so by total internal reflection. If the angle at which the light strikes the internal surface of the waveguide is less than the critical angle θ_c then all of the light is reflected as shown in figure 1.6. If the angle is greater than the critical angle, then some of the light escapes the core of the waveguide. The critical angle is determined by the refractive index of the waveguide core (n_1) and the refractive index of the cladding (n_2) according to the relationship:

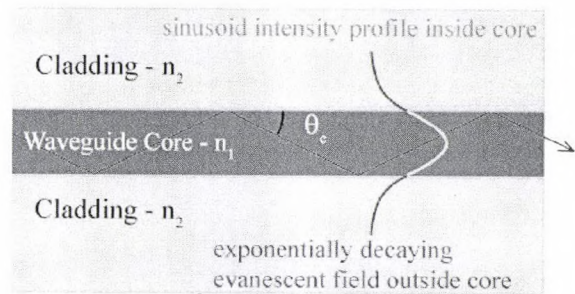


Figure 1.6: Total internal reflection in a symmetrical waveguide showing light power profile inside the core and the cladding evanescent field.

$$\theta_c = \sin^{-1} \left(\frac{n_2}{n_1} \right) \quad \text{Equation 1.1}$$

Using this scheme, waveguides can transmit light over long distances with very little loss in intensity [26]. Simultaneous with the light's reflection off the internal surface of the waveguide is the creation of an electromagnetic field at the surface of the core. This field extends into the surrounding media and is called the evanescent wave. The intensity of the field decays exponentially with distance from the surface of the core. The effective distance this field penetrates into the external cladding is usually less than one wavelength of light and is very sensitive to the incident angle θ_c , the refractive indexes of the core (n_1) and the cladding (n_2).

For planar or cylindrical waveguides, the light can travel down the waveguide in different modes depending on the dimensions of the waveguide [27]. A mode is the spatial distribution of optical energy in one or more dimensions. Based on the wavelength of light, material indices of refraction, and dimensions of the waveguide, the mode that will be propagating through the waveguide with index profile shown in figure 1.5 will be the first order transverse electric (TE) mode [28]. This distribution of light intensity with location is shown superimposed on the symmetrical waveguide shown in figure 1.6. The light intensity profile follows a sine curve inside the core and evanescent light field in the cladding regions exponentially decays to zero.

1.7 Analyte Detection Method

The most common example of a waveguide is a fiber optic cable (see figure 1.7). The largest application for fiber optic cables is the telecommunications industry. A telecom fiber has a cylindrical geometry made of a plastic coated glass fiber. The mode(s) of light propagation are determined by the fiber core size and refractive index difference between the core and cladding. A mode of light propagation is a particular electromagnetic profile that is carried with

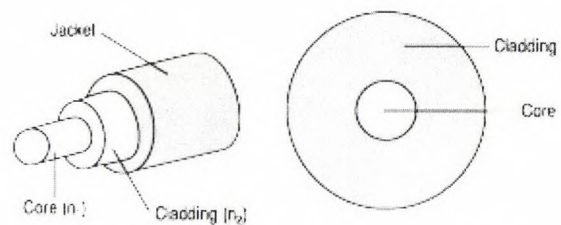


Figure 1.7: Basic fiber optic cable geometry showing a high refractive index cylindrical core surrounded by cladding and a plastic jacket [27]

low attenuation down the core of the waveguide. If a single mode of light propagation is desired,

the light will be distributed with the highest intensity at the center of the core. The single mode glass fiber has a 4 to 10 μm core depending on the guided wavelength, with 1310 nm or 1550 nm being typical wavelengths used in the telecom industry [27]. For a single mode fiber guiding visible wavelengths, the core must be smaller than for the longer wavelengths used for communications. To expose the evanescent field for sensing purposes, a section of the fiber optic cable can be heated so the glass is melted. The heated portion of the cable is then stretched which thins the glass fiber and thereby exposes the evanescent field. The field can then interact with the air or solution surrounding the fiber. This is one technique whereby the evanescent field can provide a source for fluorescence excitation, but measuring the spatial intensity shift of the field locally is difficult because of the delicacy of the construction and the cylindrical nature of the fiber.

1.8 Planar waveguides

A second common geometry of waveguide is the planar waveguide. The refractive index differences between the core and cladding are typically larger than for optical fibers and the light is guided down a square or rectangular core rather than a cylindrical fiber. This thin-film, planar format has several benefits over other geometries:

- 1) Having the waveguide core built on a wafer makes it easier to pattern regions of probes on specific areas of a flat surface using microfluidic channels, contact printers, or inkjet printers.
- 2) A microfluidic network can be used to bring the sample solution to the attached probes.
- 3) The waveguide geometry can be designed to modify the evanescent field penetration distance into the cladding so binding interactions can be measured with high sensitivity.

In the studies described in this dissertation, the waveguide design that was determined to have the best geometry for this sensor was planar and guides single

wavelength light that is in the visible range (654 nm). To create a waveguide, a film of non-stoichiometric silicon nitride with a refractive index of approximately 1.8 was deposited on top of a thermal oxide wafer as shown in figure 1.8. Silicon nitride is a linear optical material transparent to light of wavelengths in the visible range. The thermal oxide formed the lower cladding

($n=1.45$) and optically shielded the waveguide core from the silicon substrate

($n=2.1$). For the structure to form a

waveguide there must be a region of high refractive index material surrounded by lower index cladding material. Therefore, the thermal oxide wafer with a surface refractive index of 1.45 was coated with a film of refractive index of 1.8. On top of the film was air ($n=1.0$) or aqueous solution ($n=1.33$) or attached proteins ($n=1.4-1.5$). This structure will always guide one or more modes of light. Using a bulk film as a waveguide is not a convenient geometry unless the evanescent field is only used for fluorescent excitation. But in this case a localized waveguide was desired to simplify the evanescent field measurement. So a 2 to 5 μm wide ridge was fabricated by partially etching the film so the light was confined horizontally and guided only in the ridge area. This geometry also reduced the number of horizontal and vertical propagating modes. The light was guided with a higher intensity in the ridge area and the probe regions were placed on the ridge waveguide so the evanescent field was able to come into contact with as much of the binding area as possible.

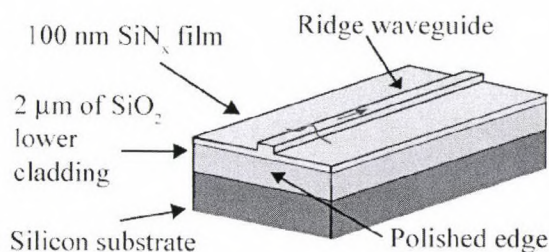


Figure 1.8: An asymmetrical 2 μm wide, planer ridge waveguide fabricated on a thermally oxidized silicon wafer.

When local binding events take place within the evanescent field above the core, the refractive index of the upper cladding next to the core changes due to the displacement of the fluid in the upper cladding by the bound analytes. The field adjusts to a new intensity profile as

the refractive index changes. These binding events form an additional self assembled layer (adlayer) on the surface of the core. Capturing the analytes using affinity binding is only half of the sensor. Changes in the evanescent field distribution must be detected to find where the shifts (if any) have taken place. If the field profile has changed and that change can be detected, the binding events can be measured without using any additional reagents or enzyme/nano-particle/radioactive/magnetic/fluorescent labels. The degree of spatial shift in the evanescent field intensity depends on the refractive index changes in the upper cladding. With very small analytes the adlayer thickness due to binding will not change significantly but the small molecules will still cause a refractive index change by displacing fluid near the surface. Thus this sensing technique would result in a greater detected signal when the analyte for detection was a protein rather than a low molecular weight amino acid or environmental contaminate such as toluene. If the sensing of small molecules was necessary, the evanescent field detection method could be used to observe the results from a competitive affinity assay using labeled analyte.

1.9 Evanescent field detection

To detect and measure the evanescent field intensity, near field scanning optical microscopy (NSOM) may be used to scan the surface and measure the evanescent field intensity and surface topography (figure 1.9). Benefits of using NSOM are:

- 1) The tip collects light from a ~100 nm aperture and the scan resolution is lower than the diffraction limit of visible light. In these studies the intensity was measured several times per micron so very detailed images of the evanescent field can be acquired.

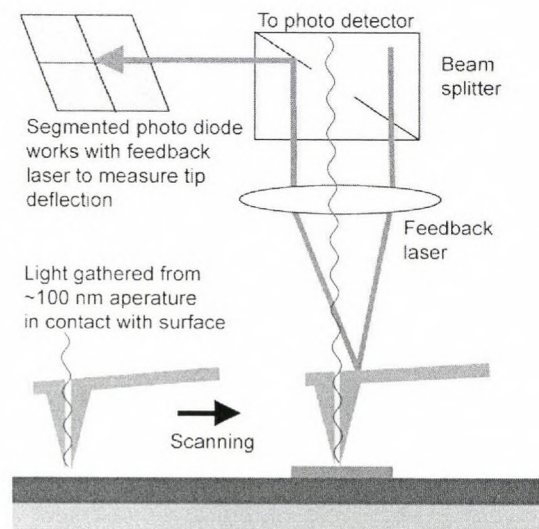


Figure 1.9: NSOM device measures topography and light intensity by scanning a tip with a 100 nm aperture across the surface of the sample.

- 2) The topography of the sample is measured at the same time as the light intensity.
- 3) A 100 μm length of the waveguide was scanned in ~ 5 min.

Disadvantages of using NSOM are:

- 1) The NSOM is an expensive and bulky laboratory instrument and must be on an air table and connected to a computer.
- 2) The NSOM tip must be in contact with the surface therefore any microfluidic network over the waveguide must be removed and the waveguide must be dry.
- 3) The tip scanning on the surface can also damage patterned regions or captured analyte.

An alternate way the evanescent field

profile is measured is using a buried detector array. The detector array was fabricated under the waveguide in the lower cladding on the waveguide chip. The benefits of this method were that the detectors measure the evanescent field at a constant distance away from the center of the waveguide core. Since the evanescent light field decays exponentially with distance into the cladding, moving the NSOM tip away from the surface results in lower detected power. Since the NSOM tip

measures topography and field intensity via

surface contact, the tip moves away from the waveguide due to changes in surface topography. Measuring at a constant distance from the core with a buried detector array would reduce the chance that these topography effects would have secondary effects on the detection of a spatial shift in the field intensity. The distance between the core and detector array can be optimized to

increase sensitivity to changes in surface refractive index changes. An additional advantage with

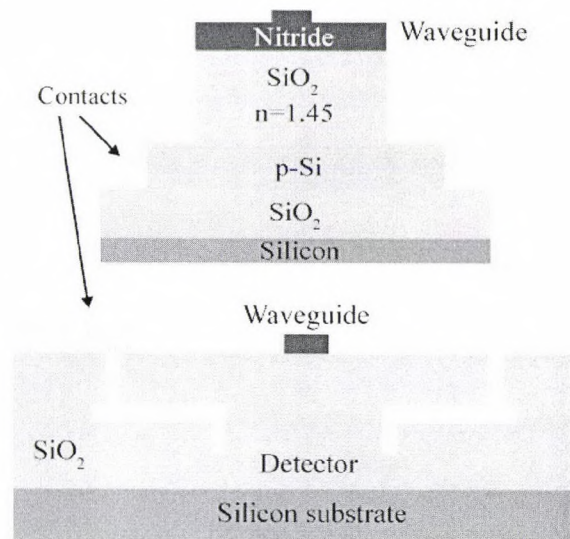


Figure 1.10: Cross section of two buried detector designs. (top) Uniform polysilicon detector strip fabricated at the CSU cleanroom, and (bottom) Avago detector design with isolated 9.5 μm long detector blocks.

a detector array is with the appropriate circuitry, the light field for the whole length of the waveguide can be measured in real time as sample is introduced on the waveguide surface. The disadvantage of using a buried detector array is the resolution of the field measurement. Typical detector devices (figure 1.10) measure the field at 10 μm to 100 μm intervals down the length of the waveguide. The detectors also absorb more of the power from the waveguide than NSOM. The amount of light launched into the waveguide must increase in order to have the same propagation distance as for a sample with no buried detector array.

In general, to detect an analyte, the evanescent field profile of the waveguide is measured before the analyte is allowed to bind to the probe region. Then after binding, the light profile is measured again to determine if there is a shift in the field. If a shift is observed, then the quantity of analyte can be calculated by using a standard response curve for that analyte. So detection of a response would indicate the presence of an analyte and degree of shift would help determine the amount of analyte. Since the response for separate probe regions can be determined, the presence and concentration of several analytes can be determined at the same time for one sample. Detecting the spatial shift in the evanescent field intensity is a more direct way of measuring analyte concentration and avoids the use of any fluorescent tags, added reagents or sample preparation.

1.10 Research aims

The aims of this research that will be addressed in this dissertation are:

1. Establish a theoretical background for a method for reagentless detection of affinity binding using evanescent field shifting.
2. Determine the optimal method for interrogation of the evanescent field for detecting small shifts in intensity due to upper cladding refractive index changes.
3. Develop a functional prototype device based on a planar optical waveguide with patterned micro-scale probe regions specific for a relevant analyte incorporating an evanescent field detection method.

As an effort to accomplish the preceding three aims, the following questions and variables pertaining to this sensor will be addressed:

Optimal waveguide design: What waveguide geometry results in single mode propagation of light? Using NSOM and buried detector arrays, what are the evanescent field intensity profiles for single mode propagation of light in a ridge waveguide? What are the challenges for attaching proteins to the waveguide surface using PDMS microfluidic channels? How well do numerical simulations compare with the measured results using NSOM and the buried detector designs? What are the observed surface and buried detector light field profiles when different features are attached to the top of the waveguide?

Light response to the following features will be examined:

1. High refractive index features fabricated with the same refractive index as the core material.
2. Polymer features made of a photoresist film that approximate the refractive index profile of biological features
3. A multilayer protein immunoassay using two concentrations of C-reactive protein with a negative control

For the preceding features, the effect of the thickness, length, and spacing of the features will be considered to determine the limits of detection and the geometry parameters for a quantitative sensor. The thickness studies will help determine the smallest analytes that can be detected using the shifting of the evanescent field. Determining the response to differing lengths of features will help the design of capture regions for optimal sensitivity while providing a significant signal for detection. Spacing of the features effects interference between adjacent capture areas and the maximum number of analytes that can be detected for an active waveguide.

In chapter 2 the basics of waveguide design and the phenomenon associated with the detection method will be discussed. In chapters 3 and 4 the response of the light field to fabricated and patterned features as measured using NSOM will be presented. Chapter 5 contains

information about buried detector design, fabrication and some results that characterize the response of the detectors. Chapter 6 concludes the dissertation and presents some areas for future improvement of the sensor device.

Chapter 2 – Optical Waveguides

2.1 LEAC Waveguides

This chapter describes the fabrication and characterization of sub-micron thickness planar, optical waveguides for application to the local evanescent array coupled (LEAC) device. The planar waveguide was fabricated out of silicon nitride deposited with a reaction ion sputter deposition. The films were characterized using AFM (atomic force microscopy), ellipsometry and XPS (x-ray photoelectron spectroscopy). The optimal design of the waveguide was determined for single mode light propagation and the surface evanescent field intensity was determined using NSOM.

2.2 The Evanescent field

The light propagated by a symmetrical waveguide is carried in two spatial regions. Inside the core the intensity profile fits a sine curve with the peak intensity in the center of the waveguide core. The remainder of the guided power travels outside the core in the evanescent wave. The surface intensity of the evanescent wave matches the power just inside the core but then decays exponentially to zero at an infinite distance from the core. The evanescent field penetration depth (d_p) into the cladding regions is defined as the distance when the power drops to $1/e$ of the power level at the edge of the core. The penetration depth is defined as:

$$d_p = \frac{\lambda}{2\pi\sqrt{n_1 \sin^2 \theta - n_2^2}} \quad \text{Equation 2.1}$$

where λ is the wavelength of the propagating light, n_1 and n_2 are the refractive indices of the core and the cladding respectively θ is the angle of illumination in the core and the quantity $n_1 \sin^2 \theta$ is the effective index of the waveguide mode.

Figure 2.1 shows two symmetrical waveguides with different core thicknesses (d). The thinner the core ($d \rightarrow 0$), the larger amount of the field is contained outside the core and the evanescent field will have a larger penetration depth. The term symmetrical indicates that the cladding has the same refractive index on each side of the core. The planar waveguide device pictured in figure 2.2 is an asymmetrical waveguide, therefore the evanescent field profiles are not uniform as for a symmetrical system. However, the same trends apply when changing the core thickness, cladding refractive indices or the wavelength of propagating light. The upper cladding for the waveguide shown in figure 2.2 is the air or water that contains the binding events that are detected. The lower cladding is SiO₂ on a silicon wafer that is used as a substrate for the deposition of the film that makes up the core of the waveguide. Changes can be observed in the amount of evanescent field penetration as the core thickness is changed. As the core thickness d is decreased, the farther the evanescent field will penetrate into the upper and lower cladding. So typically for a core thickness of 50 nm to 500 nm with a core of index 1.8, lower cladding index of 1.45 and an upper cladding index of 1.0, the penetration into the cladding would be approximately 200 nm for the thinner core to 75 nm for the thicker core. Therefore, the evanescent field penetration

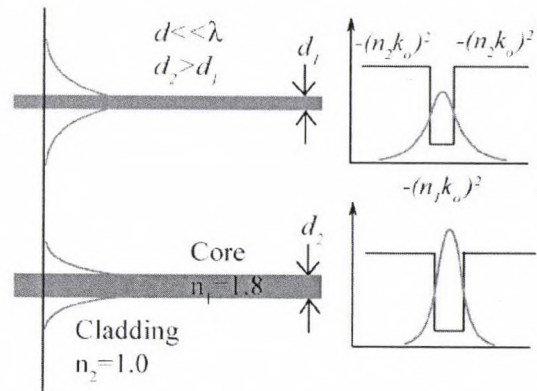


Figure 2.1: Increasing the core thickness reduces evanescent field penetration into the cladding regions, k_0 is the initial magnitude of the propagation vector.

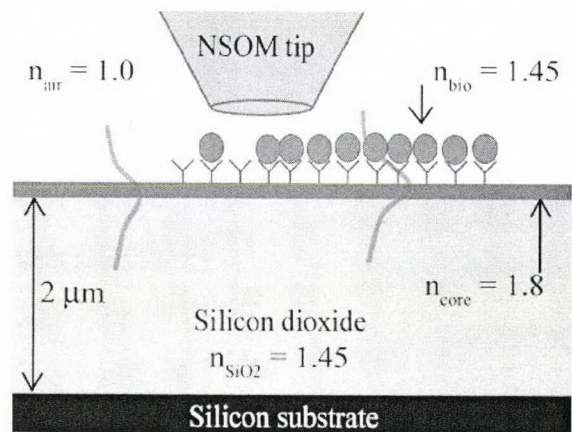


Figure 2.2: Evanescent field response to binding events as measured by NSOM. The field intensity shifts spatially up out of the lower cladding as a response to analyte binding.

depth is sensitive to several properties including cladding and core indices, the thickness of the core and the wavelength of light used.

The penetration of the evanescent field can be used to probe the binding events that occur for a capture region on top of the core of the waveguide. In figure 2.2, a capture region can be observed on top of an active waveguide in air. Some analyte has bound to the probes on the surface forming an adlayer next to the

waveguide core. The binding of the analytes (organic molecule with $n = 1.3$ to 1.5) displaces the fluid ($n = 1.0$ or 1.33) next to the core and changes the effective refractive index of the upper cladding. Light in the evanescent field will interact with these bound species causing a local shift in the field as it responds to the changed refractive index profile. The

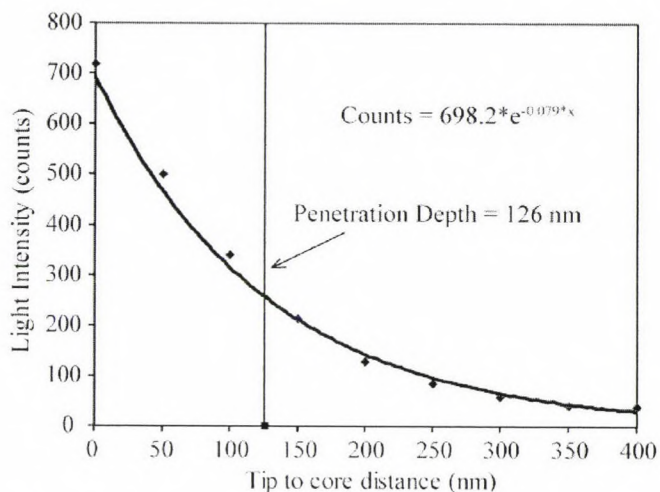


Figure 2.3: Light intensity as measured using NSOM while the tip is lifted away from the surface of a 4 μm wide ridge waveguide. Penetration depth measured experimentally to be 126 nm for this waveguide.

binding of target analytes must take place within the penetration depth of the evanescent field to increase the degree of response. The typical size of an antibody/antigen pair with linking to attach it to a surface is between 10 nm and 30 nm depending on hydration and analyte molecular weight. These binding interactions fall well within the confines of the evanescent wave (see figure 2.3). The attached probes will cause a spatial shift in the field away from the observed intensity for a bare waveguide. There are two ways to determine binding of the target. Before binding and after binding field profiles could be taken, or the profile of a probe region exposed to the sample may be compared with the same probes that aren't incubated with analyte. If there is a difference between the signals from the exposed sample and the unexposed, then the degree of shift indicates the amount of binding of analyte to the probes. With proper calibration of the response

to differing concentrations of analyte in complex milieu with possible non-specific binding interactions, the shift of the evanescent wave can be used as a quantitative and qualitative indicator of analyte concentration.

2.3 Deposition of the Nitride film

The substrates used for waveguide core deposition are silicon wafers with 2 μm of thermal formed SiO_2 . A reactive sputtering technique (Nordiko, see figure 2.4) with argon plasma sputters silicon on the wafer surface, which then reacts with nitrogen radicals from a NH_3 or N_2 plasma. This reactive sputtering forms an amorphous non-stoichiometric layer of silicon nitride (SiN_x). The thickness of the film varies over the surface of the wafer by no more than several nanometers over a 4 in

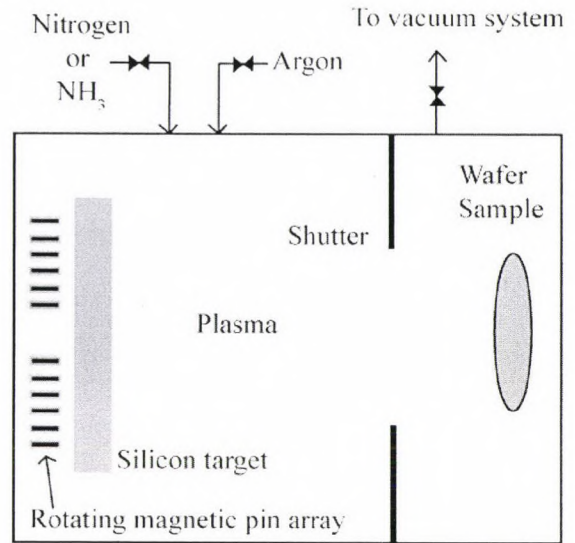


Figure 2.4: Amorphous silicon nitride was deposited using reactive sputter deposition. Argon plasma sputtered silicon onto the sample, which then reacted with nitrogen contained in the plasma

wafer diameter as shown in figure 2.5. Over a typical waveguide length of 15 mm, the thickness of the core varied less than 1%. The base pressure of the plasma during sputter deposition can be adjusted to alter the refractive index of the film. Deposition pressure was set at 12 mTorr to

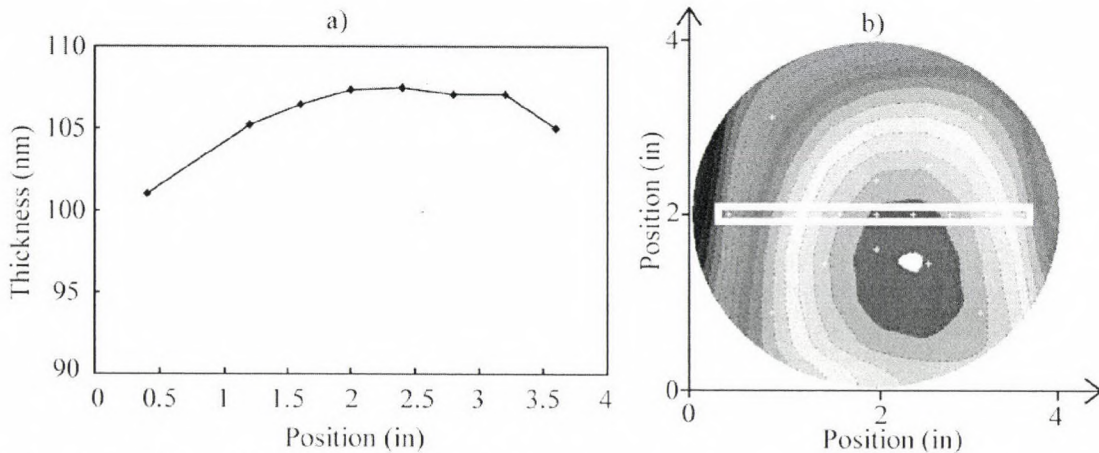


Figure 2.5: a) Centerline thickness profile and b) contour plot for a sputter deposited nitride film on 4-inch wafer

produce a film index of 1.8. Using atomic force microscopy (AFM) the film roughness of the deposited nitride film was found to be ≈ 1.0 nm root mean square (RMS) for a $1 \mu\text{m} \times 1 \mu\text{m}$ region as seen in figure 2.6.

An atomic composition analysis, x-ray photoelectron spectroscopy (XPS), was done on the film at two different sampling depths. For the shallow angle of 15° the x-rays only interrogate the top 1.5 nm of the film surface. Examination of the XPS spectra in figure 2.7 indicates that the surface of the film is mostly a silicon and oxygen mixture with a small amount of nitrogen. The carbon and fluorine were probably present due to surface contamination of the sample from the wafer container. According to this compositional analysis, the surface chemistry for probe attachment would be expected to be the same as any SiO_2 glass substrate. As the XPS angle is increased to 45° the sampling depth is about 4.5 nm, the concentration of silicon stays about the same while the oxygen decreases and the nitrogen increases. So this would indicate more silicon nitride, which is the expected bulk film material.

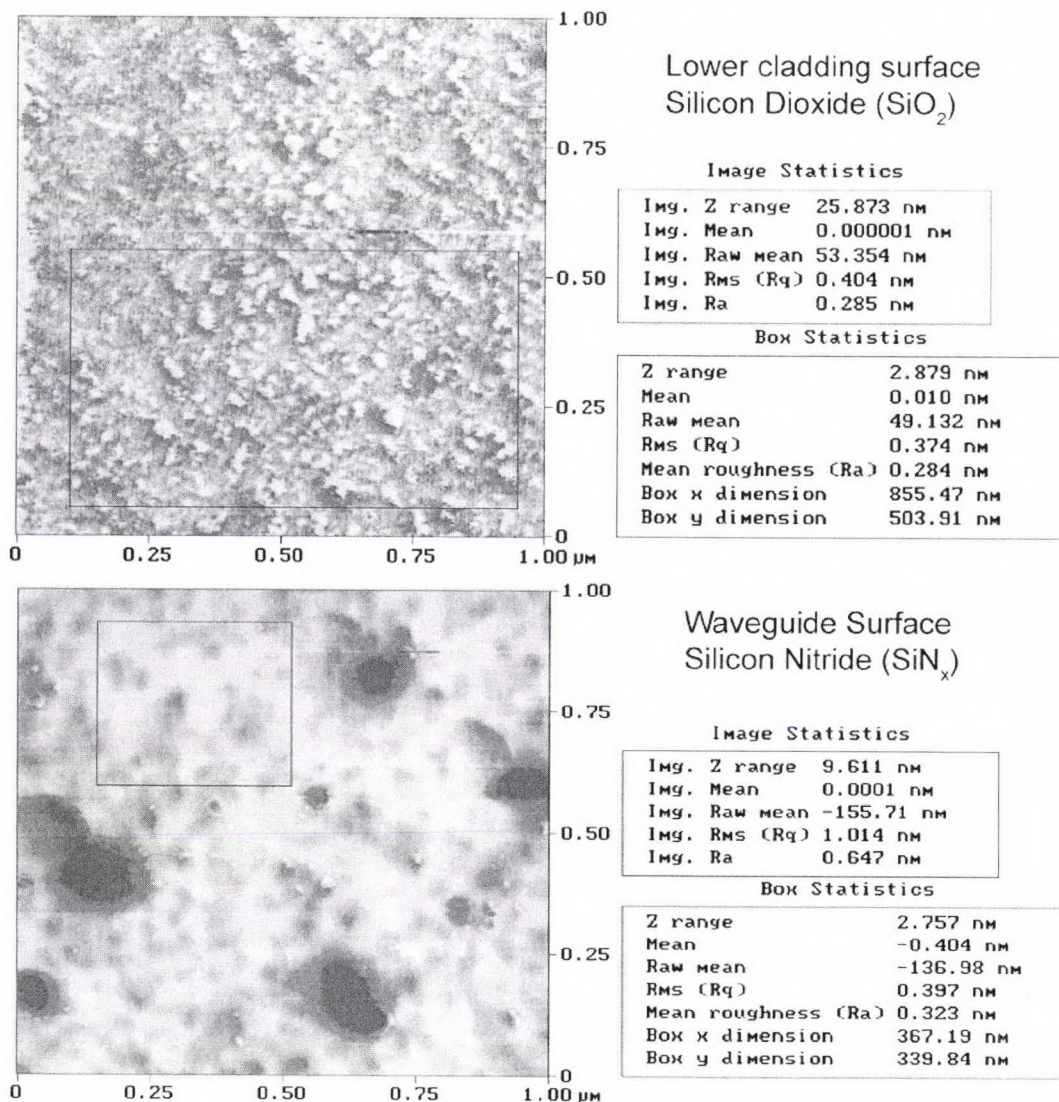


Figure 2.6: AFM roughness scans for thermal oxide and silicon nitride surfaces. SiO₂ roughness was 0.4 nm and SiN_x roughness was 1 nm.

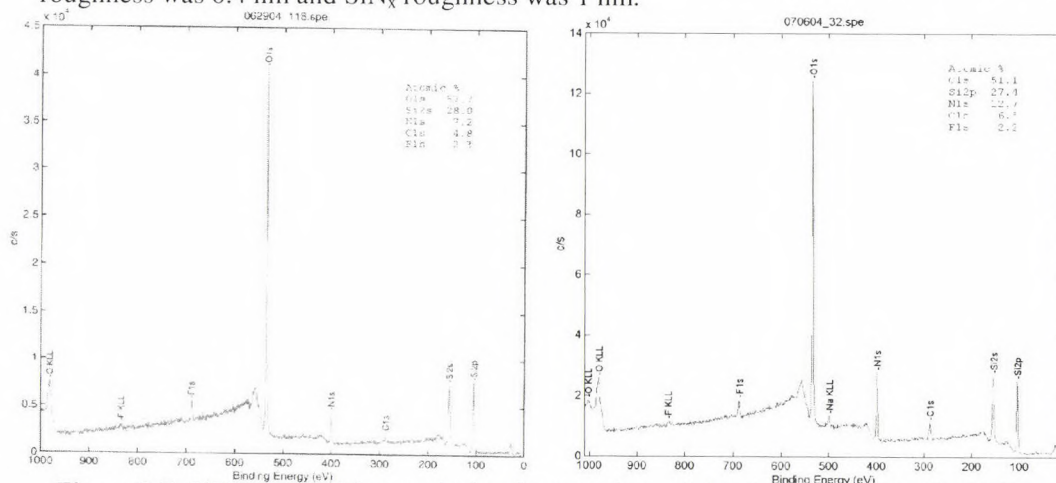


Figure 2.7: XPS composition analysis of top surface of the deposited film. (Left) Top 1.5 nm of the film showing mostly silicon and oxygen as composition. (Right) Top 4.5 nm of the film indicating an increase in nitrogen concentration.

2.4 Prototype waveguide designs

The waveguides fabricated were all of an asymmetric refractive index profile with silicon dioxide at the lower cladding. There were two reasons why an asymmetric design was chosen over a free-floating waveguide with symmetric cladding. Waveguides fabricated with a solid lower cladding were more mechanically durable and allowed moderate pressure from washing or patterning to be applied without risk of damage to the waveguide. The solid substrate waveguides also had a less complex fabrication procedure. Free-floating designs would require additional etching and masking steps in order to remove the solid cladding material under the waveguide.

A 500 nm and 100 nm thick nitride film were deposited so the evanescent field characteristics for a variety geometries could be studied. The whole surface of the film was not used as a waveguide, instead a width of the film

was masked and the remainder etched to form a rib or a ridge that confines and guides the light. If the whole thickness of the film is etched away

leaving a strip of material, the waveguide is termed a rib waveguide. If only part of the film is

etched, the waveguide is called a ridge

waveguide. Using lithography and CF_4/O_2

etching, the width and thickness of the

waveguides were controlled. CF_4 plasma was a very effective etchant for silicon nitride with a

100 nm film being completely etched in less than one minute. The addition of oxygen into the plasma removed any organic photoresist residue from the surface and also removed any possible polymerization byproducts of the CF_4 from building up on the masking photoresist.

Four geometries of waveguides were fabricated in order to study the surface mode characteristics (see figure 2.8). The wafers were masked using the mask design shown in figure

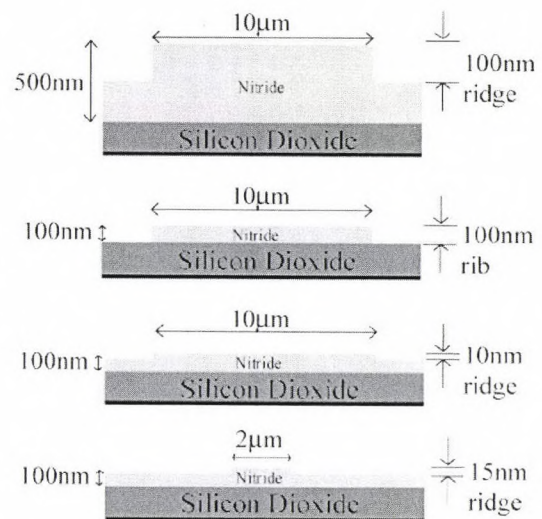


Figure 2.8: Cross section of four test waveguide geometries showing width and etch depth.

2.9. Using the 500 nm thick film, a 250 nm ridge waveguide was etched into the film using CF_4/O_2 plasma in a MicroRIE plasma etcher. Three waveguide types were fabricated out of the 100 nm film samples. A

completely etched 100 nm rib, a 10 μm wide ridge waveguide with a partial etch of 10 nm, and a 2 μm wide ridge with a 18 nm partial etch were fabricated. To launch light into these structures, a technique called end-fire coupling was used. After etching to form the waveguide, the back of the wafer was scribed with a diamond tip pen and the

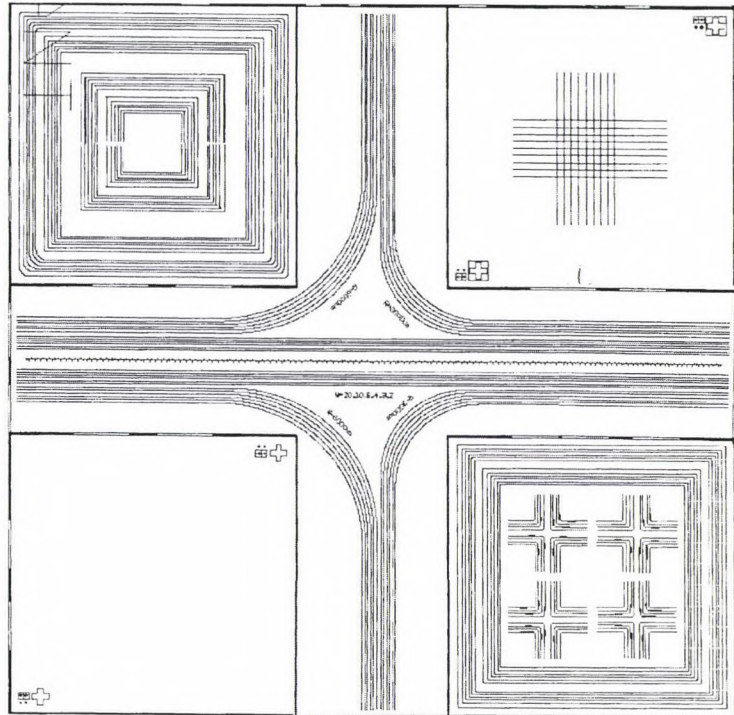


Figure 2.9: Four inch \times four inch chrome-on-glass mask for fabrication of 2 to 30 μm wide waveguides.

sample broken to expose an edge perpendicular to the waveguide. The sample was then attached with Crystalbond 509 (thermoplastic polymer that softens at 160 $^{\circ}\text{F}$ and flows at 275 $^{\circ}\text{F}$) to a dummy sample so the waveguide was protected between the two wafers (Aremco). This wafer stack can then be placed in a holder for edge polishing with successive applications of 20 μm down to 0.05 μm polishing papers. Light is then launched from a single mode optical fiber by aligning the center of the fiber with the polished edge of the waveguide. After bonding the fiber and the waveguide chip to glass plates the alignment is stabilized by bonding the edges of the glass plates together. The fiber is connected to a 10 mW, 654 nm laser diode using a ST fiber connection. To maximize the coupling efficiency between the fiber and the waveguide, a single

mode optical fiber with a core dimension of $4\ \mu\text{m}$ was chosen. This fiber type has the smallest core size of available fiber types and the single mode provides for the best mode matching to excite a single mode in the planar waveguide. The alignment of the $4\ \mu\text{m}$ core of the optical fiber with the $100\ \text{nm}$ by $10\ \mu\text{m}$ core of the planar waveguide resulted in significant coupling losses and was the most time consuming aspect of waveguide fabrication.

2.5 Near field scanning optical microscopy (NSOM)

After end fire coupling, the sample was ready for surface evanescent field intensity measurement. The NSOM has a basic geometry as shown in figures 1.9 and 2.10. The tip has a hollow aperture through the center that was scanned across the surface of the waveguide (figure 2.11). The aperture was $100\ \text{nm}$ in diameter and light was collected through the aperture and sent through a photomultiplier tube and

then sent to a detector. The scan regions are $100\ \mu\text{m}$ by $100\ \mu\text{m}$ on the sample surface. Typical scan sizes collect 256 data points per line scan and an image was composed of 256 line scans producing a 256×256 data array. Therefore for the largest physical scan area, each data point along a line scan was collecting the light over $0.39\ \mu\text{m}$ of the sample and

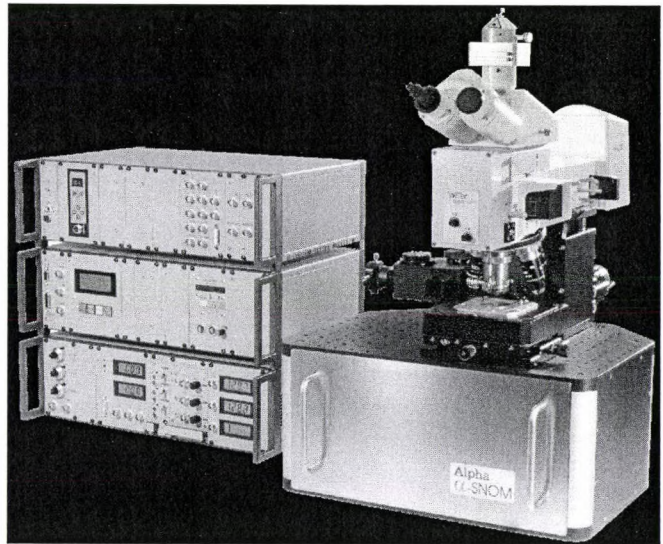


Figure 2.10: α -SNOM instrument [WiTec] (Ulm, Germany)

displaying it as a single point or pixel of the image. The scan speed of the tip is $1.1\ \text{s}$ per forward scan. Slowing the scan speed or scanning a smaller physical region will increase the magnitude of the signal received and averaged for each data point in the array. This will also reduce the average tip speed over the surface and affect the noise in the topography measurement. A laser reflecting

off the top of the tip allows the topography to be measured while simultaneously measuring the light intensity through the aperture in the tip. This dual measurement capability was valuable in helping to determine the location of the waveguide or any probe regions on the sample.

There are several negative features associated with using this method to measure the surface evanescent field. The tip sliding in contact with the surface can disturb soft topographical features such as attached biological molecules. Topography variation can cause issues with how the evanescent field intensity is measured. The optimal case would be to measure the evanescent field intensity at the core/cladding interface regardless of any features attached to

the surface. Unfortunately, the tip was unable to operate using this mode of light collection. When the tip was on a bare portion of the waveguide, away from any attached probes, the tip was in contact with the top surface of the core.

However if the tip scans over a region of attached probes or probes with bound analyte, the tip moves away from the upper surface of the core. This resulted in a lower amount of detected power due to the evanescent field exponential decay as the tip-to-core distance was increased. This decrease in detected power, as the tip moves away from the core, was something that must be considered when looking at the evanescent field response to features that have a lower refractive index than the core.

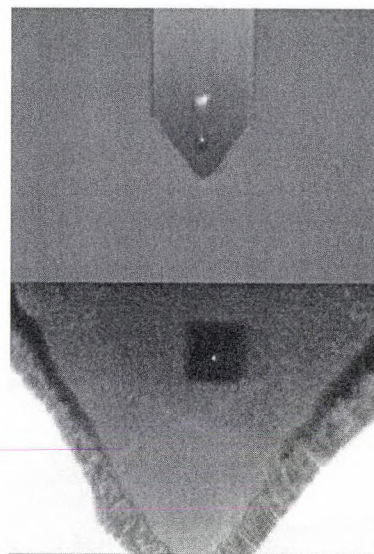


Figure 2.11: Images of the top of the NSOM cantilever tip showing the reflection of the deflection laser and the 100 nm aperture where light is collected.

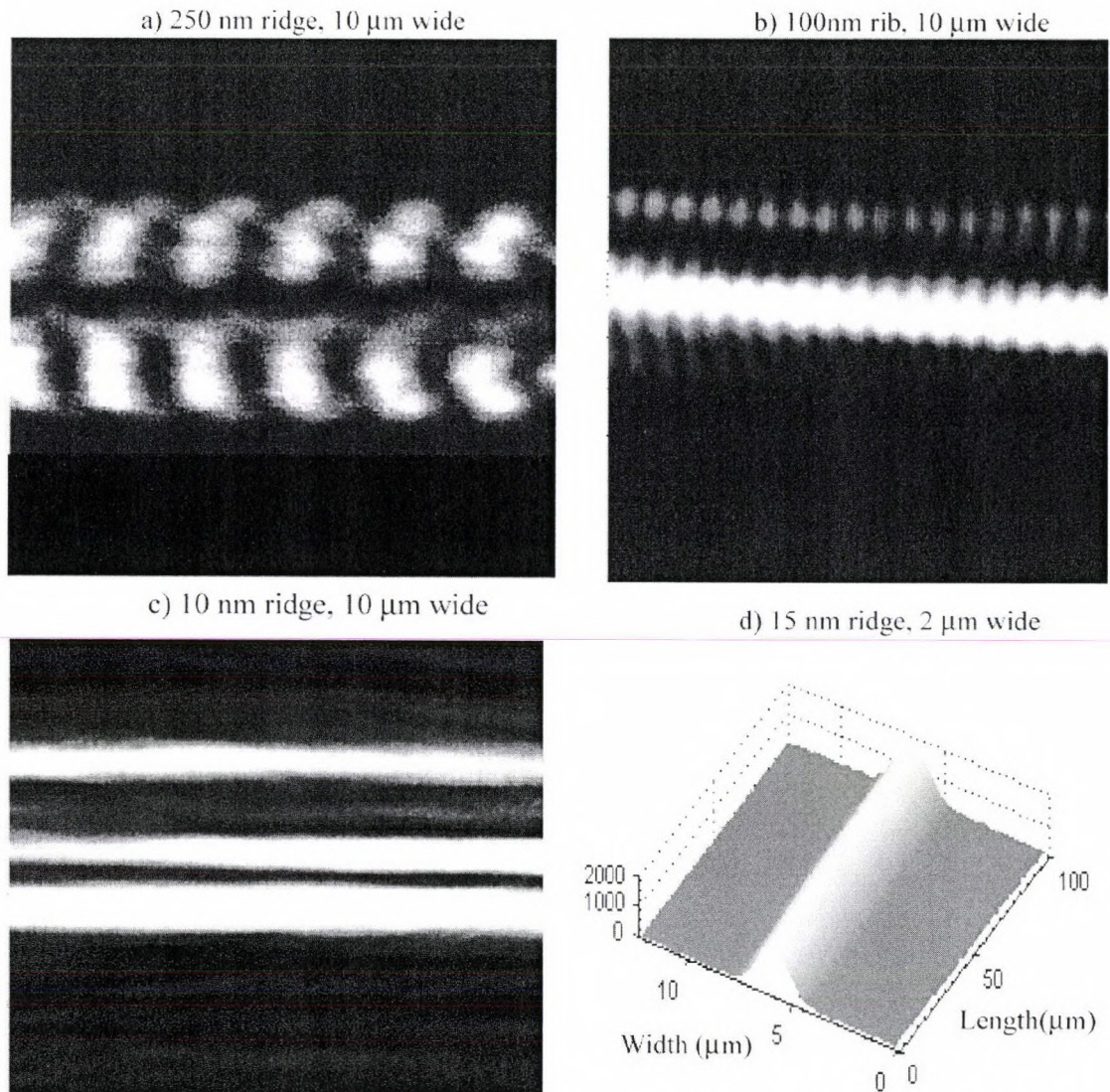


Figure 2.12: Surface mode profiles for preliminary waveguide geometries shown in figure 2.8. The 15 nm ridge waveguide with a 2 μm width with the evanescent field profile shown in the lower right was determined to be single mode and a suitable geometry for sensor fabrication.

2.6 Waveguide geometry and modes

Figure 2.12a shows the surface evanescent field intensity for the 250 nm ridge waveguide. The relatively large core size and width resulted in multiple propagating modes. The mode beating in this structure resulted in areas of the waveguide having nodes, or regions of zero detected field. This was not an optimal design because these nodes result in areas where there is minimal evanescent field penetration into the upper cladding. For the three samples fabricated

from the 100 nm film multimode behavior was also observed in some structures. Figure 2.12b shows the surface field profile for the 10 μm wide 100 nm rib waveguide. Calculations done by G. Yuan indicated this structure has about 30 propagating modes. For the 10 μm wide, 10 nm ridge structure seen in Figure 2.12c, only 3 lateral modes were observed in the NSOM scans with no mode beating observed down the length of the waveguide. For a ridge waveguide with a 2 μm width and an etch depth of 20 nm, only one lateral mode was supported and the profile appears to be single mode (Figure 2.12d). As seen in Figure 2.12d, the 2 μm ridge waveguide geometry has the least number of propagating modes and is the best candidate for the sensor waveguide.

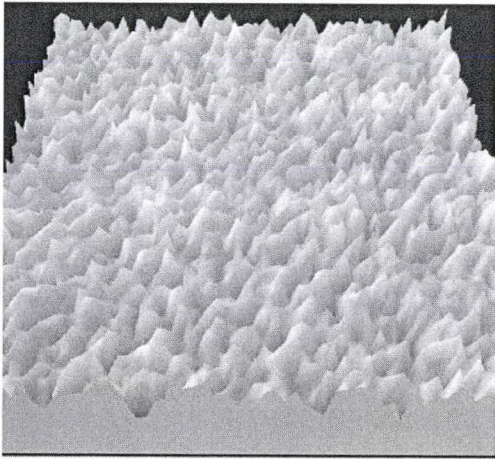
The increase in thickness of the core increases the number of vertical modes and increasing the width allows multiple horizontal modes to propagate. Increasing the number of propagating modes makes determination of the evanescent field response difficult and complicates the data analysis. Mode beating between the guided modes induces oscillation that may interfere with the response caused by the presence of probe/analyte binding. In addition to the beating of the guided modes, for a multimode waveguide, the evanescent field does not extend as far into the cladding regions and changes in cladding refractive index (such as during sample binding) will result in a smaller shift in the field.

2.7 Fabrication summary

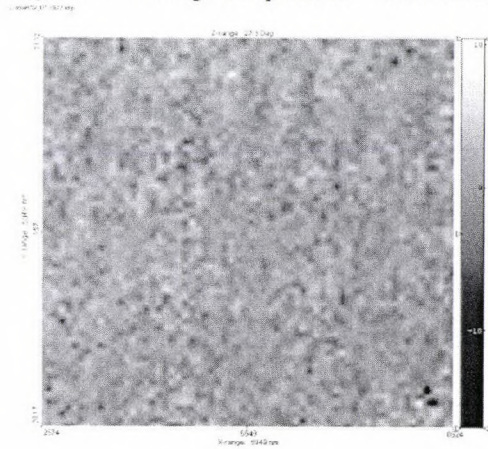
The sensor is based on an asymmetric planar optical waveguide. To fabricate this device an approximately 100 nm thick silicon nitride film is deposited by reactive ion sputtering on a thermally oxidized silicon wafer. The film was deposited using a Nordiko 7000 with a silicon target and NH_3 as the nitrogen source. This sputtering method for film deposition results in an average RMS surface roughness of approximately 2 nm and etching of the silicon nitride increases the surface roughness to a RMS value of 2.53 nm (Figure 2.13). The roughness does have an appreciable impact on the scattering losses from the waveguide and the observed noise in measuring the surface evanescent field intensity. The substrates used to deposit the silicon nitride

are thermally oxidized silicon wafers with 2 μm of oxide (Noel Technologies, Campbell, Ca). Individual waveguide chips are fabricated from the dielectric coated wafer using conventional photolithography and dry etching techniques (see figure 2.14). Approximately 1 in \times 1 in chips were scribed from the wafer and prepared for processing by rinsing in acetone, methanol, and deionized water. After a 120°C dehydration bake, Microposit S1818 positive photoresist was spun on a chip at 5000 to 6000 rpm to obtain a 1.8 μm thick layer. Following a 90°C prebake, the photoresist was exposed using a Karl Suss contact aligner, and the sample was developed and inspected. Ridge waveguides were etched in a Technics MicroRIE plasma etcher in a two step process. An initial etch using O_2 at 50W was used to descum the sample then the 15 nm waveguide ridges were etched at 50 W using a 4:1 $\text{CF}_4:\text{O}_2$ mixture. After stripping the photoresist, clean edges were backside scribed and cleaved perpendicular to the waveguides. Facets on this cleaved edge were polished using a progression of 9 decreasing alumina grit sizes (figure 2.15) from 30 down to 0.05 μm to allow for end-fire fiber coupling to one of the 2 to 3 μm wide waveguides. Shown in figure 2.16 are images of the surface scattering produced by end fire coupling the fiber to the waveguide and the top and side views of the device. Figure 2.17 shows electron micrographs of the surface and edge of some rib waveguides that are ready to be bonded to another wafer for the polishing procedure.

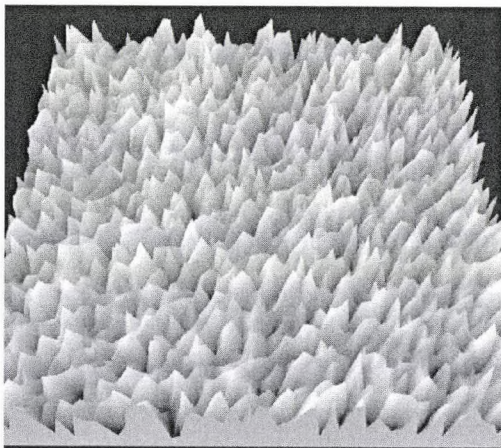
Nitride etched once with CF_4/O_2 plasma



RMS roughness = 2.52 nm
Roughness average amplitude = 2.00 nm



Nitride etched twice with CF_4/O_2 plasma



RMS roughness = 4.28 nm
Roughness average amplitude = 3.46 nm

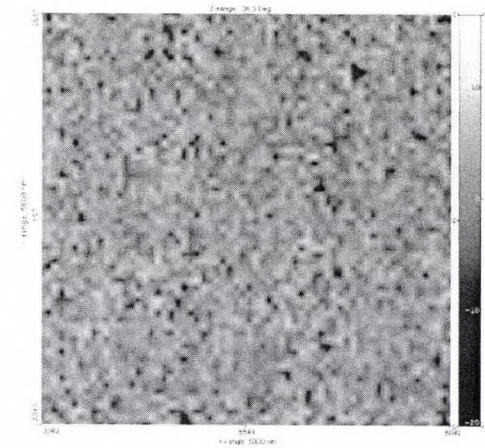


Figure 2.13: Plasma etching the nitride surface increases the RMS surface roughness from 2.52 nm after one etch to 4.28 nm after 2 etching steps. Roughness measured using AFM.

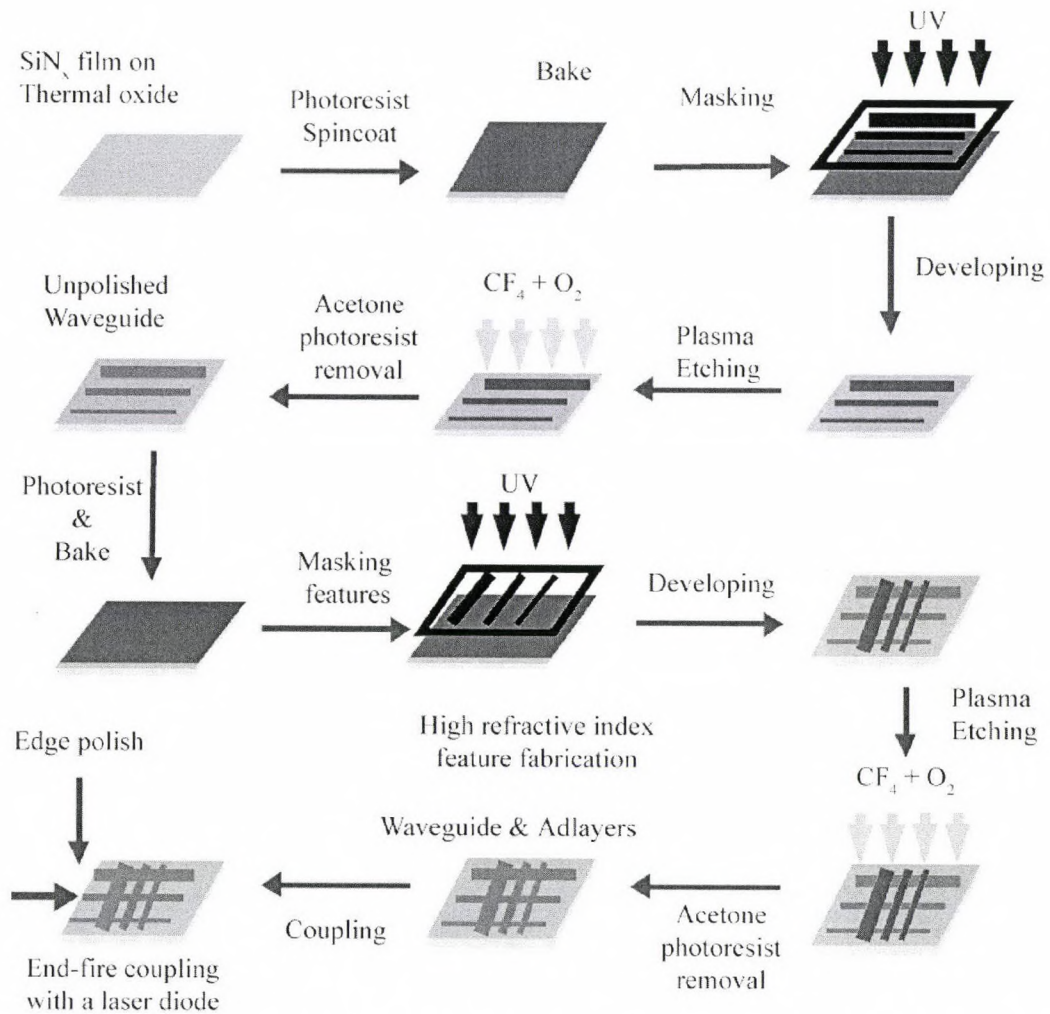


Figure 2.14: Fabrication flow diagram for waveguide and surface features. Fabrication of the waveguide begins with deposition of a silicon nitride film on a silicon wafer with $2 \mu\text{m}$ of thermally formed silicon dioxide. Lithography is then carried out on the sample to mask narrow lines on the sample that will form the waveguides after a dry plasma etching step using CF_4 and O_2 .

In the fabrication of the high refractive index features, an additional lithography and etching step is needed to form those features. For deposition of proteins or patterning of photoresist features, the waveguide is polished and then those features are patterned on the waveguide surface. After polishing and patterning features, light is launched into the waveguide by using a laser diode coupled to a single mode optical fiber. The end of the fiber is aligned with the polished facet of the planar waveguide and the coupling stabilized to allow the sample to be moved as shown in Figure 2.16.

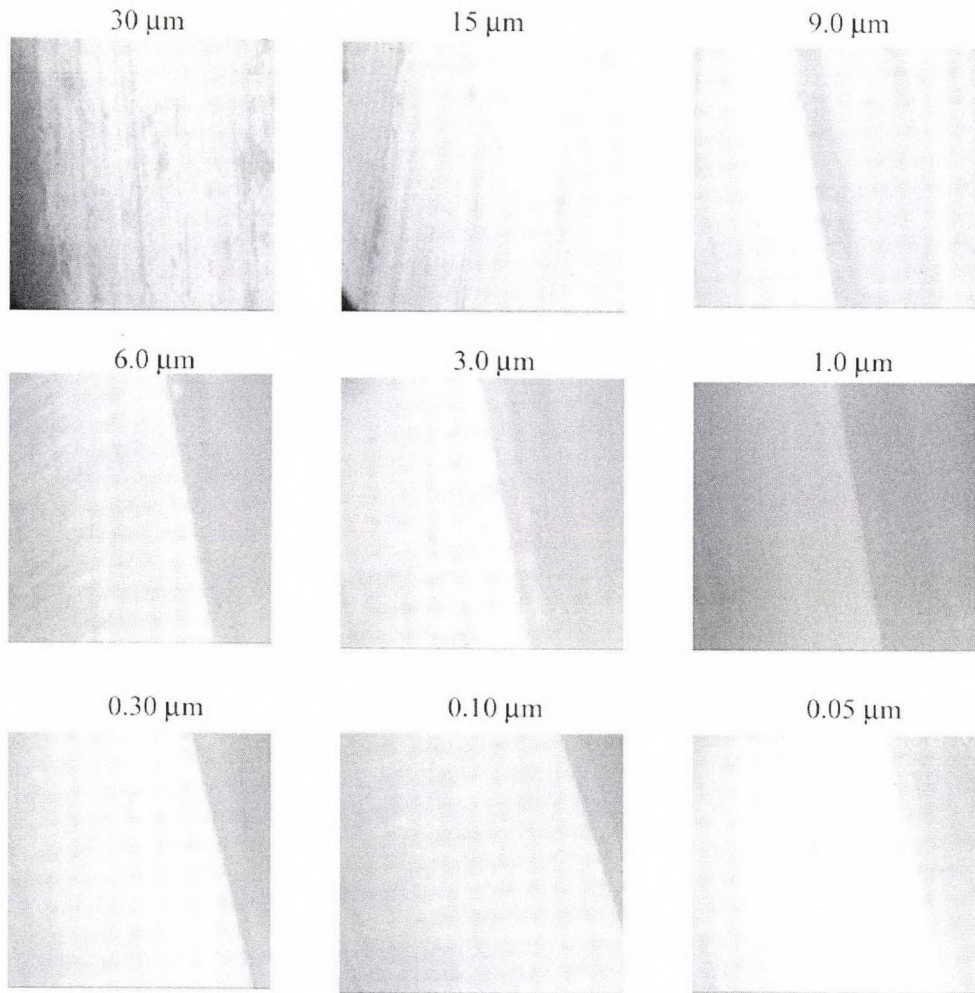


Figure 2.15: Facet polishing using a progressive series of diamond wet polishing paper.

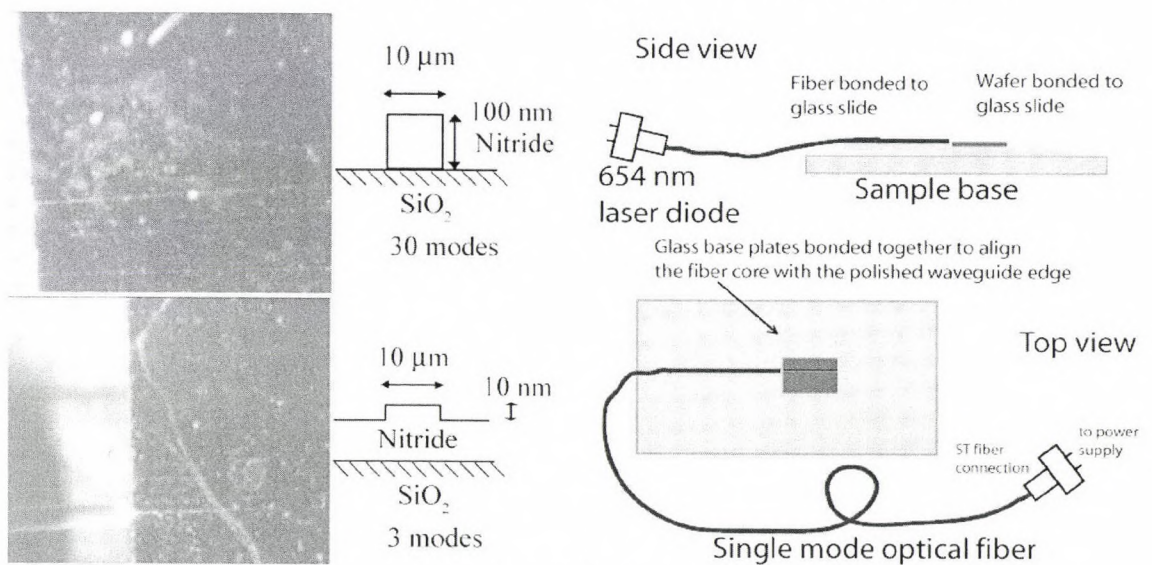


Figure 2.16: End-fire coupling and view of completed waveguide with bonded fiber

2.8 Conclusion

The process for the creation of a planer optical waveguide from a film of amorphous silicon nitride on thermal oxide has been developed and implemented. Wet polishing of the wafer edge was accomplished and end-fire coupling was used to couple 654 nm light into the waveguide core. The surface evanescent field intensity in air was measured for several geometries using NSOM to determine mode profiles. The geometry of the waveguide and the number of propagating modes have an effect on the surface light intensity. It was found that a less than 3 μm wide ridge waveguide formed from partial etching a film with a thickness of 100 nm would result in a single mode waveguide.

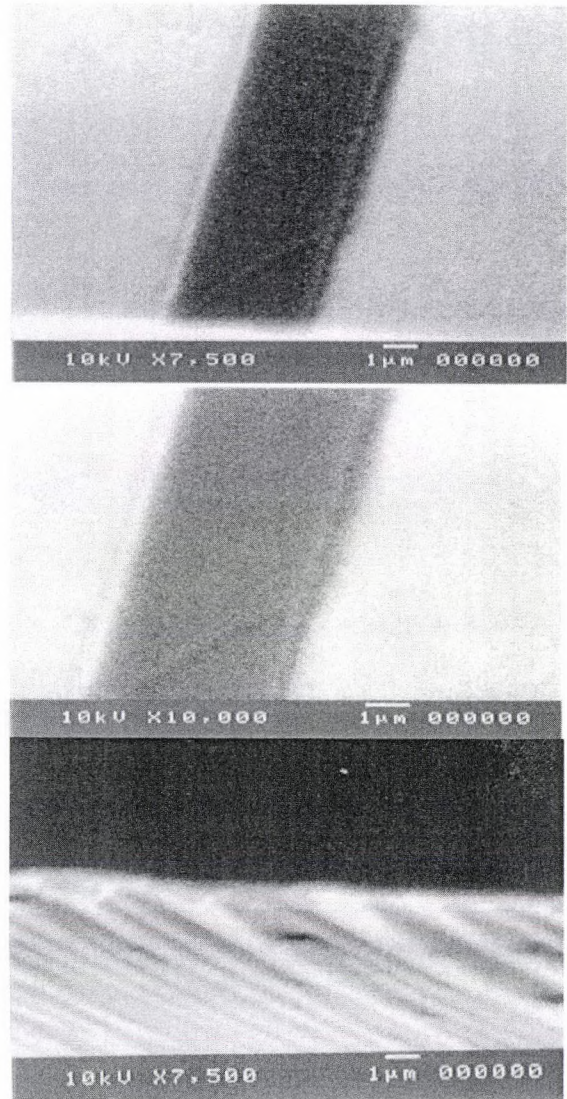


Figure 2.17: Electron micrographs of unpolished waveguide edge

Chapter 3 – Features on the waveguide¹

3.1 Fabrication of high index features on the waveguide surface

The first step in determining the evanescent field response to features on the waveguide was to fabricate some features that had a similar height and longitudinal extent to biological

probe regions. The most easily fabricated features are of the same refractive index as the core of the waveguide. This type required only an additional lithography and etching step to fabricate. The feature thickness was easily adjusted through control of the etching times. The waveguide fabrication details can be found in Chapter 2 and the fabrication flow diagram for the high refractive index features is shown in figure 2.14. Nitride features 7 μm

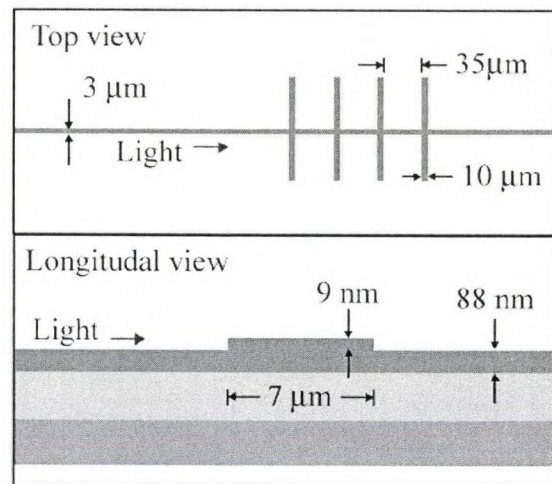


Figure 3.1: Geometry of high refractive index features fabricated on the waveguide surface to determine the evanescent field response to surface refractive index changes.

long and 9 nm thick were fabricated (see figure 3.1) on a waveguide and the field response was measured using NSOM.

3.2 S/N and power modulation for NSOM results

To analyze the response of the evanescent field to the features fabricated on the core, it is useful to calculate the change in detected power. For the following experiments in this chapter

¹ Text from this chapter first appeared in a manuscript: Stephens, Matthew D., Guangwei Yuan, Kevin L. Lear, David S. Dandy, "Optical and physical characterization of a local evanescent array coupled biosensor: Use of evanescent field perturbations for multianalyte sensing," Submitted Aug 18, 2009 to Sensors and Actuators B: Chemical.

and chapter 4, the ΔP value, the power modulation, is defined as the absolute value of the average signal over the pattern less the average power before the pattern divided by the power before the pattern (see Equation 3.1).

$$\Delta P = \left| \frac{(Light_in_pattern) - (Light_before_pattern)}{(Light_before_pattern)} \right| \times 100\% \quad \text{Equation 3.1}$$

This power modulation measurement provides a normalized standard that is useful for comparing the response to features with differing heights, lengths and refractive indices. The magnitude of the power modulation must also be compared with the amount of noise present in the signal generated through NSOM scans of the surface evanescent field intensity. The *RMS* (root mean square) noise for a signal is defined as the square root of the absolute value of the sum of variances from the signal (see Equation 3.2). The variance is the expected square deviation of the signal from the average signal. In other words, the *RMS* noise is roughly equivalent to the average difference between a data point and the average signal.

$$RMS = \sqrt{\left| \frac{\sum_{i=1}^n \left(X_i - \frac{\sum_{i=1}^n X_i}{n} \right)^2}{n} \right|} \quad \text{Equation 3.2}$$

where X_i is an individual data point and there are n data points in the signal. The S/N (signal to noise ratio) for a specific response of the evanescent field to a feature is defined as the average difference between the input signal and the signal over the feature divided by the RMS noise on the input signal (see Equation 3.3).

$$\frac{S}{N} = \frac{Signal}{RMS_noise} = \frac{(Light_in_pattern) - (Light_before_pattern)}{RMS_noise} \quad \text{Equation 3.3}$$

The code used to calculate these quantities from the NSOM array data is shown in Appendix B.

According to the International Union of Pure and Applied Chemistry's Goldbook, the limit of detection of an analytical method is defined as the concentration or quantity that can be detected with reasonable certainty according to the following equation:

$$X_L = \bar{X}_b + ks_b \quad \text{Equation 3.4}$$

where X_L is the signal that corresponds with the limit of detection, \bar{X}_b is the mean of blank measurements, k is a numerical factor chosen according to the confidence level, and s_b is the standard deviation of blank measurements. For the each of the features studied in chapter 3 and 4, the feature height corresponding to the limit of detection at a confidence level of 95% will be indicated.

3.3 NSOM results for high refractive index features

Uniform evanescent field intensity was measured before the feature. At the feature the surface field was observed to increase over the feature (see Figure 3.2). Figure 3.2 is composed of

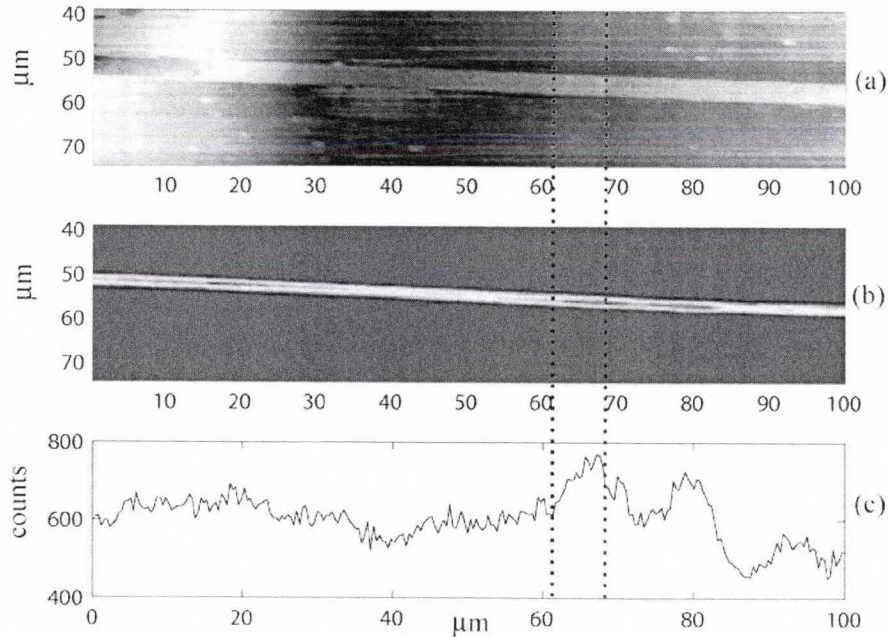


Figure 3.2: First feature in a series of four. Light travels from left \rightarrow right. (a) Topography of 4 μm wide waveguide with 34 nm etch depth. Feature size is $\approx 7 \mu\text{m}$ in length and 5 nm thick, (b) Surface light intensity measured with NSOM, (c) Total light measured in photon counts carried in the waveguide after subtracting the background. An increase in surface evanescent field intensity is observed over the feature followed by oscillations.

three images. The top image (a) is a false color (grayscale) image of the topography of the

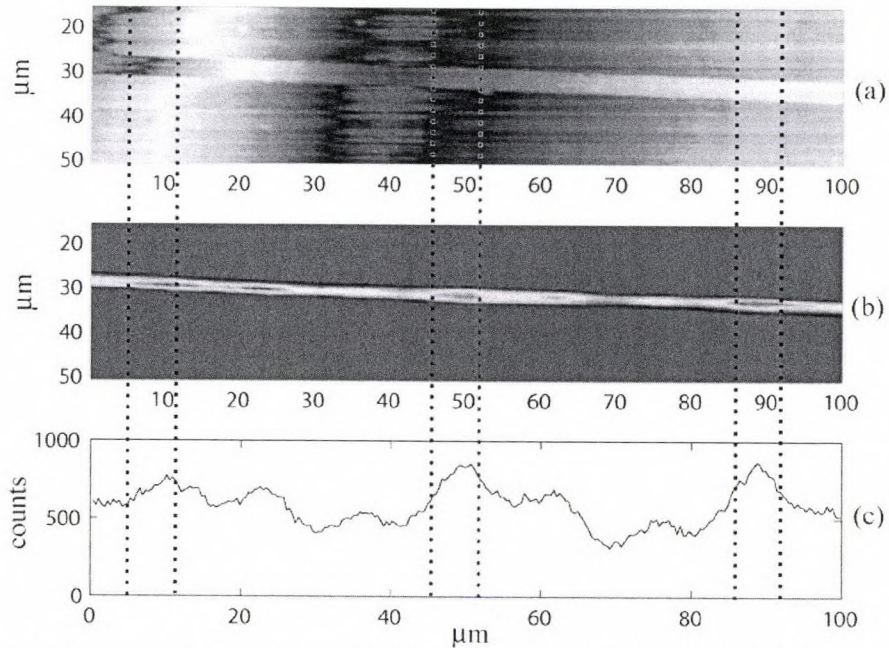


Figure 3.3: Response to first, second and third closely spaced high refractive index features in series. Light travels from left \rightarrow right. (a) Topography of 4 μm wide waveguide with 34 nm etch depth. Each feature size is $\approx 7 \mu\text{m}$ in length and 5 nm thick, (b) Surface light intensity measured with NSOM, (c) Total light measured in photon counts carried in the waveguide after subtracting the background. An increase in light was observed over each feature. Oscillation period is approximately 14 μm between the features.

waveguide and any surface features found within the scan region. The middle image (b) is a false color (grayscale) image of the 2D light intensity measured at the surface of the sample using the NSOM tip. The bottom image (c) is the total light intensity in photon counts averaged across the width of the waveguide after background subtraction. Almost all of the light field responses to patterned features will be presented in this format in this chapter and the next.

The light before the region was bound to the first order mode and its intensity profile determined to be a single Gaussian distribution centered on the waveguide. As the light encountered the feature, the light distribution spatially shifted up due to the refractive index change at the surface and part of the light was promoted to a higher order mode. As the light exits the area, the distribution of light drops so that more was carried in the lower cladding and the

higher order mode was no longer supported by the geometry of the waveguide. The fraction of waveguide power carried in the higher order mode was either coupled back into the fundamental mode or lost into the cladding regions. As seen in Figure 3.2, as the light exits the feature, the intensity drops and the field oscillations decay back to a uniform intensity level (see Figure 3.5). The oscillations are a result of the guiding conditions changing as the light traveled through the feature region.

The decaying mode beating that was observed was due to the weakly bound higher order mode interfering with the guided mode. The mode beating influenced the spacing of patterns along the waveguide. A stable field before a pattern was needed to ensure the measured effects could be separated from adjacent patterns. This experiment placing the patterns 35 μm apart for 9 nm thick features determined that 35 μm was insufficient spacing (see figures 3.3c and 3.4c). The oscillations observed in the evanescent field between features had not decayed out of the waveguide before the light encountered the next feature.

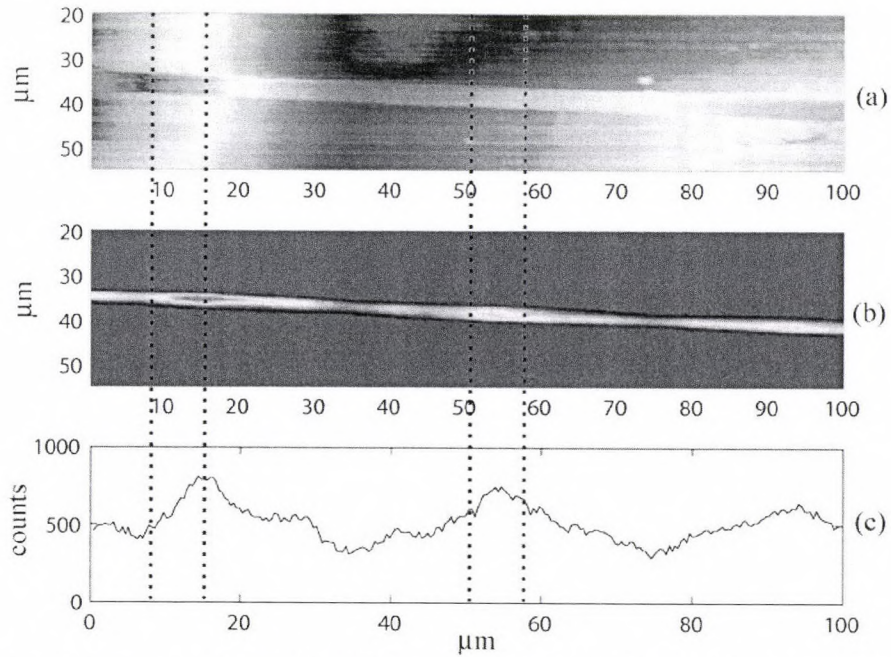


Figure 3.4: Response to third and fourth high refractive index features in series. Light travels from left \rightarrow right. (a) Topography of 4 μm wide waveguide with 34 nm etch depth. Each feature size is $\approx 7 \mu\text{m}$ in length and 5 nm thick, (b) Surface light intensity measured with NSOM, (c) Total light measured in photon counts carried in the waveguide after subtracting the background. The oscillation period outside the feature region was larger than inside the feature region.

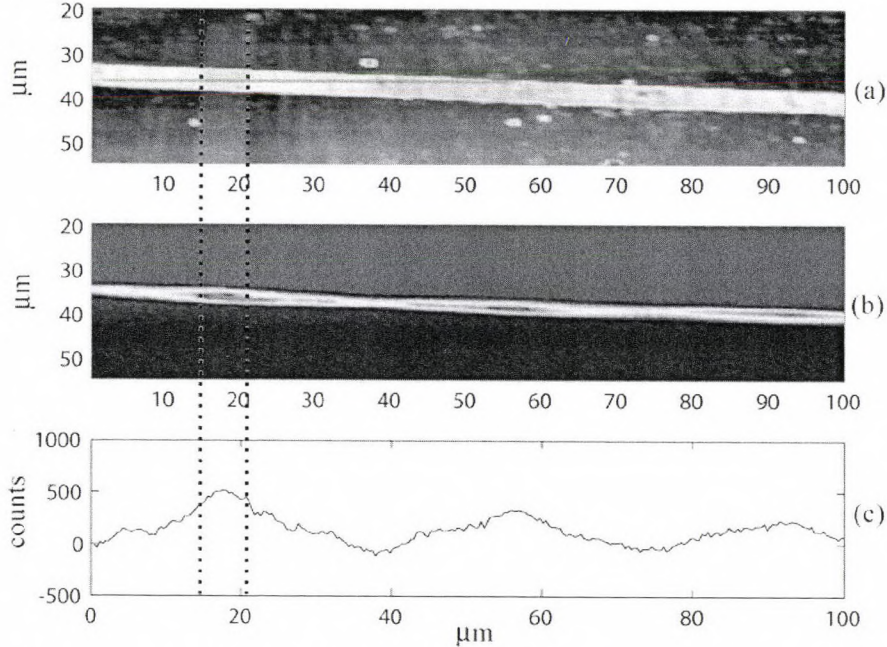


Figure 3.5: Response to fourth high refractive index feature in series. Light travels from left \rightarrow right. (a) Topography of 4 μm wide waveguide with 34 nm etch depth. Each feature size is $\approx 7 \mu\text{m}$ in length and 5 nm thick, (b) Surface light intensity measured with NSOM, (c) Total light measured in photon counts carried in the waveguide after subtracting the background. Oscillations were observed to decay after the last feature. Oscillation period $\approx 40 \mu\text{m}$ after the last feature.

To determine the effects of feature length and thickness on the evanescent response, a second sample was fabricated with a feature length of $13\ \mu\text{m}$ and a thickness of $30\ \text{nm}$ (figure 3.6). The response increased when length and thickness of the feature was increased (see table 3.1). Also the features were placed $190\ \mu\text{m}$ apart and the field was observed to return to a uniform value between features.

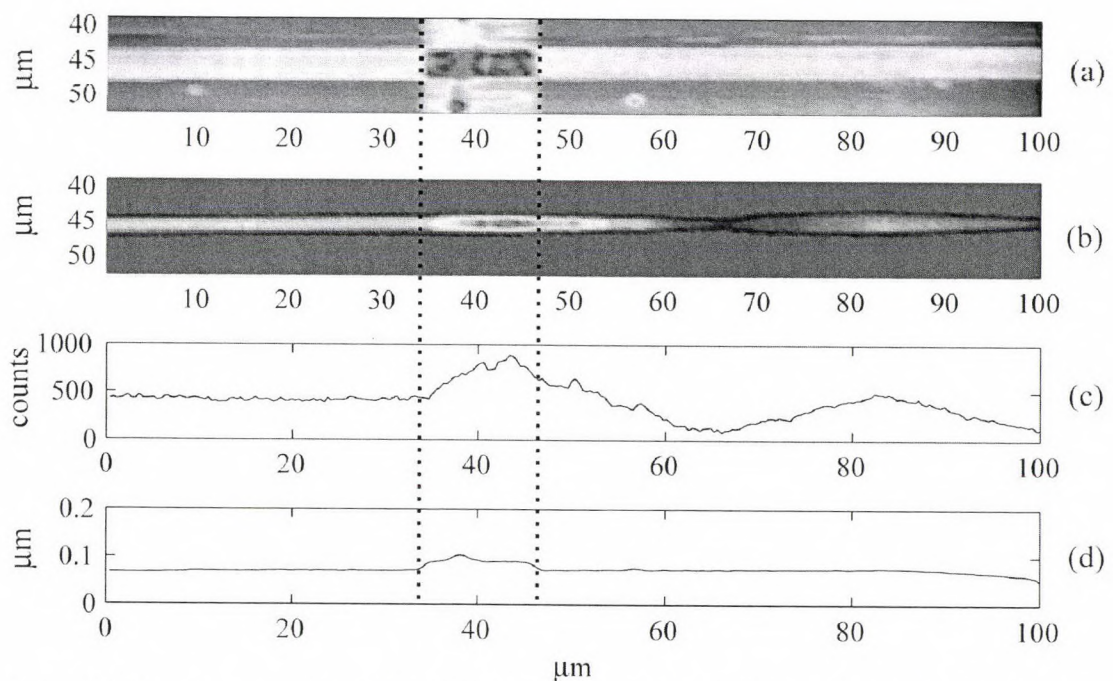


Figure 3.6: Response to a larger high refractive index feature. Light travels from left \rightarrow right. (a) Topography of $4.5\ \mu\text{m}$ wide waveguide with $21\ \text{nm}$ etch depth. Feature size is $\approx 13\ \mu\text{m}$ in length and $30\ \text{nm}$ thick, (b) Surface light intensity measured with NSOM, (c) Total light measured in photon counts carried in the waveguide after subtracting the background showing a larger increase in light over the feature than was observed for thinner features. (d) Cross-section of the topography scan showing the location of high refractive index feature. Oscillation period is approximately $34\ \mu\text{m}$ after the feature.

3.4 Numerical simulation of field response to high refractive index feature

The beam propagation method (BPM) is a mathematical modeling approach that can describe the 2D and 3D propagation of optical energy in a waveguide. The surface light intensity profile for this planar waveguide structure can be modeled using BeamPROP (RSoft), which is based on the beam propagation method. To confirm the NSOM results of the response to high refractive index features, the waveguide with a high refractive index feature was simulated using BeamPROP by G. Yuan. Figure 3.6 shows the topography

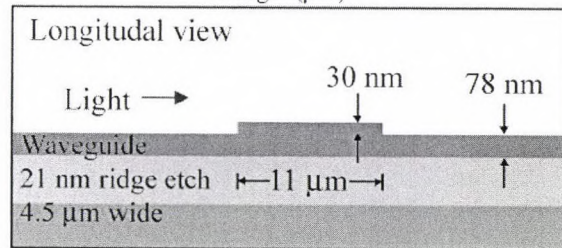
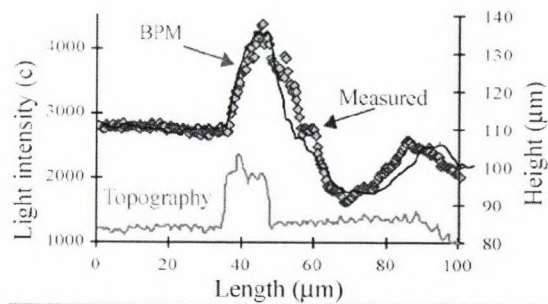


Figure 3.7: BeamPROP and experimental results (top) for a high refractive index feature. Simulated geometry (bottom). Light travels from left \rightarrow right. Surface evanescent field increases as a response to the feature.

and light intensity as measured using NSOM for a feature with a thickness of 30 nm. The geometry and an overlay of the light intensity with the simulated response using BeamPROP is shown in figure 3.7 (simulation done by G. Yuan). As can be seen, the light profile generated by the BeamPROP simulation has the same trends as observed with the NSOM. The simulation accurately predicted the magnitude of the initial change in field intensity. The decaying oscillations were also predicted after the feature. The strong quantitative agreement between laboratory measurements and model predictions gives confidence in the experimental procedure and methodology. These simulation results also validate the assumptions about how the waveguide operates.

3.5 Summary of experimental results for high refractive index features

Several conclusions may be drawn from the analysis of these results of the data shown in figures 3.2 to 3.7. The evanescent field responded in a significant manner to 9 nm and 30 nm

thick features attached to the core. The power modulations for each feature are shown in table

3.1.

Feature	1 – Fig 3.2	2 – Fig 3.3	3 – Fig 3.4	4 – Fig 3.5	Fig 3.6
Δp	16.7 %	50.8 %	47.9 %	70.3 %	66.1 %
Length	7 μm	7 μm	7 μm	7 μm	13 μm
Height	5 nm	5 nm	5 nm	5 nm	30 nm
S/N	10.4	26.1	25.3	21.5	25.2
LOD	0.822 nm	0.83 nm	1.3 nm	1.5 nm	1.32 nm

Table 3.1: Power modulation values and feature sizes for four high refractive index features in series and one larger feature. S/N is the non normalized power modulation divided by the RMS noise level and the limit of detection (LOD) is the thickness of the pattern in nm that corresponds to the signal generated at the limit of detection as defined in equation 3.4.

These are good approximations of the dimensions of common probe/analyte interactions involving the capture and detection of proteins. Results from these high index features indicate that probe/analyte binding events forming a layer of biological material 10 to 20 nm thick may induce a measurable spatial shift in the evanescent field intensity. The second conclusion that was drawn was that for feature lengths as small as 7 μm , the field shifted and responded in a significant manner. The feature length had an impact on the number of capture regions that were placed on the active region of the waveguide and influenced the multianalyte capabilities of the sensor. The smaller the features were made while still producing a measurable and significant response, the more sensing elements that could be placed in the device. The third conclusion that was made was the oscillations produced by each feature might affect the signal received at the other features. For these high refractive index features, the oscillation period was about 35 to 40 μm and it appeared to take three periods for the oscillation to decay. This produced some interesting effects in the fields measured from the features fabricated with 35 μm spacing. As shown in figure 3.3, the oscillations reinforced each other and the power modulation increased for

each subsequent feature. Ideally the normalized response from features with the same refractive index profile and geometry would be the same. The spacing of adjacent features should be designed such that the light field is uniform as it encounters a feature. This would better ensure the response measured at each feature would be the light response to that feature alone. These results indicate that it should be possible to directly detect the binding events associated with proteins interacting with probe regions using the shift in the evanescent field.

3.6 Evanescent field response to photoresist features

The designed operation of this device for the detection of relevant analytes is based on capturing targets out of a sample milieu [29-34] and allowing the capture events to interact with the evanescent field. The sensor elements are patterned in an array attached directly to the high refractive index core of the waveguide. When an aqueous mixture is brought into contact with the sensor surface, complementary analytes diffuse toward the capture regions and bind or hybridize with their respective probes [35-38]. As the capture events take place, the sample milieu immediately adjacent to the core, assuming water with a refractive index of 1.33, is displaced by the captured analytes that have a refractive index from 1.35 to 1.6 [41-43]. Binding occurs at the surface of the waveguide core, and as a result the bound analyte becomes part of the optical cladding of the waveguide. By monitoring the evanescent field it is possible to infer that binding is occurring in locations where there is a shift in the field intensity.

However, there are a number of important issues to be addressed in this system.

- (1) The degree to which the evanescent field change depended on the size of the analytes that bind to the surface.
- (1) The effect of adjacent capture regions on the signal obtained from a region.
- (2) The minimum size for a capture region that provides a detectable change in the evanescent field.

To begin to address these issues, the probe/analyte regions were emulated by patterning the waveguide with an organic film having an index similar to that of biological material. A reproducible means of fabricating these regions is via the use of photolithography techniques. The optical field around these photoresist features was experimentally determined NSOM. The following sections describe the patterning of the photoresist features, the interrogation of the surface evanescent field and the computer simulated response to a representative feature.

Features were fabricated on the waveguide using lithographically patterned organic films with thicknesses of 60 nm and 130 nm. The presence of the organic material on the waveguide caused up to a 70% change in the intensity of the evanescent field over the patterned region and the excitation of a weakly bound higher order mode. The waveguide core and surrounding cladding were numerically simulated using BeamPROP and these predictions were in quantitative agreement with the experimental results obtained using NSOM.

Biological analytes have a refractive index of 1.35 to 1.6 depending on composition and hydration. The core of the waveguide has an index of 1.8 and photoresist has an index of 1.6 as determined using ellipsometry. Determining the response to a patterned organic film is believed to better approximate the detection of analytes of interest than the detection of artificial core thickness changes. Patterning photoresist features on the waveguide provides a refractive index profile closer to that of real analytes and gives more insight into the creation of a sensor capable of measuring relevant analytes. Using patterned photoresist, the evanescent field response to changes in feature length, spacing and thickness was determined.

3.7 Creating the photoresist features on the waveguide

Earlier in this chapter, the effect of core thickness changes on the local evanescent field was explored [39, 40]. To more accurately approximate the refractive index profile of a probe layer with captured analyte, photoresist was used to more closely match the refractive index of biological features. Waveguides were fabricated as described in Chapter 2 and then a thin layer of photoresist (Shipley 1818) with a refractive index of 1.6 was patterned to approximate the

refractive index profile and size of attached probe/analyte (see figure 3.8). To simulate capture of a series of large proteins or virus particles on the waveguide surface, the photoresist thickness was set between 60 and 130 nm. To obtain films of this thickness, the stock S1818 photoresist was thinned by the addition of a low viscosity solvent, Propylene glycol monomethyl ether acetate (PGMEA). The thinned photoresist was dispensed on the sample and spun at 5000 to 6000 rpm to create the film, which was then baked, exposed, and developed using the same procedure as prescribed for the stock S1818.

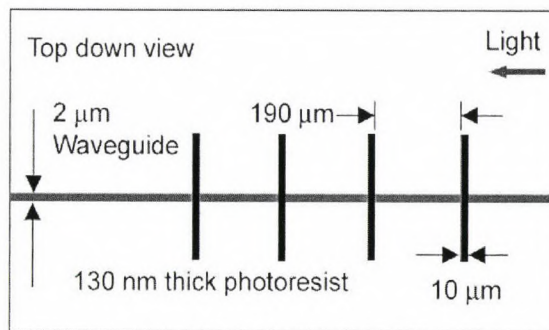


Figure 3.8. Geometry of uniform resist features patterned on the waveguide.

The thickness of the layer of the photoresist was then determined using the topography capabilities of the NSOM. Initially the S1818 was diluted 1:1 by mass with PGMEA, however this resulted in a photoresist coating of approximately 150 nm, which was larger than desired. A solution of 2:1 solvent/photoresist was created and used to coat a wafer at 6000 rpm. This resulted in an approximately 130 nm thick layer of the photoresist. An additional dilution (2.6:1) was produced allowing for the creation of a 60 nm layer of photoresist if spun at 5000 rpm.

3.8 Measuring light response

NSOM was used to interrogate the light field surrounding the waveguide and quantify the impact of the polymer adlayer regions on the evanescent field. In this discussion, the term adlayer is used to represent the presence of a photolithographically patterned feature on the surface of the waveguide core. The instrument used to observe the field, an alpha-SNOM (Witec, Ulm, Germany) was placed on an air table and suspended by tension cables to provide a vibration free platform ensuring that topography was measured with reduced environmental noise. The NSOM acquired simultaneous topography and surface evanescent field intensity by raster scanning a cantilever tip across the surface of the sample (see figure 1.9). The tip operated in contact with

the surface of the waveguide and collected light from the evanescent field through a 100 nm diameter aperture. This collected light was then amplified with a PMT, and a 2D intensity plot of the local evanescent light field was created. The topography of the sample was determined through deflection of the cantilever tip in contact with the surface. The deflection of the tip was determined by the change in signal from a detector that collected light from a laser beam reflecting off the tip of the cantilever. The cantilever tips were held in place by a magnet and were aligned with the fiber optic cable that collected the light through the tip aperture. The optical path alignment was accomplished by observing the tip through the instrument's CCD display. The tip was brought in contact with a waveguide and the stage adjusted such that light traveling down the waveguide was observed through the aperture of the tip. The aperture was usually centered over a strong scattering center of the waveguide. This provided a strong signal and light was easily visible through the aperture. The signal from the detector was then monitored as the position of the fiber optic cable was changed using the x-y positioning knobs. Centering the fiber's location over the aperture maximizes the detected signal, producing the best S/N ratio in the light intensity scans. To quantify the evanescent field intensity, a $100\ \mu\text{m} \times 20\ \mu\text{m}$ area was scanned while collecting topography and light intensity information. The default settings for the image generation were 256 line scans with 256 data points taken per line scan. The normal scanning speed used was 0.8 to 1.2 s per line scan in the forward direction and 0.5 s in the reverse direction. If a smaller area was scanned, the number of line scans, scan speed, and data points per line remained the same.

The procedure for measuring the evanescent field strength was as follows: a dc power supply inputted 20 to 40 mA to a laser diode with an output wavelength of 654 nm. The laser diode was connected to a length of single-mode optical fiber. The fiber provided the light source to end fire couple light into the waveguide film. The waveguide chip and the associated fiber were bonded onto an aluminum block to provide a stable platform allowing movement of the chip without negatively impacting the coupling alignment. The sample was placed on the stage of the

NSOM and the tip brought down into contact with the surface of the waveguide chip. To complete the testing, light/topography scans were taken to determine the evanescent field intensity on the surface of the chip. The data was analyzed using the Image Control (WiTec) image analysis software or exported and plotted with Matlab (The Mathworks).

3.9 Modeling field distribution using the beam propagation method

Using the commercial software package BeamPROP from RSoft, the 2D optical power distribution was simulated for a waveguide structure with one adlayer feature [40, 50]. The core of the waveguide was simulated using a refractive index of 1.822, the lower cladding layer with 1.45 refractive index, upper cladding of air with 1.00 refractive index and the feature with 1.55 refractive index. The simulated feature was 8.5 μm long. The incident beam was assumed to be the TE_{00} mode at a wavelength of 654 nm and the thickness of the photoresist layer was 130 nm. The exit boundary condition was set to be a non-reflective boundary. This best approximates the propagation when the waveguide was long enough so that reflections from the end of the waveguide were negligible. The transverse and longitudinal grid spacing was 10 nm and 100 nm, respectively. The software package solved the 2D Helmholtz equations that described field propagation (simulation done by G. Yuan). The overlay of the NSOM data with the simulation output can be seen in figure 3.11.

3.10 Results and discussion

Several adlayer sizes and thicknesses were studied to quantify the evanescent field response to the presence of the patterns. Figure. 3.8 shows an evenly spaced set of 4 photoresist regions fabricated to a thickness of 130 nm. The measured evanescent field over the bare waveguide was observed to have a uniform Gaussian profile, indicating a single bound mode (figure 3.9). This single mode behavior was optimal for quantification of the response to the presence of an adlayer. Specifically, if the waveguide contained two guided modes, the signal from an adlayer may not be distinguishable from the oscillation between the modes. As seen in figure 3.10, as light encounters the photoresist feature, there is a drop in the measured surface

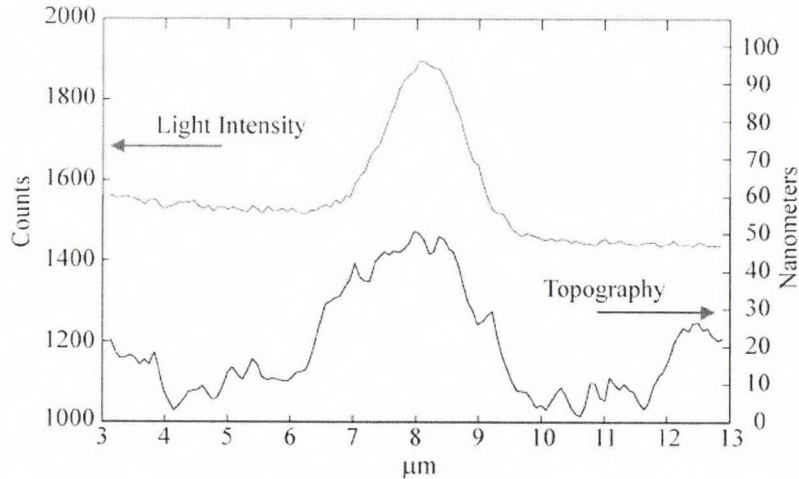


Figure 3.9. Cross-section plot of the light intensity (top) and topography (bottom) of an approximately 3 μm wide ridge waveguide etched 14 nm. Light profile indicates a single bound mode.

light intensity followed by a sharp increase at the end of the feature. The lower part of figure 3.10 shows the light intensity measured along the centerline of the 2 μm wide waveguide. The response from the BeamPROP simulations for the 8.5 μm long, 130 nm thick feature is shown in figure 3.11. The centerline scan data shown indicates that $\Delta P \sim 70\%$. The measurement and simulation results shown in figure 3.11 are in excellent agreement with respect to the normalized modulation depth of 70%. Both figures 3.10 and 3.11 indicate a strong change in the optical evanescent field when the propagating light reaches the adlayer region and past the adlayer, a large damped oscillation of the evanescent field is observed. This oscillation may be caused by the excitation of a second order mode that interferes with the guided first order mode [40]. In this case, leaky higher order mode(s) are excited due to the increase in refractive index near the core that effectively increases the core thickness. The increase in effective core thickness results in a power distribution shift where more of the optical power is contained within the core. If the thickness of the layer is large enough, the guiding conditions of the waveguide change such that the propagation of two or more modes becomes possible. Any higher order modes that become excited during the adlayer regions were no longer as tightly bound when the light travels back to the bare waveguide. The transient presence of the higher order mode with the guided mode

caused the observed oscillation in the surface evanescent field intensity. The oscillation decayed to zero when the power excited into the higher order mode was coupled back into the fundamental mode or was lost from the waveguide. This oscillation impacted the spacing of adjacent capture regions. To obtain interference free measurement from each capture region, the regions were spaced so that the light field was able to return to a uniform value. This leaky mode was also observed in the BeamPROP simulation of the light response to the features. A spacing of 200 μm was sufficient to allow the evanescent field to return to a uniform value.

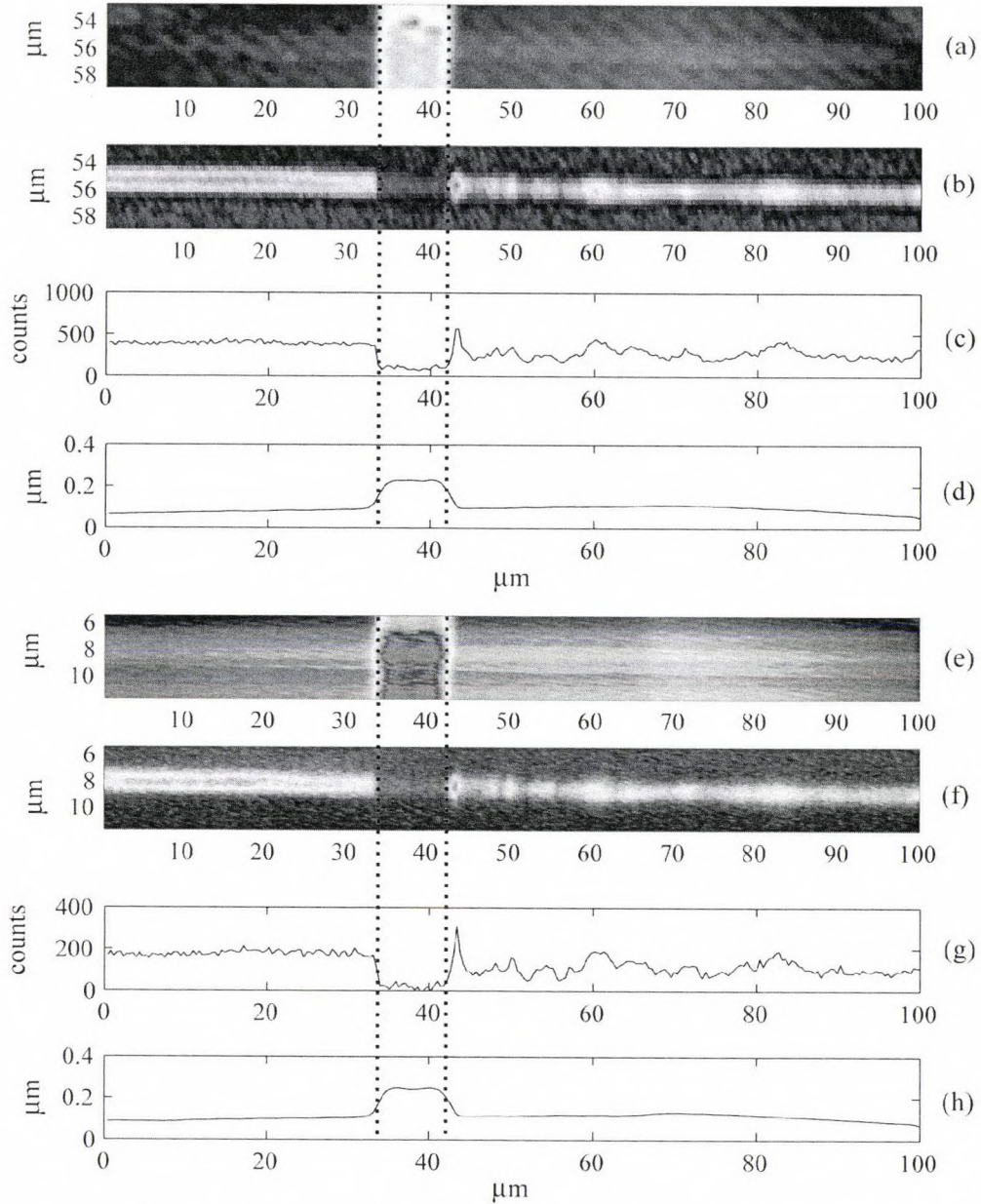


Figure 3.10: Light travels from left \rightarrow right. $\Delta P = 76.9\%$ for (c) and $\Delta P = 70.9\%$ for (g).

(a-d) Experimental light response to the second of four photoresist features. (a) Topography of $2.0\ \mu\text{m}$ wide waveguide with $14\ \text{nm}$ etch depth. Feature size is $\approx 8.5\ \mu\text{m}$ in length and $130\ \text{nm}$ thick, (b) Surface light intensity measured with NSOM, (c) Total light measured in photon counts carried in the waveguide after subtracting the background. (d) Cross-section of the topography scan showing the location of photoresist feature.

(e-h) Response to the fourth photoresist feature: (e) Topography of $2.0\ \mu\text{m}$ wide waveguide with $14\ \text{nm}$ etch depth. Feature size is $\approx 8.5\ \mu\text{m}$ in length and $130\ \text{nm}$ thick, (f) Surface light intensity measured with NSOM, (g) Total light measured in photon counts carried in the waveguide after subtracting the background. (d) Cross-section of the topography scan showing the location of photoresist feature. The two features show similar response and indicate that $190\ \mu\text{m}$ was enough spacing to allow the field to return to a uniform value.

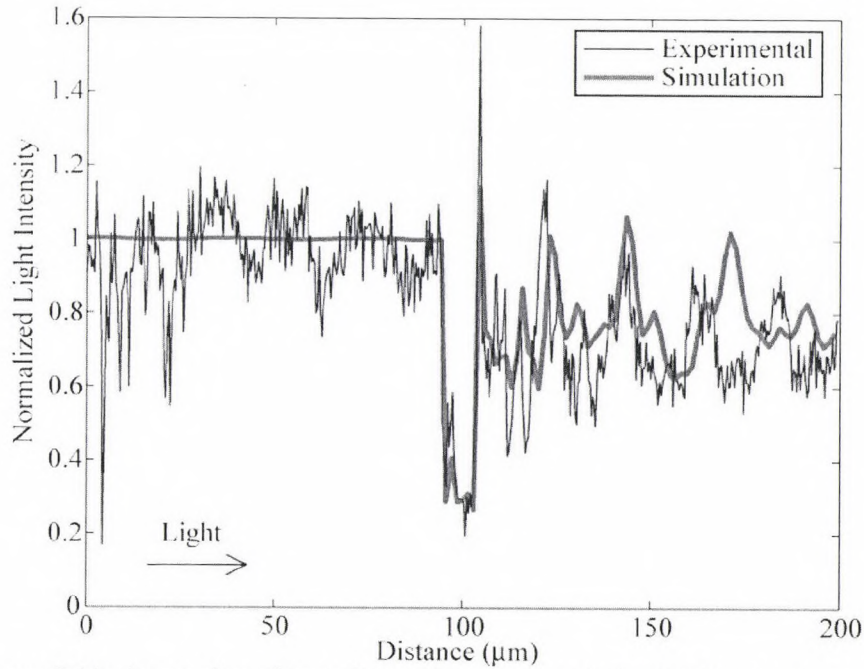


Figure 3.11: An overlay of experimental response and simulated response to the 130 nm thick, 8.5 μm long photoresist feature. Light sampled along the top surface of the core and photoresist feature. $\Delta P = 51.9\%$. Oscillation period is $\sim 25\ \mu\text{m}$.

As may be seen in figures 3.11 and 3.12, the measured evanescent field intensity at the surface of the sample decreased as the tip was scanned over the region where there was patterned photoresist. Two things were considered when looking at the surface evanescent intensity plots generated using NSOM. The evanescent field decayed exponentially as the tip was moved away from the surface of the core. Any topographical feature with refractive index lower than the core will produce this effect. This effect occurred for all sizes of topographical features even if the refractive index change was not large enough to cause a shift in the evanescent field. Therefore as the tip scanned over a photoresist adlayer, the measured field strength decreased since the tip moved away from the core/cladding interface. The second effect that occurred was the detection of the shift in the evanescent field as a response to the refractive index change. The presence of the higher refractive index material caused the light to shift up toward the adlayer out of the lower cladding. These two phenomena produced opposite effects on the light intensity measured at the surface. The tip shifting away from the core reduced the detected signal and the evanescent field shift increased the detected signal. For surface features with refractive indices similar to that of

the core, the effect of the shifting light field was larger than the tip/core distance change and the measured light tended to increase over the adlayer features. In the case of adlayers with refractive index of 1.6, the tip shifting up was the dominant effect on measured light intensity.

To investigate the dependence of signal strength on feature size, a series of adlayers of different lengths were fabricated, shown schematically in Figure 3.12, each with a height of 60 nm. The shortest length studied was approximately 3 μm . For the 3.9 μm feature seen in Figure 3.14, the drop in intensity was followed by an

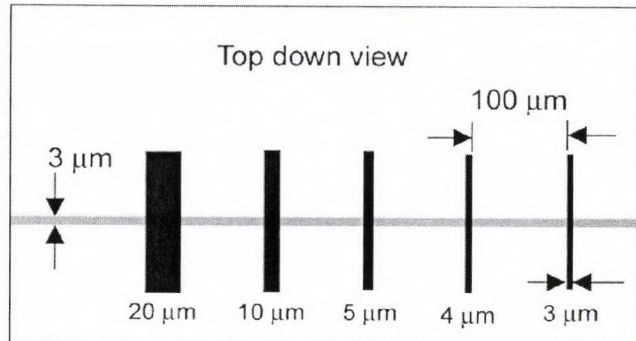


Figure 3.12. Geometry of variable size resist features patterned on the waveguide. Photoresist more closely approximated the refractive index of biological features.

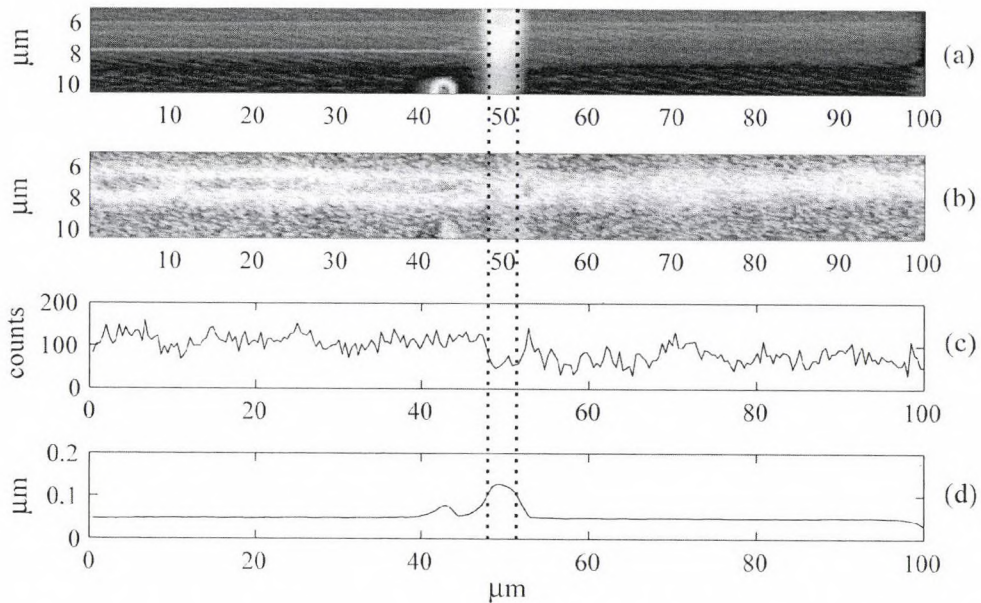


Figure 3.13. Light response to small photoresist feature. (a) Topography of 2.0 μm wide waveguide with 14 nm etch depth. Feature size is $\approx 3.9 \mu\text{m}$ in length and 70 nm thick, (b) Surface light intensity measured with NSOM, (c) Total light measured in photon counts carried in the waveguide after subtracting the background. $\Delta P = 45.6 \%$. (d) Cross-section of the topography scan showing the location of photoresist feature.

increase and then decaying oscillations indicated that the feature was large enough to cause a change in the evanescent field. A similar response was generated by the 2.7 μm adlayer length, as seen in Figure 3.14. The oscillations were definitively present when the 2D light intensity scan was analyzed rather than the total optical power (figure 3.14b). Thus, while it appears there is a minimum length of probe region that is able to generate a significant observable signal, it appears that 3 and 4 μm feature sizes still excite a measurable response in the evanescent field. Many current microarray technologies use 20 to 75 μm diameter spots, which are well over the minimum size that can cause a significant response in the evanescent field.

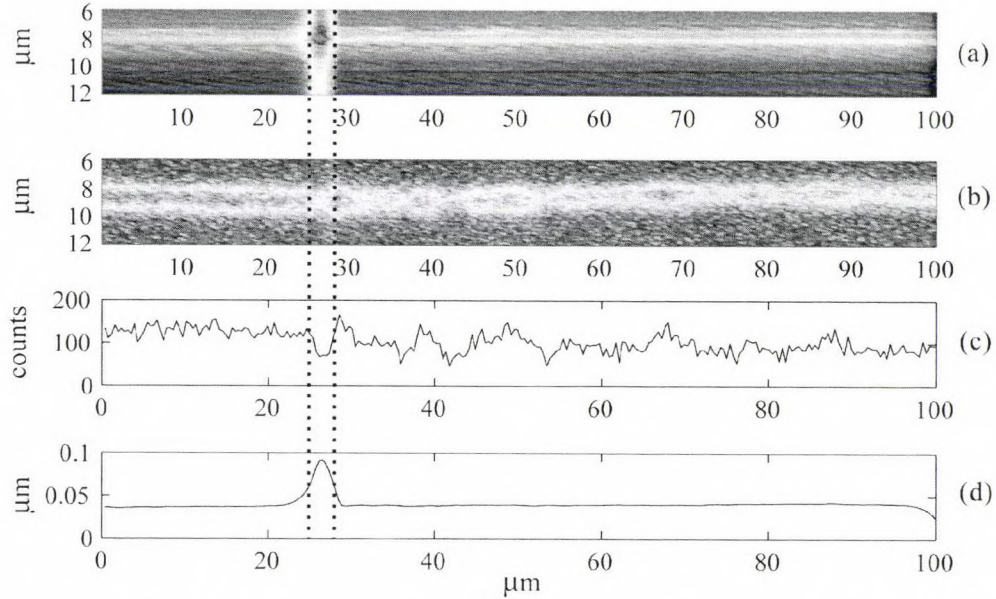


Figure 3.14: Light response to the smallest fabricated feature. (a) Topography of 2.0 μm wide waveguide with 14 nm etch depth. Feature size is $\approx 2.7 \mu\text{m}$ in length and 50 nm thick, (b) Surface light intensity measured with NSOM, (c) Total light measured in photon counts carried in the waveguide after subtracting the background. $\Delta P = 26.4\%$. (d) Cross-section of the topography scan showing the location of photoresist feature.

3.11 Conclusion

The evanescent field response in the cases that were studied point toward several conclusions. The presence of the organic material on the surface of the waveguide core excites a weakly bound mode that caused decaying interference with the bound mode. This was a result of the waveguide core dimensions being near the single mode/multi mode boundary. Any feature large enough to elicit a response in the evanescent field was also observed to excite a higher order mode over the adlayer region. This result indicated that the probe regions should be spaced sufficiently far apart to allow for the light field to return to a uniform value. For the system studied here, a spacing of 150 to 200 μm was enough to allow the oscillation to decay to zero. The evanescent field intensity, measured at the surface of the waveguide/adlayers, decreased as the tip was scanned over the adlayer region and a sharp increase in evanescent field intensity was observed after the end of the adlayer. The decrease in surface light intensity was due to the photoresist feature being at a lower refractive index than the core. The power modulation, due to the presence of the adlayer and the degree of oscillations, increased as the height and length of the adlayer increased as seen in table 3.2.

Feature	Fig 3.10c	Fig 3.10f	Fig 3.11	Fig 3.13	Fig 3.14
ΔP	76.9 %	70.9 %	51.9 %	45.6 %	26.4 %
Feature Height	130 nm	130 nm	130 nm	70 nm	50 nm
Feature Length	8.5 μm	8.5 μm	8.5 μm	3.9 μm	2.7 μm
S/N	15.9	14.6	9.11	3.99	2.79
LOD	8.5 nm	9.7 nm	14.8	21 nm	14.4 nm

Table 3.2: Power modulation values and feature sizes for photoresist features shown in the figures. S/N is the non normalized power modulation divided by the RMS noise level and the limit of detection (LOD) is the thickness of the pattern in nm that corresponds to the signal generated at the limit of detection as defined in equation 3.4.

Given the low amount of noise involved in measuring the evanescent field with the NSOM, the apparent minimum length of adlayer that generated a discernable signal was less than the measured 3 μm . The BeamProp simulation results, which contain no adjustable parameters, agree with the measured results and show the same patterns when encountering a photoresist region. These guidelines that have been determined give insight on the design of size and spacing of capture regions in further experimental devices.

Chapter 4 – Protein immunoassay on the waveguide²

4.1 Introduction

There is considerable demand for a rapid, quantitative, multianalyte sensor for the detection of biological or environmental analytes. A thin film optical waveguide built on a silicon wafer has been used as a platform for local evanescent array coupled (LEAC) detection of analyte binding. Using a visible guided wavelength and an optical waveguide core thickness of 100 nm, the evanescent field was found to be sensitive to the refractive index changes within 150 nm of the core. In this chapter, results are described from an experiment using a poly(dimethylsiloxane) (PDMS) microfluidic network to pattern a four-layer C-reactive protein (CRP) immunoassay with saturated, dilute, and zero CRP concentrations on the surface of the LEAC sensor. The immunoassay is carried out by immobilizing Anti-CRP on the waveguide using a Avidin/Biotin non-covalent link and then allowing buffer solutions containing the analyte to incubate with the antibody regions. The surface evanescent field profile for each concentration of CRP was determined using near field scanning optical microscopy (NSOM). The measured values compared well to simulated responses obtained via the beam propagation method (BeamPROP). Using the topography capabilities of the NSOM the pattern heights were measured. For saturated CRP the complex height was 14.8 nm, for the dilute concentration the height was 12.4 nm, and the height with no bound CRP was 11.6 nm. The measured evanescent field modulation was $\Delta P =$

²Text from this chapter first appeared in a manuscript: Stephens, Matthew D. Xinya He, Rongjin Yan, Charles S. Henry, Kevin L. Lear, David S. Dandy, "Evanescent Field Response of a Planar Optical Waveguide to a Quantitative Immunoassay Measured using Near Field Scanning Optical Microscopy," Submitted on Aug 22, 2009 to Analytical Chemistry.

23% for the saturated CRP, 20% for the dilute CRP pattern, and 18% for no CRP, demonstrating the quantitative capabilities of the LEAC biosensor.

4.2 Protein concentration assay using evanescent field response

This chapter describes progress toward development of a label-free method of detecting CRP (analyte) binding through a shift in evanescent field intensity around an optical waveguide. This study was a step in the process of developing an integrated device for biosensing using relevant immunoassay chemistry and presented a more realistic representation of a bioassay than the surrogate polymer features described in

chapter 3. The biorecognition elements (anti-CRP probes) were patterned in an array immobilized directly onto the surface of the core of a planar waveguide. As analyte in solution binds to a complementary probe region, the effective index of refraction and biological adlayer thickness both change, thereby changing the optical properties of the

waveguide cladding. These changes cause a spatial shift in the evanescent field intensity. The thickness of the core was engineered so the evanescent field was able to interact with the cladding layers tens to hundreds of nanometers from the core. The benefit of using this type of sensor is that it locally detects the direct analyte binding to the immobilized probes on the waveguide surface. There is no labeling of the analyte or addition of labeled probes needed for detection or quantification of binding.

Results will be presented that demonstrate the quantitative response of the evanescent field of a waveguide to a patterned immunoassay. The immunoassay was patterned using a PDMS microfluidic network (μ FN) [44-50]. The anti-CRP/CRP system (see Figure 4.1) was

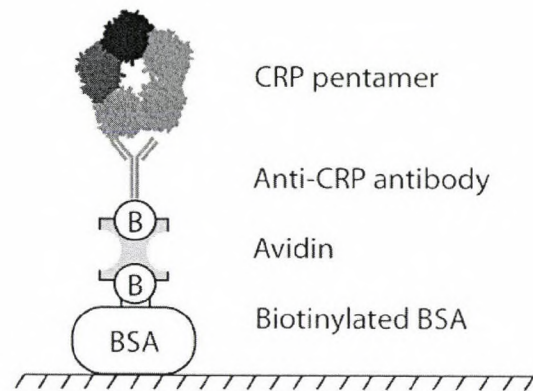


Figure 4.1: An immunoassay complex consisting of biotinlyted BSA, Avidin, Anti-CRP and CRP.

selected to be representative of typical antibody/antigen interaction, and it is an important oxidative stress biomarker. The probe regions for each analyte concentration were separated from one another on the waveguide surface to allow the signal from each region to be determined independently. This segregation allows the placement of multiple probe regions along the waveguide. The microfluidic system was operated to allow simultaneous detection of several concentrations of analytes on the same waveguide. Although the same probe was patterned multiple times along the surface, it would be straightforward to immobilize a different probe type in each region, thereby making the device multianalyte capable.

The four-layer CRP immunoassay was patterned using a PDMS microfluidic channel oriented perpendicular to a waveguide fabricated on a silicon wafer (See figure 4.2b). Several concentrations of CRP were allowed to incubate with the anti-CRP. A high concentration was studied to ensure that nearly all the available binding sites on the surface were filled with protein. A dilute concentration was used to pattern less than a monolayer of protein. Also, there were some patterns that had the final patterned layer as anti-CRP, because

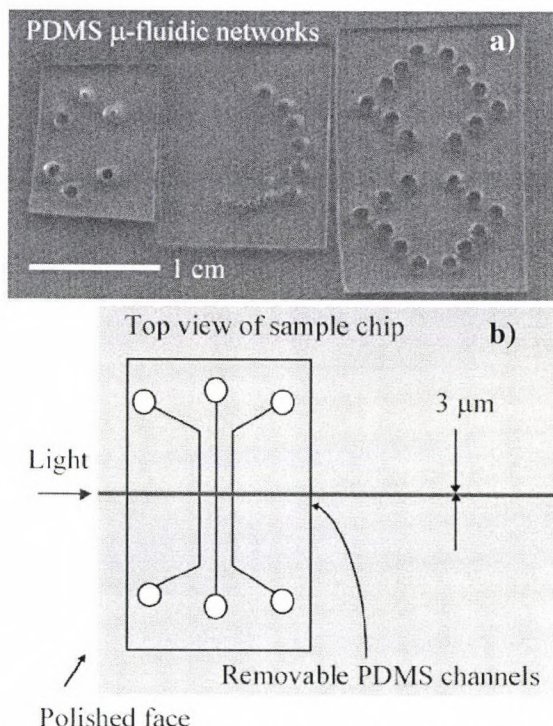


Figure 4.2: a) Molded PDMS stamps with 3, 6, and 12 channels for patterning. b) Three-channel network attached to a waveguide chip.

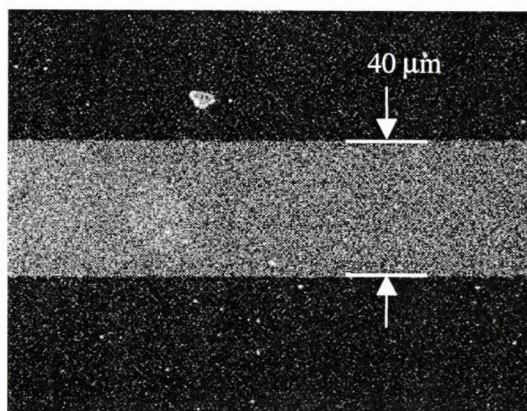


Figure 4.3: Fluorescence image of 4-layer immunoassay with FITC labeled Anti-CRP patterned using a PDMS channel

buffer with no CRP was added to that channel. The CRP used as analyte here was labeled with a fluorescent tag FITC to allow redundant quantification of the CRP binding using fluorescence microscopy. An example of this CRP immunoassay using a PDMS channel with a width of 40 μm is shown in figure 4.3. Xinya He and Brian Murphy carried out the immunoassay patterning on the waveguide surfaces [51,52].

4.3 Waveguide fabrication

Waveguides were fabricated as detailed in Chapter 2. But in brief, they were fabricated by depositing a 100 nm silicon nitride film using reactive ion sputter deposition (Nordiko 7000, Inverness Medical, Louisville CO) on a thermally oxidized silicon wafer (2 μm SiO_2 , Noel Technologies, Campbell, CA). Standard photolithography techniques were used to mask for the creation of waveguides out of the nitride film using Microposit S1818 positive photoresist (Rohm and Haas Electronic Materials Corporation). After masking, the nitride surface was etched 15 to 20 nm to form 2 μm wide ridge waveguides using a 4:1 $\text{CF}_4:\text{O}_2$ plasma etch (Technics Micro RIE Series 800) at 50 W and 250 mTorr. The wafer was then scribed on the back surface and cleaved in preparation for edge polishing to expose a facet of the nitride film for end-fire light coupling using a laser diode and single mode optical fiber. This fabrication procedure resulted in a single mode of light propagation at 654 nm wavelength and an evanescent field large enough to extend into the patterned proteins and surroundings up to 150 nm away from the waveguide surface.

4.4 Immunoassay patterning

Poly(dimethylsiloxane) (PDMS) was used to form a μFN for patterning the immunoassay on the SiN_x waveguide surface (See figure 4.3a). Using the PDMS μFN allowed the remainder of the surface to remain free from nonspecific binding and the dimensions of the patterned regions could be easily controlled. The volume of fluid needed to fill the channels was usually only a few microliters, reducing the reagent costs for the system. Prior to patterning, the nonreacted oligomers in the PDMS were removed using a solvent extraction process [51,52]. After curing the

PDMS in a 65°C oven for 2 h, the stamps were placed in stirred triethylamine for 2 h with a solvent replacement after 1 h. Additional oligomer was extracted from the stamps by treating for 2 h in stirred ethyl acetate and then 2 h in stirred acetone. After oligomer extraction, the stamps were placed in a 65°C oven for 2 h to evaporate solvents.

Before the stamps were used to pattern proteins, they were exposed to air plasma for 45 s at a power of 18 W (Harrick Scientific, PDC-32G). The stamps formed a non-covalent seal with the waveguide surface and were able to be removed when the protein patterning was finished.

The immunoassay was formed in a series of four patterning steps.

1. 2.5 mg/mL Biotin-BSA was patterned for 90 min on the SiN_x followed by a flush using phosphate buffered saline (PBS, 50 mM phosphate, 0.9% NaCl, pH 7.4)
2. Avadin was added followed by a PBS flush
3. 2.5 mg/mL biotin-anti-CRP was added and allowed to incubate for 30 min followed by a PBS flush
4. Differing concentrations of FITC-labeled CRP were allowed to incubate for 30 min followed by a PBS flush and removal of the PDMS μFN.

4.5 NSOM of protein patterns

Near field scanning optical microscopy (WiTec alphaSNOM) was used to quantify the effect of the patterned immunoassay on the surface evanescent field intensity. The NSOM acquired simultaneous topography and surface evanescent field intensity by means of a cantilever tip that is scanned across the surface of the sample. The tip was in contact with the surface of the waveguide and collected light from the evanescent field through a 100 nm diameter aperture. This collected light was amplified with a PMT and a 2D-intensity plot of the local evanescent light field was created. The topography of the sample was determined through deflection of the cantilever tip in contact with the surface. The data was analyzed using the Image Control (WiTec) image analysis software or exported and plotted with Matlab (The Mathworks).

4.6 Evanescent field response

Using a three channel PDMS μ FN (figure 4.2b), patterns were created on a waveguide surface and subsequently analyzed with the NSOM to measure the surface evanescent field intensity. The three channels were incubated with CRP concentrations of 600 $\mu\text{g}/\text{mL}$, 0.6 $\mu\text{g}/\text{mL}$, and 0 $\mu\text{g}/\text{mL}$ of CRP in PBS. The NSOM was used to take $100 \mu\text{m} \times 20 \mu\text{m}$ scans along the waveguide with the tip in contact with the surface, simultaneously collecting topography data and evanescent field intensity. The μ FN used to pattern the samples for NSOM analysis had channel widths of approximately 75 μm . The four-layer immunoassay thickness measured by the NSOM

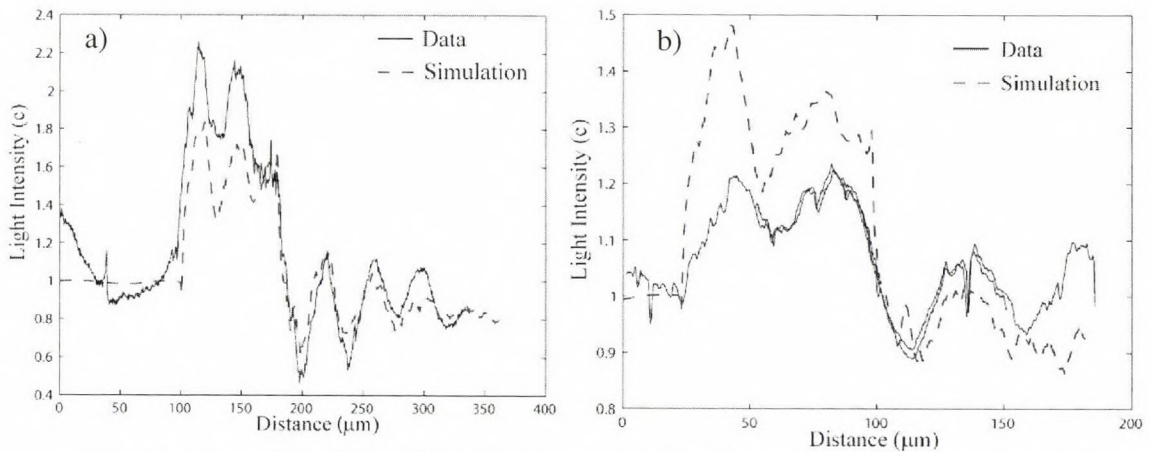


Figure 4.4: Two 75 μm long features on waveguide. Light response results to the features with CRP concentrations of a) 600 $\mu\text{g}/\text{mL}$ and b) 0.6 $\mu\text{g}/\text{mL}$ respectively. Data from NSOM scans are shown as solid lines and the BeamPROP simulation results are shown as dashed lines. Oscillation period is approximately 40 μm .

was 12 to 18 nm after drying, depending on the CRP concentration. To more readily quantify the average power in the waveguide, the 2D light intensity image for each scan area was condensed into a 1D line where each value was the light intensity at each point along the waveguide. As seen in Figure 4.4, light is propagating from left to right and as the light encounters the pattern, the measured surface intensity increases. After the pattern, an oscillation in light intensity was observed. This oscillation was caused by the excitation of a second order mode that interfered with the guided first order mode. In this case, the higher order mode(s) may become excited due to the increase in refractive index near the core, which effectively increases the core thickness.

The increase in effective core thickness resulted in a power distribution shift where more of the optical power was contained within the core. If the thickness of the layer was large enough, the guiding conditions of the waveguide change such that the propagation of two or more modes became possible. Any higher order modes that became excited during the patterned region were no longer as tightly bound when the light travels back to the bare waveguide. The transient coexistence of the higher order mode with the guided mode caused an observed oscillation in the surface evanescent field intensity. The oscillation decays to zero when the power in the higher order mode was coupled back into the fundamental mode or was lost from the waveguide.

CRP Concentration	Pattern thickness	Measured ΔP	Simulated ΔP
0 $\mu\text{g/ml}$	11.6 nm	18.2 %	21 %
0.6 $\mu\text{g/ml}$	12.4 nm	19.9 %	22 %
600 $\mu\text{g/ml}$	14.8 nm	23.3 %	25 %

Table 4.1: CRP concentration/pattern thickness vs. intensity modulations.

The data displayed in Table 4.1 show the response to all three immunoassay concentrations and predicted power modulation (R. Yan) from using the BeamPROP software with no adjustable parameters in the software model. The two-dimensional simulation results were obtained using commercial software by RSoft and these were in agreement with the laboratory results. The incident beam was assumed to be the TE mode at a wavelength of the 654 nm. The longitudinal light intensity along the waveguide and the BPM simulation results are shown in Figure 4.4. The experimental data is shown as a solid line and the results of the BPM simulation are shown as a dashed line. For the simulation profile shown, the high CRP pattern thickness was 15 nm and was assumed to have a refractive index of 1.45, a value typical of organic material. Figure 4.4 shows the total detected light intensity along the waveguide for two different concentrations of the CRP antigen. The high concentration of CRP (600 $\mu\text{g/mL}$), which corresponds to saturated monolayer analyte coverage, yields a ΔP value of 23%. For the low

concentration of CRP (0.6 $\mu\text{g/mL}$), which was expected to have less than a monolayer of CRP bound to the surface, the observed ΔP value was 19.9%. The observed power modulation for no CRP present was 18.2%. The evanescent field undergoes a larger power shift for the higher concentration of CRP, demonstrating the quantitative ability of this sensor. This observed increase in ΔP with CRP concentration was supported by the numerical BeamPROP simulations (R. Yan).

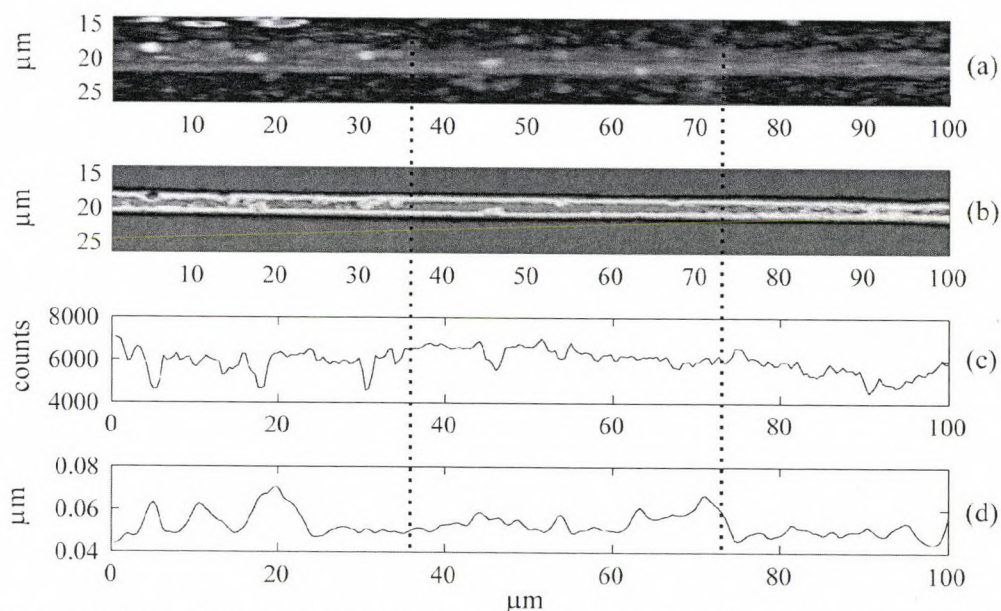


Figure 4.5: Control feature with no captured CRP. (a) Topography of 2.6 μm wide ridge waveguide with 13 nm etch depth. Feature size is $\approx 40 \mu\text{m}$ in length and 4.9 nm thick, (b) Surface light intensity measured with NSOM, (c) Total light measured in photon counts carried in the waveguide after subtracting the background. $\Delta P=7.3$ for buffer only added to the μFN . (d) Cross-section of the topography scan for the immunoassay feature.

To determine the effect of pattern size on evanescent field response, an additional experiment was done with a three-channel PDMS μFN using channels 40 μm wide. Figures 4.5 to 4.7 show the topography of the waveguide and the immunoassay pattern, the light intensity image over the same area as the topography scan, and the total light intensity in the waveguide. Figure 4.5 shows the results for the 3.4 nm thick pattern with no CRP added. As can be seen, due to the nonspecific binding, the light field response of only the attached antibody can not be seen

graphically. However, calculating the ΔP with equation 3.1 indicated a signal change of 7 %.

Figure 4.6 shows the results for the 9.0 nm thick pattern with a less than monolayer coverage of CRP. The average intensity of the light field increased as it encountered the protein layer and $\Delta P=13\%$ for low CRP concentration. Figure 4.7 shows the results for the 10.6 nm thick pattern resulting from incubation with a high concentration of CRP. The signal change for the high CRP concentration was calculated to be 17 %.

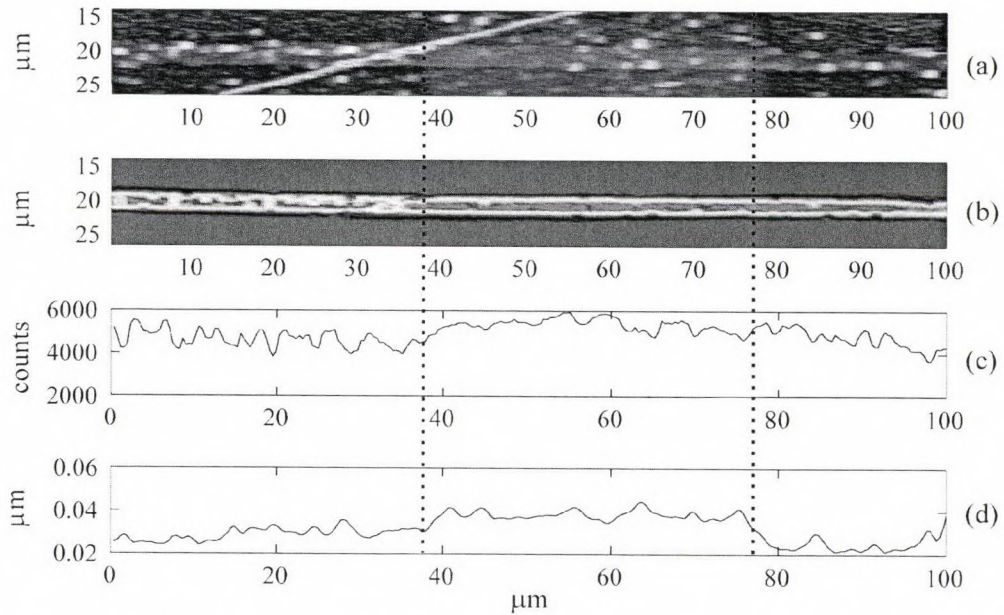


Figure 4.6: Light response to low CRP concentration. (a) Topography of 2.6 μm wide ridge waveguide with 13 nm etch depth. Feature size is $\approx 40 \mu\text{m}$ in length and 9.0 nm thick, (b) Surface light intensity measured with NSOM, (c) Total light measured in photon counts carried in the waveguide after subtracting the background. $\Delta P=13.0\%$ for low [CRP]. (d) Cross-section of the topography scan for the immunoassay feature.

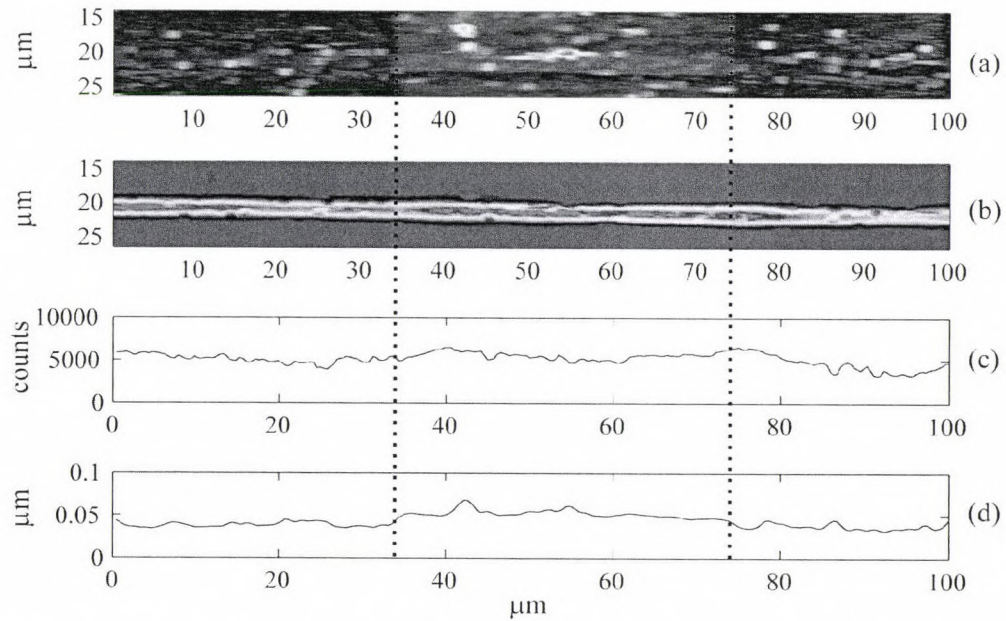


Figure 4.7: Light response to high CRP concentration. (a) Topography of 2.6 μm wide ridge waveguide with 13 nm etch depth. Feature size is $\approx 40 \mu\text{m}$ in length and 12.8 nm thick, (b) Surface light intensity measured with NSOM, (c) Total light measured in photon counts carried in the waveguide after subtracting the background. $\Delta P=16.6\%$ for high [CRP]. (d) Cross-section of the topography scan for the immunoassay feature.

CRP Concentration	0 $\mu\text{g/ml}$	0.6 $\mu\text{g/ml}$	600 $\mu\text{g/ml}$
Pattern thickness	4.9 nm	9.0 nm	12.8 nm
Measured ΔP	7.3 %	13.0 %	16.6 %
S/N	4.85	6.26	5.67
LOD	2.19 nm	2.9 nm	4.5 nm
LOD Concentration	-	0.441 $\mu\text{g/ml}$	

Table 4.2: Power modulation for 40 μm channel width for quantitative CRP immunoassay. S/N is the non normalized power modulation divided by the RMS noise level and the limit of detection (LOD) is the thickness of the pattern in nm that corresponds to the signal generated at the limit of detection as defined in equation 3.4. The limit of detection concentration is the concentration of CRP that would produce the detection signal indicated in equation 3.4.

4.7 Conclusion

The specific binding of protein molecules, CRP in this case, was directly detected via monitoring of the evanescent field at the surface of a planar waveguide. The presence of the immunoassay proteins on the surface of the waveguide core excites a weakly bound mode that caused decaying interference with the bound mode. This phenomenon was a consequence of the waveguide core dimensions being near the single mode/multi mode boundary. Any feature that was large enough to produce a response in the evanescent field was also observed to excite a higher order mode over the patterned region. This excitation process indicated that the probe regions should be spaced 500 μm apart to allow for the light field to return to a uniform value.

The detected power changed as the amount of CRP bound to anti-CRP changed, that is, as the target concentration changed. The increase in coverage of CRP in the pattern increased the refractive index of the upper cladding next to the core and the degree of light response also increased. The observed results from monolayer coverage showed a ΔP of 17% to 23.3% and less than monolayer coverage showed a ΔP of 13% to 19.9% depending on the pattern size. The observed power modulation for the two channel sizes indicated that the ΔP would be larger for larger feature lengths. This trend agreed with BeamPROP simulation results for the light response to the patterns. This indicated that the light response was quantitative with respect to the concentration of CRP for this waveguide sensor. According to the noise levels observed in the light signal, the less than monolayer coverage results were above the limit of detection as defined by Equation 3.4. A lower limit of detection can be obtained if the signal from the evanescent field can be measured without the surface topography impacting the signal. As a next step in the design of the sensor, buried detector elements were used to measure the evanescent field intensity. The buried detectors were at a uniform distance from the waveguide core and were not subject to surface topography effects when measuring the field and are discussed in Chapter 5.

Chapter 5 – Buried detector sensing

5.1 On chip evanescent field detection

This chapter describes results obtained using a planar waveguide fabricated on a chip that contained underlying (buried) silicon photo-detectors. The detectors were located 1.0 μm to 1.4 μm away from the core of the waveguide in order to intersect with the evanescent field in the lower cladding. The detectors converted the optical field received from the evanescent field to electrical signals. A change in signal received by a detector indicates a change in the refractive index of the upper optical cladding. For example, a change in refractive index may indicate the presence of adsorbed species on the upper surface of the waveguide. The detector operates in real time and indicates the degree of coverage of a species adsorbed to the waveguide surface through a relative shift of the evanescent field.

The buried detector format provides significant opportunities for localized detection of chemical or biological analytes in complex milieu through monitoring of the evanescent field [53]. The shift in the detected optical signal as a result of bulk refractive index changes on the surface of the waveguide is presented as proof of principle. In addition, the predicted response to the refractive index changes via numerical modeling is compared with the measured detector response.

5.2 Buried detector concept

To form an evanescent field detection array on the waveguide chip, the photoelectric effect of a semiconductor material was used. The photoelectric effect is the phenomenon by which a material will release electrons when it absorbs energy from light or other electromagnetic

radiation. In semiconductors, low energy light such as visible photons can promote electrons out of the valence band and into the conduction band where they can be induced to flow when the material is biased with an electrical voltage [55]. For example, amorphous, polycrystalline silicon (polysilicon) located in the lower cladding of a planar waveguide can form a photodiode and detect adsorbed evanescent field (see figure 5.1 [54]). For this waveguide, which propagates 654 nm light, the polysilicon was able to absorb photons of this energy and respond by releasing electrons, which are measured to determine photocurrent [56, 57].

An advantage of buried detector array sensing was that the sensing elements were always located at a constant distance away from the core of the waveguide. This detection paradigm had the benefit of measuring the shift in the field for a capture region without needing to observe secondary effects such as field oscillation to confirm a response. With a buried detector array the field intensity was also determined without the added complication associated with the surface topography affecting the core-detector distance. Two buried detector designs were studied to determine the properties of the waveguide and the detector response to refractive index changes on top of the waveguides. Figure 5.2 shows the basic geometry of the

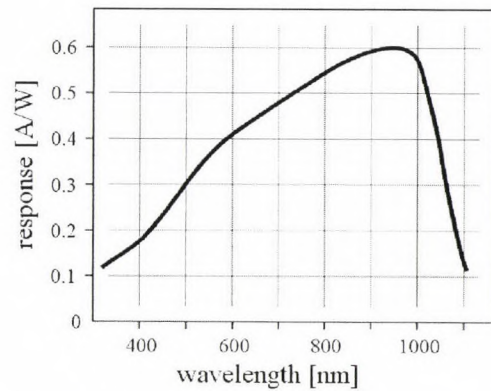


Figure 5.1: Silicon photodiode response versus wavelength of the incident light [54].

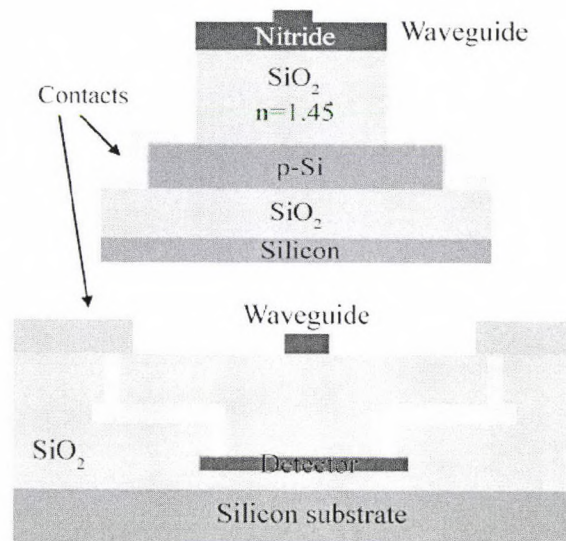


Figure 5.2: Cross sections of two buried detector designs. (Top) CSU design incorporating a solid polysilicon detector strip under the ridge waveguide and (Bottom) Avago design with discrete detector elements under a rib waveguide.

two detector designs studied. The first device studied was a detector that was designed and fabricated in the CSU cleanroom from a multilayered film sample deposited at the Army Research Lab (ARL). The second device was fabricated with the cooperation of Phil Nikkel and his colleagues at Avago Technologies.

The predicted response generated for an 8.5 μm long feature of refractive index 1.56 using a detector array is shown in figure 5.3. As seen on the left part of the figure, the simulated detectors were placed 0.5 μm away from the core of the waveguide. The response of the field to an increase in refractive index of the upper cladding region, as predicted by the model, is a shift in the guided light out of the lower cladding and toward the feature. The shift in field due to the feature causes the detected power in the lower cladding to decrease. Figure 5.3 compares this

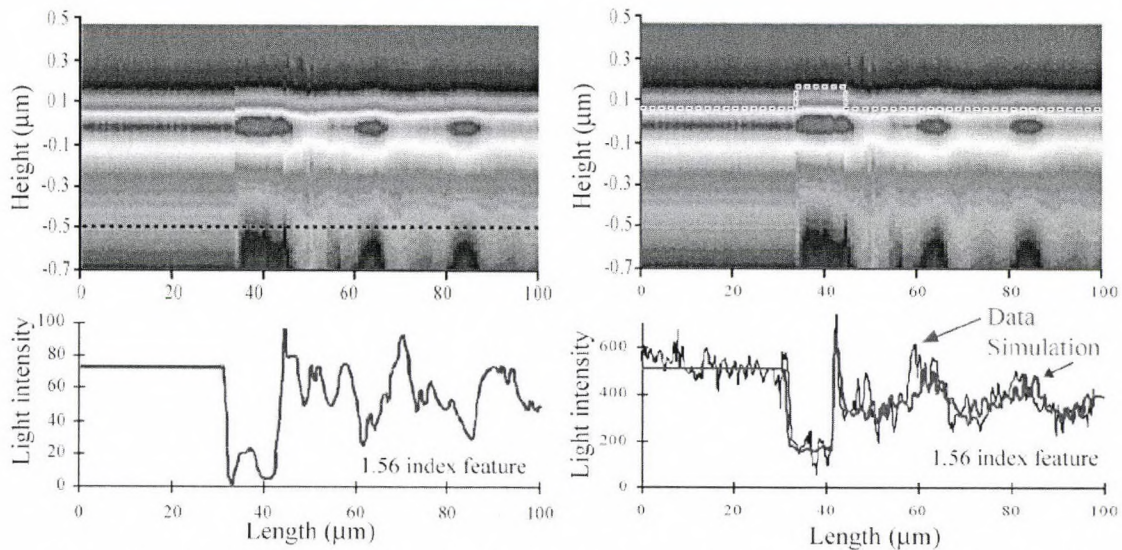


Figure 5.3: Light intensity cross section for a SiN_x waveguide with 8.5mm feature (top). Simulated detector array response & NSOM with simulated response to feature (bottom).

with the response to the same feature simulated with BeamPROP and measured by NSOM. The majority of the response seen in the figure on the lower right was due to the tip shifting up over the patterned feature and a smaller amount of evanescent field power was detected even though the field intensity above the core increased.

The buried detector concept has several disadvantages. The polysilicon detector regions in the lower cladding were designed to intercept the evanescent field and convert the photons to a current that could be measured. The presence of the detector regions converted the guided power in the waveguide from optical to an electrical signal. This increased the propagation loss from the waveguide and reduced the amount of waveguide that was effective in guiding light. The detectors also have a size larger than the NSOM tip aperture, so the resolution of the light profile as measured using the detectors would be less than if the field was measured using NSOM.

There were also several advantages to using a detector array rather than NSOM to detect the evanescent field. The detector array can measure the evanescent field while the top of the waveguide was open so sample may be delivered to the surface using a microfluidic network. The detectors were also capable of measuring the intensity along the length of the waveguide simultaneously and in real time, hereby enabling the monitoring of binding of analyte(s) for all probe regions on the waveguide at the same time. The on-chip detection of the waveguide power profile had the advantage of requiring less power, cost and instrumentation than the NSOM detection method.

The results from the BeamPROP simulations indicated that the buried detector array was a better way of profiling the evanescent field response to features of all thicknesses. Therefore, the fabrication and response of the detector arrays were carried out to determine the optical and electrical properties of the integrated devices as well as the expected response to index changes above the waveguide.

5.3 CSU detector array fabrication

As a first step in looking at the application of a buried detector to profile the evanescent field for this sensor device, a prototype detector was designed and fabricated in the CSU semiconductor cleanroom. In order

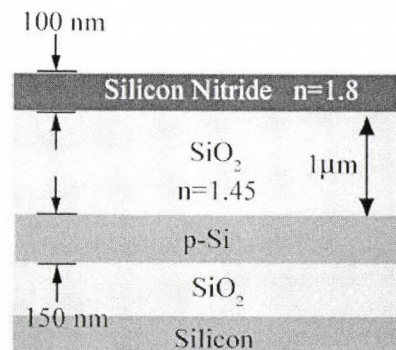


Figure 5.4: Wafer composition and dimensions for CSU detector

for a buried detector to be fabricated, a multilayer film structure from ARL was used as a starting material. Figure 5.4 shows the initial multilayer film structure. The substrate was a thermal oxide wafer and three films were deposited on the substrate in order to form the sensing, cladding and waveguide layers. The thermal oxide isolated the polysilicon detector layer from the silicon substrate to allow the bias current of the detector to only travel through the polysilicon. An additional layer of silicon dioxide provided optical isolation between the core of the waveguide and the detector region while still allowing the field to reach the detectors.

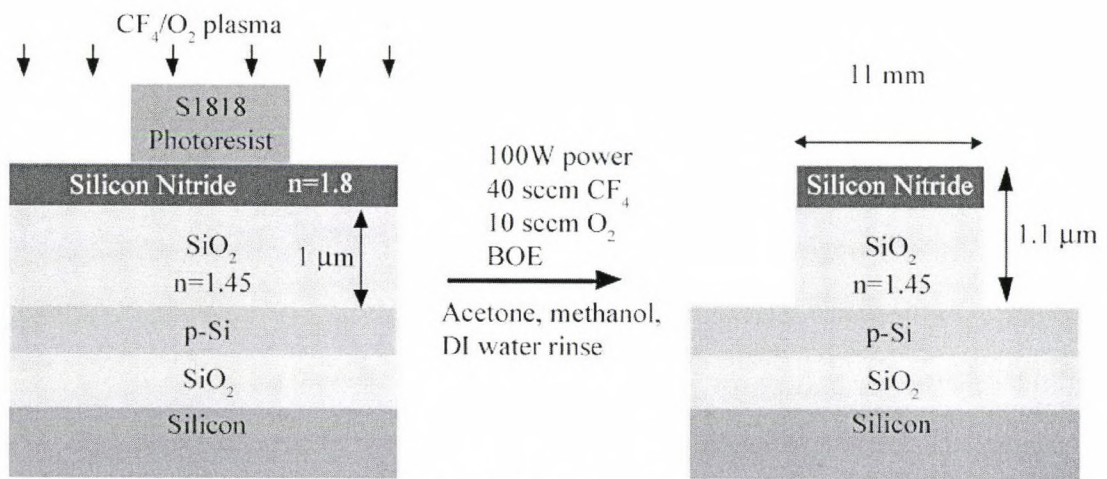


Figure 5.5a: First step in fabrication of CSU buried detectors: Mask with photoresist for CF_4/O_2 and BOE etch steps for plateau formation.

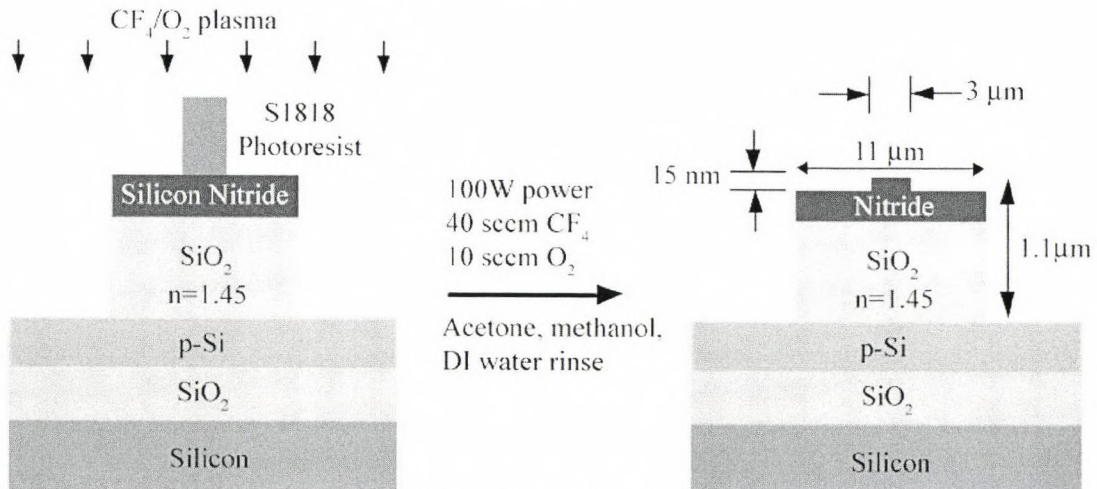


Figure 5.5b: Photoresist deposition for masking for waveguide fabrication for CSU buried detector design.

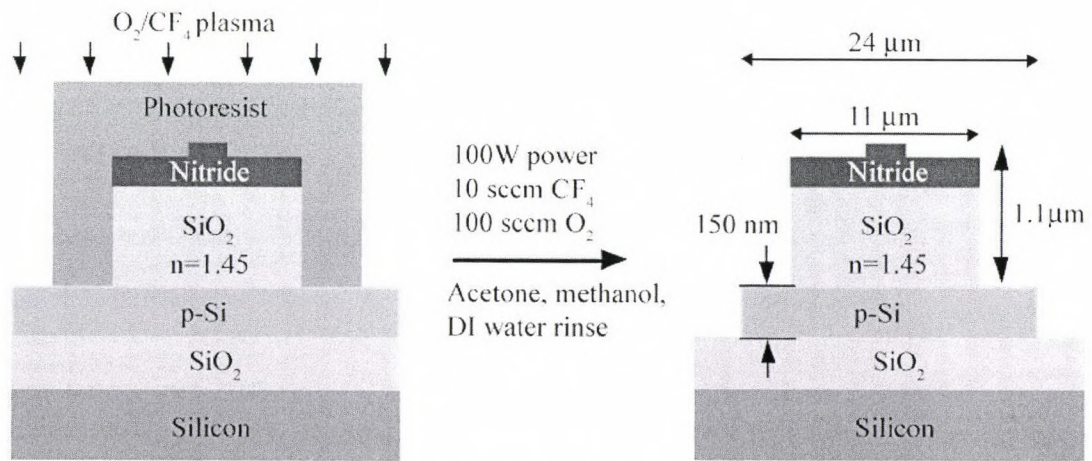


Figure 5.5c: Polysilicon detector strip fabrication for CSU buried detector

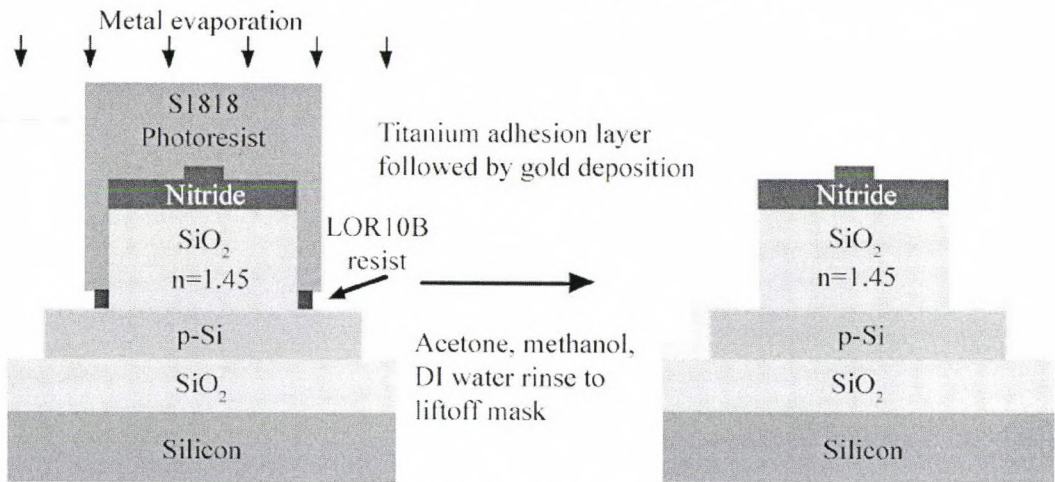


Figure 5.5d: Masking and metal evaporation for contact electrodes for CSU detector design

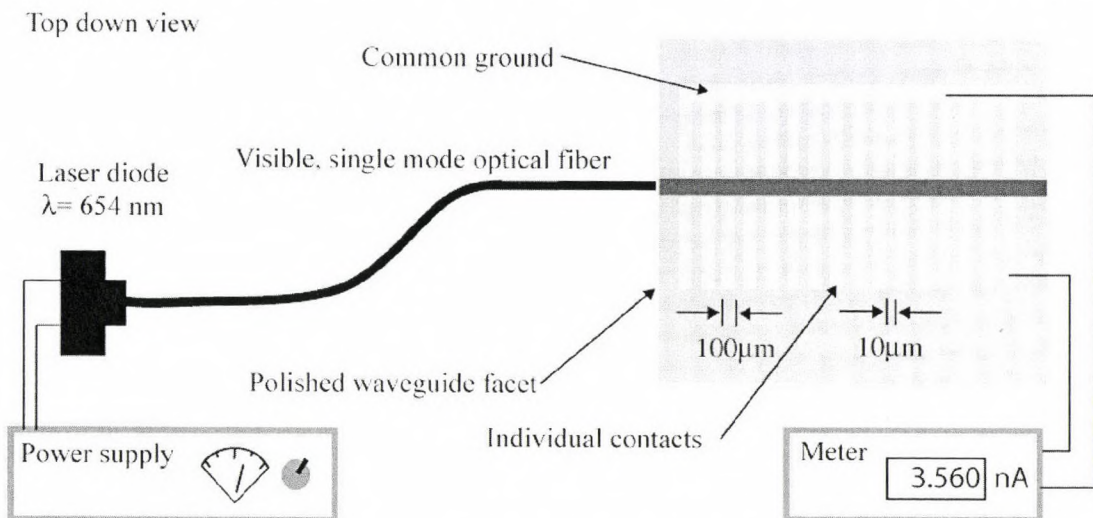


Figure 5.6: Overall view of CSU detector array with laser diode and power supply and meter to measure the photocurrent response of the detectors

To form the waveguide and sensor complex, a series of etching steps were used to remove the deposited films. The first fabrication step (figure 5.5a) was to mask an 11 μm strip with photoresist (S1818) and use CF_4/O_2 plasma to etch through the silicon nitride and silicon dioxide layers to expose the polysilicon layer. Buffered hydrofluoric acid (BOE) was used to remove any remaining silicon dioxide on the polysilicon layer to allow for good electrical contact between the polysilicon and the metal contact. A dry etch was used to accomplish the initial etch instead of a wet etch in order to define the 11 μm wide area with minimal undercutting of the mask. The buffered HF removed photoresist and silicon nitride but the plasma etch was selective in etching the nitride and SiO_2 at a much faster rate than the photoresist mask (table 5.1). The next fabrication step was to mask a 3 μm wide strip on top of the plateau to form the ridge waveguide (figure 5.5b). Applying the CF_4/O_2 plasma for 7 seconds etched the nitride layer 15 nm and formed the waveguide ridge. The next step was to remove most of the polysilicon from the wafer leaving 6.5 μm of polysilicon on each side of the waveguide block allowing metal to contact each side (figure 5.5c). The sample was masked with a 24 μm wide photoresist feature and the sample was etched with high oxygen content plasma. The oxygen plasma selectively etched the polysilicon and did not etch photoresist or silicon dioxide. After these etching steps, the sample was masked with two layers of photoresist to form a liftoff mask for removing metal that was evaporated on the surface. First a photoresist called LOR10B was spincoated on the surface and baked. Then a layer of S1818 was spun on top of the LOR10B coated sample and then baked. The sample was then exposed and developed as normal. The LOR10B resist layer developed and washed away at a faster rate than the S1818. This process formed a structure that was undercut to allow for the solvent rinse to dissolve the masking layer after metal evaporation (see figure 5.5d). Two layers of metal were evaporated on the sample. Titanium was used as an adhesion promoter for gold, which formed the electrically conductive contacts that connected to the two sides of the polysilicon strip and formed detectors. The metal contacts that were deposited

were 100 μm wide with a spacing of 10 μm . The contacts were all connected to the same detector strip and discrete detectors were not formed for this particular design. Current flow between adjacent detectors was reduced by minimizing the distance between the ends of the electrode pairs. After the metal was deposited and the excess removed through acetone/methanol/water rinses, the edge of the sample was polished to prepare it for light coupling. The sample was then attached to a fiber and laser diode and was ready for initial light intensity profiling using a benchtop current reader. Figure 5.6 shows a diagram of the coupled waveguide and the dimensions of the detector array.

5.4 CSU detector response

To determine the photocurrent response of each detector, one contact probe of the meter (Keithley 2400) was placed on the common ground pad and the other placed on one of the individual contacts. The detector region was biased with 10 volts. It was observed that the detector array would respond to environmental light. The photocurrent was measured five times for three detectors with the bench light on and off. The photocurrent response was observed to increase by approximately 0.2 mA, or 4 % of the total current, each time the detector was monitored with the bench light on. This initial analysis indicated that the detector regions were responding to the environmental light and thus should respond to changes in guided light in the waveguide. The next step in looking at this buried detector design was to profile the detector response for the bare waveguide with air as the upper cladding. The results of the detectors for the bare waveguide are shown in figure 5.7a.

To obtain a valid response from each detector, the signal from a photodetector must be normalized to avoid signal variations due to changes in background signal. This is accomplished using a reference detector and is analogous to the normalization done to obtain the power modulation values for the experiments in chapters 2 and 4. Changes in the environment or in the power supply can effect the input power launched into the waveguide. To obtain a signal from

each detector, the photocurrent for each detector signal was normalized using the photocurrent response of a reference detector that was located away from any features patterned on the surface.

An experiment was done to determine the change in the detector response when the bulk refractive index of the upper cladding was increased. The detector response was measured with air as the upper cladding and then vegetable oil was added on top of the waveguide to increase the cladding index. As seen in figure 5.7b, the photocurrent detected for the bare waveguide was lower than the current detected after the upper cladding index was changed. Based on the BeamPROP simulation results seen in figure 5.3, this was not the expected result of this experiment. The increase in upper cladding index should have resulted in lower power measured by the detectors due to an upward shift in the evanescent field. One possible explanation for this effect may be that since the oil was not confined to the top surface of the waveguide, some oil flowed between the fiber and the polished face of the waveguide. The oil then formed a more efficient coupling connection due to better index matching in the fiber/air/waveguide interface.

Determining the loss characteristics of this waveguide and detector array is a useful calculation for comparison with other structures. The loss in decibels of an optical waveguide is defined as:

$$dB_{loss} = 10 \log_{10} \left(\frac{P_0}{P} \right) \quad \text{Equation 5.1}$$

Where P_0 is the initial power in the guide and P is the power measured at some point down the length of the guide. A more accurate loss calculation was done using a collection of data to determine the loss rather than a single point. The data was fit using a linear or exponential form as seen in equations 5.2 and 5.3:

$$LOG_{10}(I_{PC}) = m * (D) + LOG_{10}(I_0) \quad \text{Equation 5.2}$$

$$I_{PC} = I_0 * e^{-\lambda * D} \quad \text{Equation 5.3}$$

where I_{PC} is the photocurrent at each detector, m is the slope of the line found by minimizing the sum of squared differences between the data and the best fit line, D is the detector number, I_0 is

the initial photocurrent coupled into the waveguide, and λ is the exponential decay constant. The loss in dB/mm for the propagation of light in a waveguide was found by using equation 5.4 or 5.5.

$$\begin{aligned} Loss_dB/mm &= m * 100 \\ Loss_dB/mm &= LOG_{10}(e^{-\lambda}) * 100 \end{aligned} \quad \text{Equation 5.5}$$

Figure 5.7c shows the loss calculation for the CSU buried detector using equation 5.2. The waveguide loss was calculated to be 13.6 dB/mm for the bare waveguide and 17.4 dB/mm after oil was added to the surface.

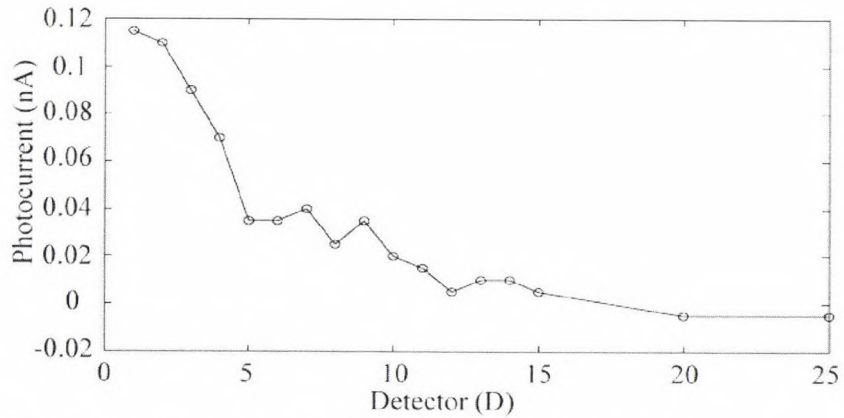


Figure 5.7a: Detector power profile for the CSU buried detector device with nothing added to the waveguide surface.

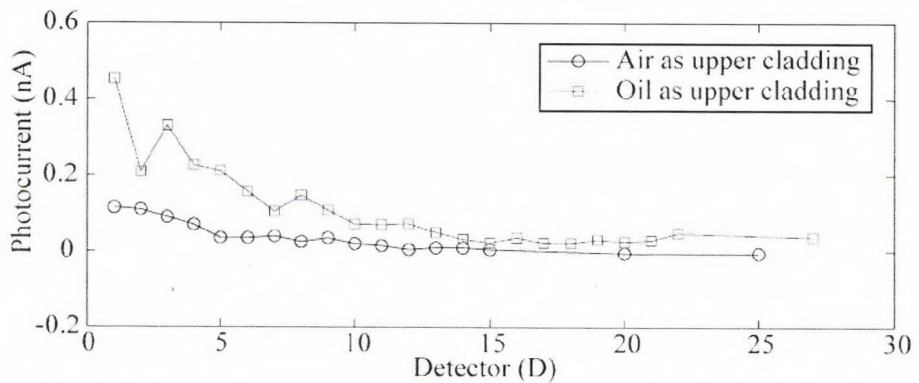


Figure 5.7b: Detector power profile for the CSU device when the upper cladding refractive index is changed using vegetable oil on the waveguide surface

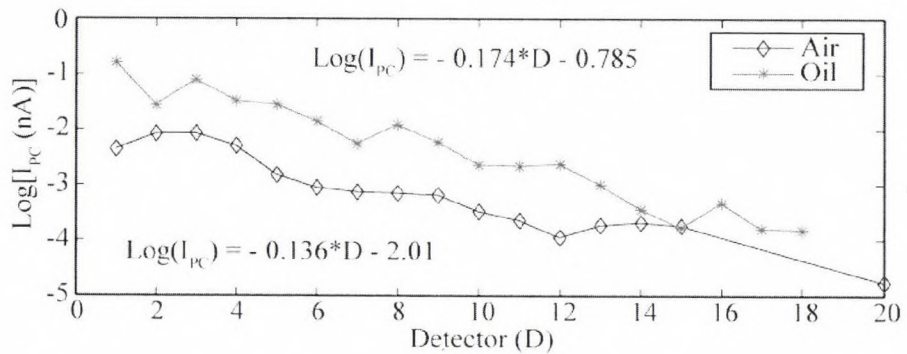


Figure 5.7c: Changing the upper cladding from air to oil affects waveguide loss for the CSU buried detector device. Bare waveguide loss = 13.6 dB/mm, With oil = 17.4 dB/mm. I_{PC} is the photocurrent measured at each detector.

Table 5.1 Etch types used in detector fabrication

Material Etched	Etchant	Etch rate and Notes
Reactive ion sputtered Silicon nitride. N ₂ or NH ₃ as nitrogen source	35 sccm CF ₄ and 10 sccm O ₂ plasma in Micro RIE. Power is 50 watts. Pressure is around 240 mTorr	From experiments on 2/4/05 measuring thickness with ellipsometry in CSU cleanroom: 2.16-2.36 nm/second. Removes poly-silicon isotropically
Silicon nitride chemically vapor-deposited from a gaseous mixture of ammonia and dichlorosilane	HF concentrations from 9 to 49 weight percent and times from 1 to 5 minutes.	$T(A) = 2.55 + 0.65(HF) - 9.3t + 3.2(HF)t$ T = thickness change of nitride film in angstroms HF = Weight percent t = time in minutes “Experimental design applied to the etching of silicon nitride in HF solutions” by Guilinger, T.R.; Kelly, M.J.; Weygandt, W.S.
Reactive ion sputtered Silicon oxide. O ₂ as oxygen source	1: 10 HF: H ₂ O (HF from bottle).	Typically used for stripping oxide
Used to remove silicon oxide	Buffered Oxide Etchant (BOE) or Buffered HF (BHF)	It contains ammonia fluoride that will decompose to make up to fluoric ion consumed during etch process.
Used to remove silicon nitride film	Phosphoric Acid : The etch temperature is 160°C	Will not etch silicon.
Poly-Silicon	A premixed solution, of nitric acid, HF, and DI water, used to etch poly-silicon. 4500 ml DI water 4500 ml Nitric Acid 200 ml HF (49%)	To increase the etch rate, the process temperature can be increased to 50°C. Silicon Etchant will etch silicon oxide, though slowly. http://microlab.eecs.berkeley.edu/labmanual/chap1/1.9.html , or http://microlab.berkeley.edu/labmanual/chap1/JMEMSEtchRates2(2003).pdf
Native oxides	1:25 HF: H ₂ O (HF from bottle).	Used for HF dips to strip native oxide without removing much of other oxides on the wafer.
Oxides	5: 1 buffered hydrofluoric acid (a.k.a. buffered oxide etch, BOE).	Because this solution is buffered, its etch rate does not vary much with use. Best for controlled etching of oxides.
single-crystal silicon	Potassium hydroxide solution at 80°C. Mixed from 1000 g KOH pellets : 2 liters H ₂ O. Solution is self-heating. Let it sit a few hours before using. Pattern with nitride.	Used for anisotropic etching of single-crystal silicon. Attacks (100) and (110) planes much faster than (111) planes.

5.5 Avago detector design

The second design that was implemented was the Avago detector [54]. This detector had the general structure and dimensions shown in figure 5.8. This detector also used polysilicon to form the photodiode to detect the presence and strength of the evanescent field in the lower cladding. It was formed using a series of metal and dielectric deposition steps separated by chemical mechanical polishing steps. This design incorporated discrete detectors that were $9.5 \mu\text{m}$ long and were separated by $0.5 \mu\text{m}$. The cross section of the Avago detectors is shown in figure 5.8a. Three scanning electron micrographs of the detector design are shown in figure 5.8. The micrographs (taken at the CSU Central Instrument Facility) show the 100 nm rib waveguide

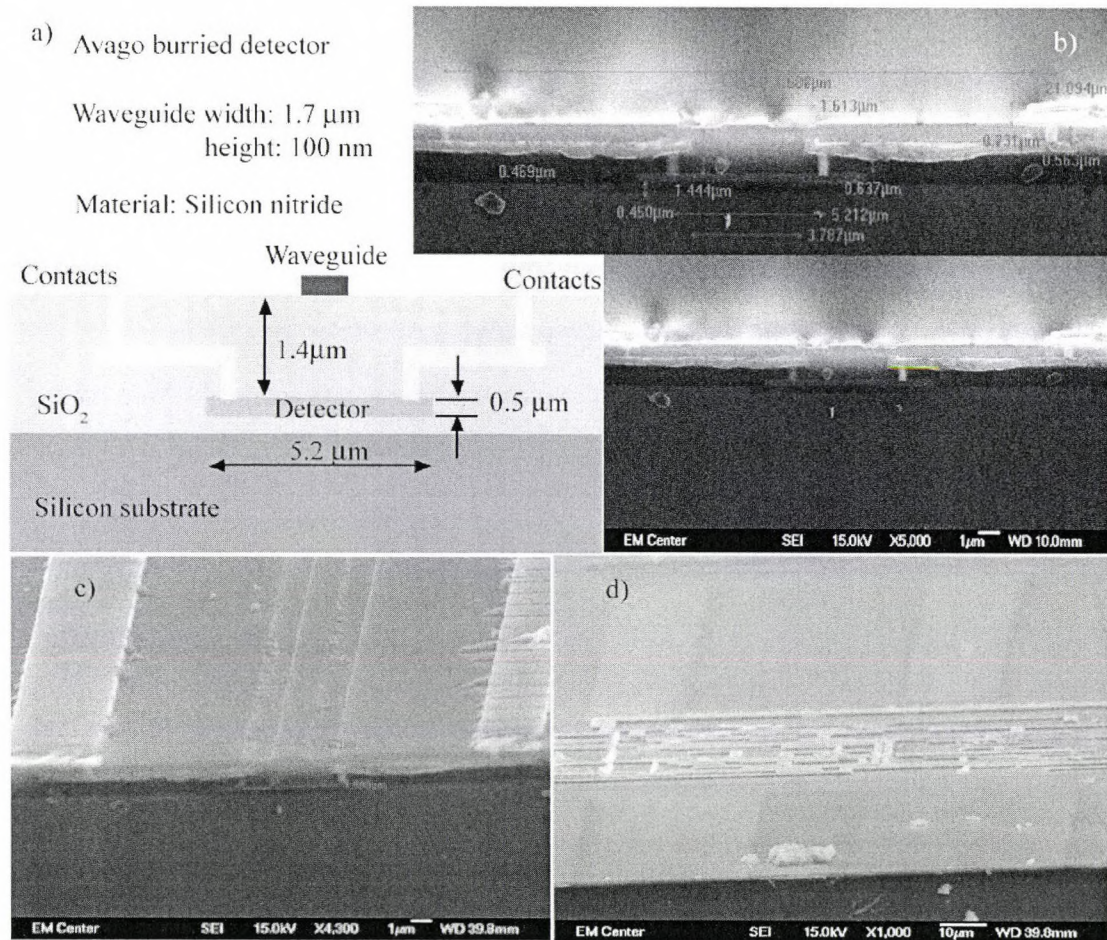


Figure 5.8: a) Avago device cross section with dimensions, b) micrograph of the cross-section of metal connections and polysilicon detector region, c) Top view of the waveguide, and d) decoder circuitry for detector measurement.

made of silicon nitride in the center and the polysilicon detector region below it. On each side of the waveguide, the metal contacts and vias can be seen. The SiO₂ dielectric insulated the detector blocks from each other and the silicon substrate. A top view of the waveguide and detector pads is shown in figure 5.8c. The differences between this detector design and the CSU detector were the smaller, separated detector blocks and the increased spacing between the core of the waveguide and the detectors. Also in the Avago device, the waveguide was a fully etched rib waveguide, which according to simulation and NSOM experimental results, was multimode at 654 nm.

5.6 Results from Avago detector

The response for the detectors was determined for the bare waveguide with air as the upper cladding. The detector response is shown in figure 5.9. For the first four detectors an increased loss rate was observed. This was due to the transient propagation of the high order modes or cladding modes as the light was initially end-fire coupled into the waveguide. The loss rate for the first four detectors was ≈ 37 dB/mm. After the initial loss of leaky modes in the first 300 to 400 μ m of the waveguide, the

propagation loss for the remainder of the waveguide was approximately 8 dB/mm. Detector-to-detector variations in the signal were likely due to scattering from the waveguide and multimode interference. The approximate estimated loss from experimental results for a waveguide of this type with no buried detector array was around 1 dB/mm

with a theoretical calculation predicting a loss of less than 0.05 dB/mm. Theoretical loss was calculated assuming only adsorbition of light in the waveguide material. The increased loss observed in actual waveguides is the result of scattering due to the roughness of the surfaces and

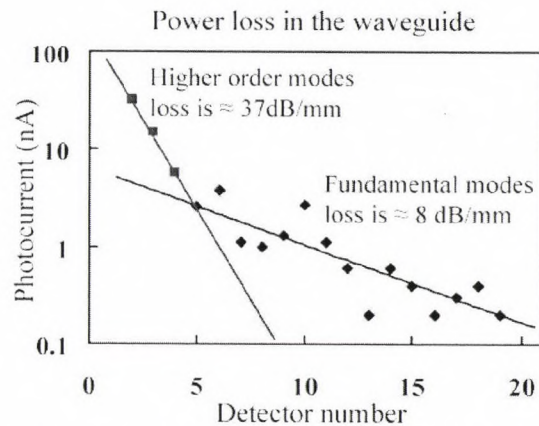


Figure 5.9: Loss characteristics of buried detector device fabricated at Avago

sidewalls of the waveguide. Additional losses were observed in these devices due to power adsorption by the detector elements.

A measurement was done to determine the effect of a refractive index change on the detected power. The detector response of the device was determined in air and then a layer of bovine serum albumin (BSA) was added to the upper surface of the waveguide. BSA is used commonly to block non-specific adsorption

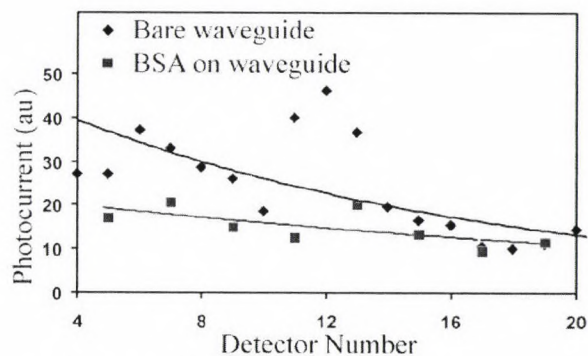


Figure 5.10: Avago sample response to uniform BSA patterning on the surface

of proteins and other molecules on surfaces. The results of the BSA layer addition are shown in figure 5.10. Consistent with the simulation results shown in figure 5.3, the addition of a higher refractive index layer to the waveguide surface shifted the evanescent field distribution and thus reduced the field detected by a buried array. The observed signal after the addition of BSA to the surface decreases, as predicted by the simulation. This result indicated that a buried detector array was able to respond in a significant manner to the addition of a small layer of biological material to the surface of the waveguide.

5.7 Conclusion

Through the laboratory and simulation experiments conducted with these two detector designs it may be concluded that it is feasible to fabricate an integrated local evanescent field detection system on the same chip as the waveguide. The buried detectors were successful in detecting the light and can be used to determine the propagation loss for the waveguide structures. The scatter in the data received from measuring the detector response limited the usefulness of the results in these preliminary studies. However, changes in bulk refractive index and uniform surface films had a measurable effect on the detected power and the propagation losses of the waveguides.

Chapter 6 – Conclusions and Future work

6.1 Introduction

In the course of these studies, a number of important discoveries were made regarding the characteristics of the LEAC sensor. The waveguide geometry for single mode propagation of light and the NSOM and buried detector array profile for light propagation were documented. The observed surface and buried detector light field profiles to different features attached to the surface were determined. Features that were studied included high refractive index features fabricated of the same refractive index as the core, polymer film features of refractive index 1.6, and a quantitative protein immunoassay. Thickness and length of features were varied to determine the size effects on signal. The minimum feature heights and lengths that produced a response were determined using the evanescent field profiles. The minimum feature spacing was found in order to ensure a clear detected signal for each probe region. The challenges associated with attaching proteins to the waveguide surface using PDMS microfluidic channels were determined. Numerical simulations were also used to predict and quantify the expected response of the evanescent field to these features. The simulations were compared with the measured results using NSOM and the buried detector designs. Additional areas for future study and improvement were found and are discussed at the end of this chapter.

6.2 Waveguide design

Several waveguide designs were fabricated to determine the evanescent field surrounding each of the cores. The planar waveguides were formed through the deposition of a silicon nitride film on thermal oxide wafer. The silicon nitride film formed the core material for the planar

waveguide. Thermal oxide on the silicon wafer served as the lower cladding. The waveguides were fabricated using photoresist masking and plasma etching. This masking and etching procedure formed the waveguide to confine the light to a narrow region of the wafer. As seen in figure 6.1, four designs were fabricated in order to determine the surface evanescent field intensity for waveguides of various geometries. The ideal evanescent field intensity for detection of binding events was a uniform field, guided down the core. If multiple modes of light propagation were guided down the core, the observed surface evanescent field intensity varied due to interference between modes. Therefore, a single mode of light propagation was necessary to maintain a uniform field. Light with a wavelength of 654 nm was coupled into the waveguide structures shown in figure 6.1. The surface evanescent field intensity was measured using NSOM. The waveguide geometry shown at the bottom of figure 6.1 was found to be single mode. All the other waveguide structures guided multiple modes using a wavelength of 654 nm. It was determined that the maximum waveguide width for single mode propagation was approximately 3 μm and the maximum etch ridge depth was approximately 20 nm. For films thicker than 100 nm multiple vertical modes were observed and for waveguides wider than 3 μm multiple horizontal modes were observed to propagate in the structure. It may be concluded from these experiments that, for a core refractive index of 1.8, the appropriate geometry for single mode light propagation was a core thickness less than 100 nm, with ridge widths less than 3 μm and ridge heights less than 20 nm.

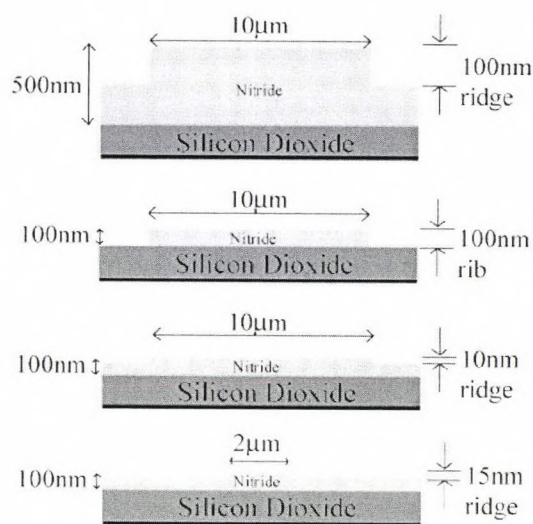


Figure 6.1: Four test waveguide geometries fabricated out of silicon nitride films deposited on thermal oxidized silicon wafer substrate. Top three structures were found to be multimode. The bottom structure was found to guide only a single mode and was the geometry used in the sensor design.

6.3 Evanescent response to core thickness changes

After the determination of the appropriate geometry for a ridge waveguide to achieve single mode light propagation, the evanescent field response to features of various sizes on the core of the waveguide was determined. As a first step in determining evanescent field response, features of the same refractive index as the core were fabricated on the surface of the waveguide. This resulted in a structure that increased the core thickness at specific regions along the waveguide. To form these core thickness changes, a secondary masking procedure was used to mask 10 μm long regions of the core and an additional etching step was added to reduce the thickness of the entire film a few additional nanometers. The evanescent field response to the high refractive index feature on the waveguide is shown in figure 6.2. Light was propagating from left to right, and the topography of the waveguide and the fabricated feature are shown in figure 6.2a. The 2D surface evanescent light intensity is shown in figure 6.2b and a line plot

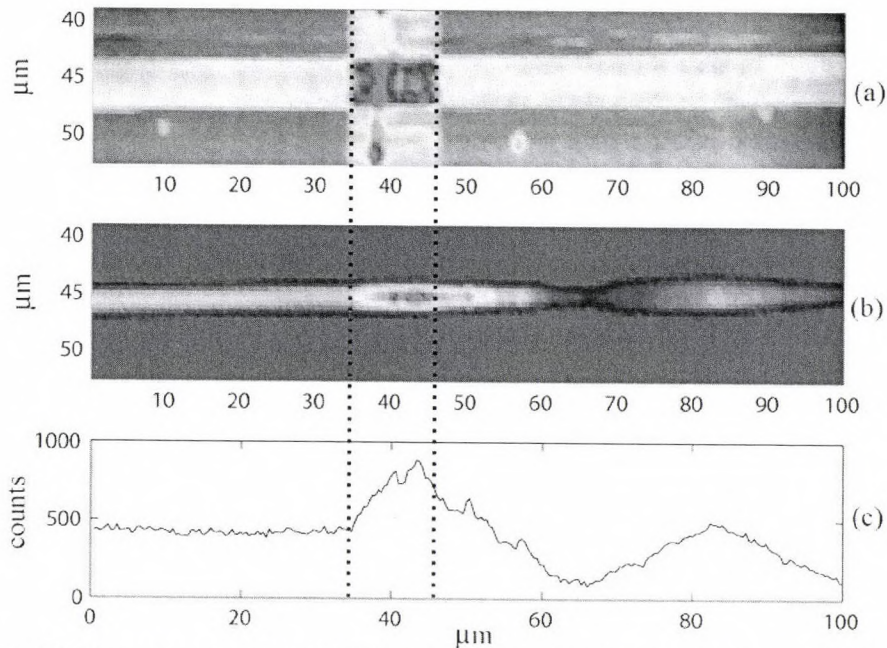


Figure 6.2: Response to a larger high refractive index feature. Light travels from left \rightarrow right. (a) Topography of 4.5 μm wide waveguide with 21 nm etch depth. Feature size is ≈ 13 μm in length and 30 nm thick, (b) Surface light intensity measured with NSOM, (c) Total light measured in photon counts carried in the waveguide after subtracting the background showing a larger increase in light over the feature than was observed for thinner features.

showing the total evanescent field intensity for the whole waveguide is found in figure 6.2c. As observed, the light intensity increased when it reached this high refractive index feature. After the feature, the light intensity oscillated and decayed back to a uniform value. This basic response profile was observed for all high refractive index features fabricated on the core. The oscillation of the light after the feature affected the response from an array of features that were closely placed along the waveguide. This first experiment to determine the response to refractive index changes provided several insights into the design of capture regions. The light intensity shifted in a significant manner in response to a 10 to 20 nm thick layer of material on the core. This thickness range is typical of the size range of several dried layers of proteins or other biological molecules attached to a surface. For these thin features, the surface evanescent field intensity as measured using NSOM increased over the feature. The light exiting the feature oscillated in a decaying manner and returned to a uniform value, indicating the appropriate feature spacing was 100 to 200 μm .

6.4 Evanescent response to patterned polymer features

As a next step in determining the evanescent field response, photoresist was used to pattern surface features on the waveguide core. The use of photoresist film produced a feature that was between 60 and 120 nm. The refractive index of the polymer film was determined to be near 1.6 and since the refractive index of proteins and other biological molecules are assumed to be 1.4 to 1.5, this provided a more realistic refractive index profile than the high index structures studied in chapter 3. The response to features fabricated from photoresist was closer to the expected response to biological materials than the response from core thickness changes. Various lengths and thicknesses of photoresist were patterned on the core of the waveguide and the evanescent field response determined using NSOM. The evanescent field response was observed to decrease as the feature was encountered, as seen in figure 6.3. After the feature, a sharp increase in field intensity was observed and then the field oscillated in a decaying manner before returning to a uniform intensity. For features of this thickness and refractive index, the evanescent

field intensity decreased over the feature because the distance between the NSOM tip and the core of the waveguide increased. The expected response of the light field to a refractive index increase on the core was a shift of power from the lower cladding up into the upper cladding (see figure 6.4). However, the combined effect of increasing the distance between the core and the tip resulted in the observed decrease in intensity over the feature.

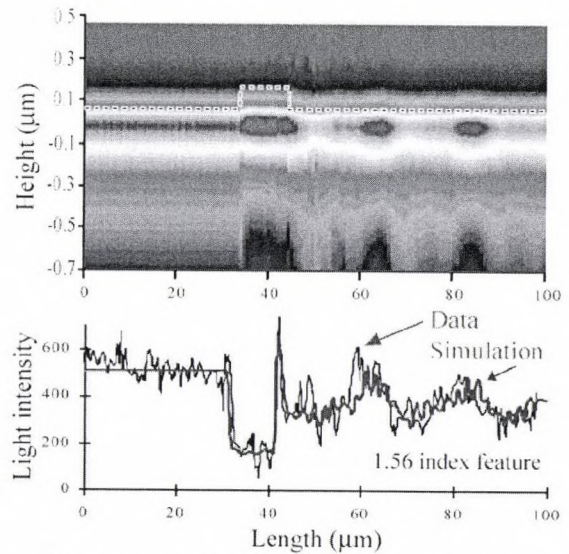


Figure 6.3: BPM light intensity cross section (top) and overlay of NSOM data and BPM as measured on the waveguide surface (bottom).

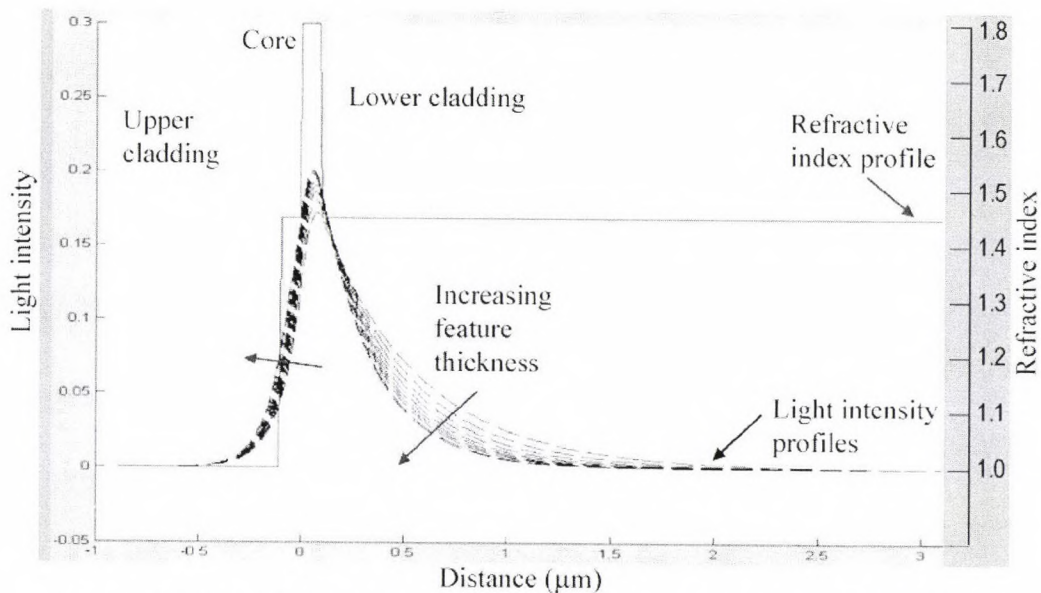


Figure 6.4: Light field shifting as feature thickness increases (BeamPROP) [53]

In the case of these photoresist features, similar to the phenomenon observed for high refractive index features, the oscillations in the evanescent field intensity after the feature impacted the spacing between the features. The analysis of these experimental results indicated several conclusions. To obtain a measurement of the evanescent field response to a feature that is independent of the surrounding features, the spacing between features should be at least 150 to

200 μm . The surface evanescent field was able to respond to features of this thickness range, which is representative of the capture of virus particles. Also, the increased distance between the tip and the core of the waveguide was the dominant effect on field measurement, and resulted in a decrease in observed intensity to these features.

6.5 Quantitative immunoassay

The next step in the development of the sensing device was to determine the response to an immunoassay. As a representative test, a quantitative C-reactive protein immunoassay was carried out on the surface of the waveguide. The immunoassay regions were patterned using PDMS microfluidic channels. The three-channel PDMS network allowed the attachment of anti-CRP to the waveguide surface using the biotin-avidin non-covalent linking mechanism. The three channels contained the same attached antibodies, but each channel was exposed to different concentrations of the CRP analyte. Concentrated (600 $\mu\text{g}/\text{mL}$), dilute (0.6 $\mu\text{g}/\text{mL}$) and zero concentration CRP solutions were added to the microfluidic channels. The 5-layer immunoassay formed biological material features on the waveguide core that, after drying, were measured to be between 12 to 15 nm thick, depending on the CRP concentration. For these relatively thin features, the shift upwards of the evanescent field due to the change in refractive index was expected to be the dominant response as seen in the simulated profiles in figure 6.4. The surface evanescent field intensity and the BPM simulation results to the high and low CRP features are shown in figure 6.5. The evanescent field intensity increased over the feature and was followed by decaying oscillations. This experiment with the immunoassay on the waveguide indicated that the evanescent field response could be used as a quantitative test to determine protein concentration.

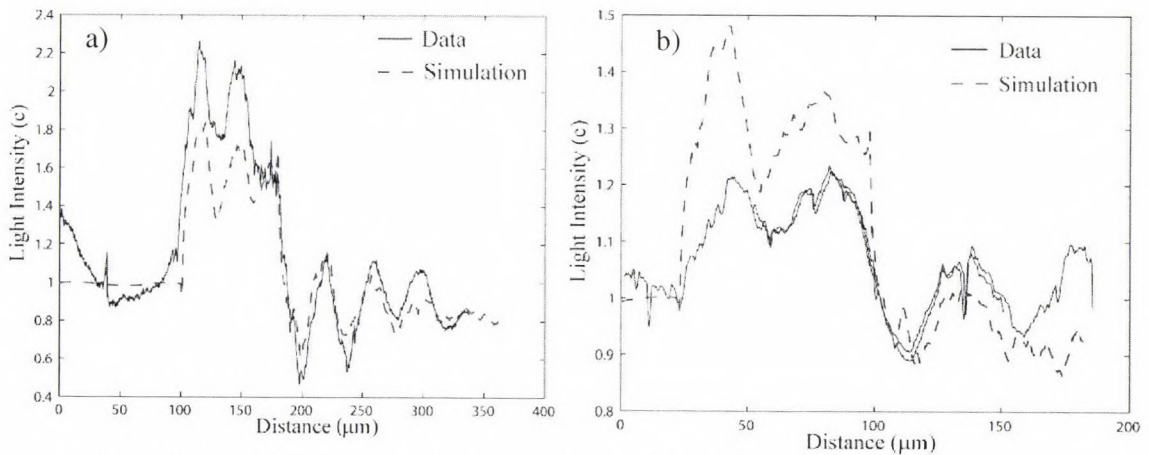


Figure 6.5: Two 75 μm long features on waveguide. Light response results of the features with CRP concentrations of a) 600 $\mu\text{g/ml}$ and b) 0.6 $\mu\text{g/ml}$ respectively

6.6 On-chip evanescent detection

The use of NSOM to determine surface evanescent field intensity was effective, but this detection method had several disadvantages. The instrument was large, needed a connection to a computer, required a large initial monetary investment and the measurement of field intensity was affected by surface topography. A new method of evanescent field detection built on the same waveguide chip may solve several of these problems. An on-chip evanescent field detection method has the advantage of being small, requiring lower amounts of power, and may be fabricated to detect the evanescent field intensity at a constant distance from the waveguide core.

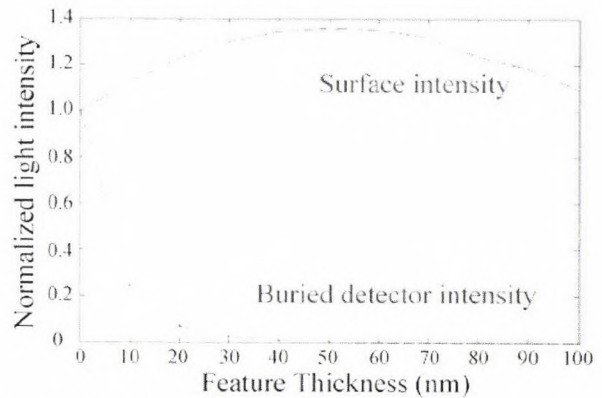


Figure 6.6: BeamPROP simulated NSOM and buried detector response for features of increasing thickness [53].

This buried detector design also has the advantage of not needing to contact the top of the waveguide. This means that a microfluidic device may be placed on a chip surface to allow delivery and mixing of small sample volumes to probe regions patterned on the waveguide core.

Figure 6.5 shows the simulated response from NSOM and a buried array 2 μm away from the core for features of increasing thickness ($n = 1.45$). The response for NSOM was not monotonic due to the effects of surface topography on evanescent field measurement. According to the simulation results shown in figure 6.6, the NSOM response to a feature 20 nm in height would be the same response as a 90 nm feature. The response for a buried detector decreases monotonically for increasing feature thickness. Also, in the range of 0 to 30 nm, which was the typical thickness for immunoassay binding, the sensitivity of the detector was higher than that of the NSOM.

The buried detector was based on using polysilicon to intercept evanescent field light in the lower cladding and convert the light to electrons that were then measured. This photo current response was in the nano-amp range and the current measured at each detector indicated the optical power traveling in the waveguide. The expected response to surface features on the evanescent field is to cause a shift of light out of the lower cladding and reduce the power

detected by the buried detectors. For the Avago detector device, a uniform bovine serum albumin (BSA) film with a thickness of approximately 1.5 nm [52] was deposited to the surface of the waveguide. The photo current response for the detectors was determined before the film patterning, and after, as shown in

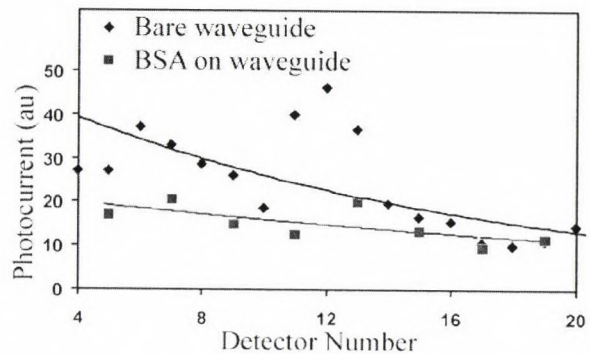


Figure 6.7: Avago sample response to uniform BSA patterning on the surface [53]

figure 6.7. The photocurrent measured for the bare waveguide was, on average, higher than the photo current after the BSA was attached. This indicated that the buried detectors responded to a thin biological film attached to the waveguide core.

6.7 Buried detector improvements

One of the disadvantages of the CSU buried detector design was the continuous detector strip under the length of the waveguide. For this detector geometry, there is the possibility that

current from several detector regions could be collected while only biasing a single pair of contacts. Biasing the surrounding detectors while measuring a detector in the center could reduce the signal transferred between contacts. This would better confine the current flow to be parallel between the contacts and the detectors would measure the power at a more specific area of the detector strip.

The waveguide design for the Avago buried detector could also be improved. The waveguide used was a 100 nm rib waveguide made of silicon nitride. The waveguide should be a 15 nm rib waveguide, 2 to 3 μm wide fabricated out of a film of 80 to 100 nm. Changing the waveguide geometry would result in single mode behavior and the light propagation would be less effected by sidewall roughness. An additional improvement would be to increase the number of buried detector elements, which would improve the ability of the detector array to observe some of the finer details of the evanescent field profile that are seen in NSOM scans. For patterned features of 10 to 40 μm the response would be difficult to determine if the detector size was 10 μm . The minimum detector size is limited by two phenomena. The fabrication techniques are limited in the minimum size of features that can be created. Also, the photocurrent generated by a detector block must be large enough to measure with the current meter. As the size of the detector region is decreased, the evanescent field intercepted by the detector is smaller and the signal from that element decreases.

An additional problem with buried detector devices is the increased absorption of the propagating light. The propagation loss of a waveguide without a detector array is approximately 1 dB/mm. The addition of a buried detector array increases the propagation loss to approximately 8 dB/mm. The waveguide-to-detector distance could be optimized to both reduce propagation losses and receive significant power at each detector. The NSOM tip collects light at each point but does not remove power from anywhere but at the current location of the tip. This is unlike the buried detector array, which removes power at each point along the waveguide regardless of the

biasing of the detector elements. Optimizing the spacing between the core and detector elements as well as the size of the detector elements is necessary for improving the operation of the waveguide.

With a buried detector design, constant background subtraction of the dark current is necessary. The buried detectors are sensitive to the environmental light and the temperature of the device. Optical shielding of the device is necessary to reduce the effect of outside light on the current readings from the detectors. A thermal conductive base attached to the sample may be necessary to maintain the same temperature across the whole waveguide chip. This would maintain uniform optical and electrical properties of the waveguide and detectors as the device is operated.

6.8 Waveguide modifications

Another factor that could be experimented with is the refractive index of the core. If the core was a lower refractive index than 1.8, for the same core thickness, more of the power would be in the evanescent field in the cladding. This would allow the detectors to be placed farther away from the core and still receive the same amount of evanescent field. If more of the power were outside the core, the sensitivity may be enhanced for any binding events that occur in the upper cladding. If the core refractive index were decreased, the core could be made thicker while maintaining the evanescent field penetration depths into the cladding regions. The thicker core region would enhance the coupling efficiency and more light would be launched from the fiber into the rib waveguide.

Any change that increases the optical coupling efficiency between the fiber and the waveguide film would be beneficial. The limitation for the number of probe regions and the device's multianalyte capability is the amount of power that can be guided. Each probe region on the surface of the waveguide causes a small amount of scattering due to the interfaces between the materials that have different refractive indices. Therefore, the more power that can be guided, the larger the number of probe regions that can be patterned on the waveguide. End-fire coupling

requires three-dimensional adjustment in order to align the fiber with the polished facet of the waveguide. Other coupling types may provide more launched power or may reduce the amount of time required for coupling. For example, grating coupling may allow easier fiber alignment by reducing the adjustment that is needed for launching the light into the waveguide but requires fabrication of a grating element on the waveguide chip.

The light used in this device had a wavelength of 654 nm, which is a red visible wavelength. Changing the wavelength of the light launched into the waveguide would be a way to change the mode profile and the evanescent field penetration without changing the waveguide core geometry or refractive index. An example would be a waveguide built out of the 100 nm nitride film and partially etched 20 nm with a width of 3 μm . This waveguide is single mode at 654 nm but it is very near the single mode/multimode boundary. Etched any deeper or any wider and more than one mode would be carried in the structure. If a shorter wavelength of light was coupled into this waveguide, it would be multimode and the evanescent field would penetrate a smaller distance into the cladding regions. A longer wavelength coupled in this waveguide and the waveguide would be single mode and the evanescent field would penetrate farther into the cladding regions than at 654 nm. This phenomenon can be used to have the evanescent field penetration be tuned to only examine a certain amount of the upper cladding without having to redesign the geometry or indexes of the material. Alternatively, several wavelengths can be used in a single device to perform depth profiling of the refractive index changes at multiple distances from the core.

6.9 Device improvements

One of the additional improvements in increasing the area for patterning probe regions is to have multiple active waveguides on the same chip. This could be achieved through splitting of one waveguide or having multiple parallel waveguides (see figure 6.8). The advantage of splitting one waveguide is the light source would only need to be coupled to one central waveguide that would split into an even number of waveguides, which would be used for probe patterning. The

only limitation would be the power needs to be sufficient in each split to detect the field (see figure 6.9). If multiple parallel waveguides were used, enough power would effectively be coupled into each waveguide but alignment might be more difficult. There could be several possible solutions to coupling into multiple

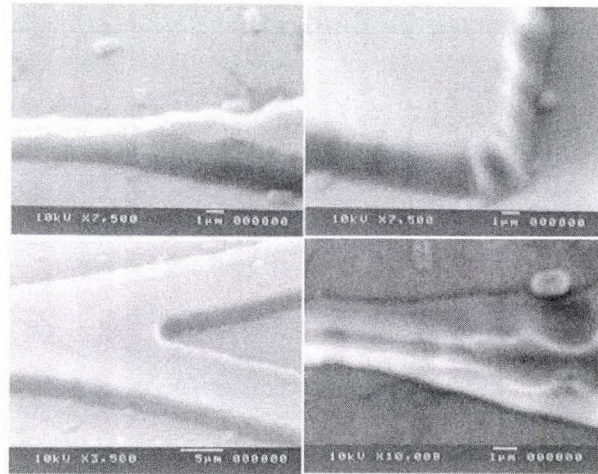


Figure 6.8: SEM Micrographs of photoresist structures for fabricating waveguide splits.

waveguides. The light source could be free to move left and right along a prism coupler with a micro adjustment used to move the light source back and forth to couple light into the waveguide of choice. Or a large diameter light source may be used to launch light into multiple parallel waveguides simultaneously using a tapered coupling design.

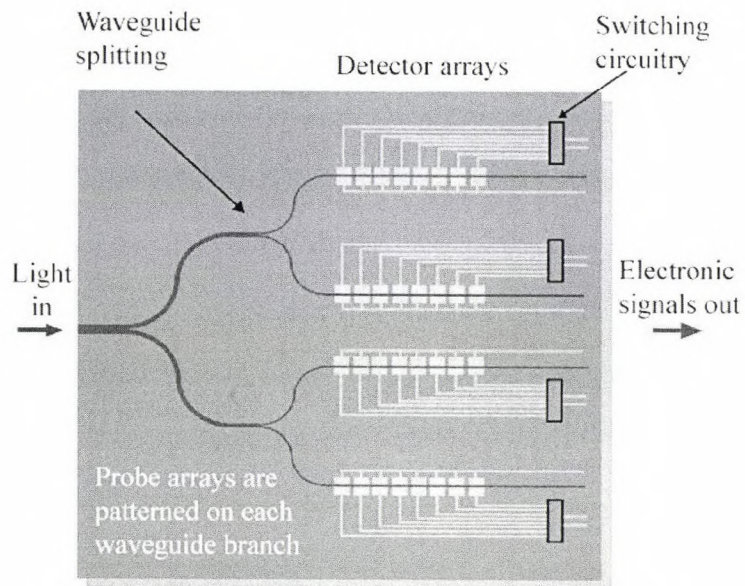


Figure 6.9: Possible device with 4 waveguides using splitting with detector array

6.10 Conclusion

The fabrication of a thin film, planar waveguide that maximizes shifts in the evanescent field for small refractive index changes near the core has been accomplished. The fabrication and preliminary testing of a simple polysilicon buried detector design has been completed. The evanescent fields have been profiled using NSOM and two on-chip detector designs. The evanescent field response to features, both artificially fabricated and self-assembled have been determined with these measurement techniques. The experimental results were compared to BPM simulations and the simulation results agree well with the experimental data. The development and testing of this optical detection method and evanescent field measurement system has indicated that this is a good combination of technology for a sensing device.

6.11 Further experiments

The quantitative immunoassay that was done indicated the evanescent field could be used to detect the concentration of a protein in solution. Signals received from the immunoassay patterns were significantly different from each other and could be correlated with amount of protein binding. However, none of the experiments that were done involved the patterning of probe regions directed against multiple analytes. An additional experiment should be done involving immunoassays for separate analytes on the same waveguide sample. With the NSOM detection technique, measurement of the evanescent field before and after protein binding is not practical. To avoid before and after testing of the evanescent field intensity, control regions must be patterned using probes that are not exposed to the analyte. One or more probe regions should be exposed to buffer only to determine the evanescent field response to the attached probes without any analyte binding. Using this method, only a single measurement would be necessary to determine the response to differing concentrations of analyte. This will also calibrate the differing responses generated by different probes or attachment chemistry. Also an experiment using complex sample milieu is recommended to determine the effects of nonspecific binding on the response from an immunoassay.

In the previous experiments, analyte binding took place completely separate from evanescent field measurement. In the eventual device design, the aqueous sample would be delivered to the waveguide surface using a microfluidic pumping and mixing device. The real-time evanescent field measurement is only possible if a fluid flow cell is present on top of the waveguide. For future work, incorporation of a molded PDMS microfluidic network attached to the waveguide for sample delivery is recommended. The effect of the PDMS material on the operation of the waveguide and detector array should be determined. The response to real-time binding of analyte with the buried detector array while the flow cell is attached should be compared with the results obtained without the PDMS network above the waveguide. The presence of the PDMS material on the waveguide core may increase absorption of light and increase the propagation loss from the waveguide. The flow cell should be designed to minimize contact of the PDMS microfluidic network with the waveguide so the majority of the waveguide is exposed to the sample fluid.

In future experiments involving patterned arrays of probes on the waveguide, the recommended feature size of the capture region is 30 to 40 μm in length. Spacing between features of at least 200 μm is recommended to allow the evanescent field to stabilize after each feature. A stable input field is necessary to determine an accurate power modulation value for each probe region.

References

- [1] Torres-Chavolla, Edith and Evangelyn C. Alocilja, "Aptasensors for detection of microbial and viral pathogens," *Biosensors & Bioelectronics*, Vol 24, Iss 11, pp 3175-3182, 2009.
- [2] Lui, Clarissa, Nathaniel C. Cady and Carl A. Batt, "Nucleic Acid-based Detection of Bacterial Pathogens Using Integrated Microfluidic Platform Systems," *Sensors*, Vol 9, Iss 5, pp 3713-3744, 2009.
- [3] Heller, M.J., "DNA microarray technology: Devices, systems, and applications," *Annual Review of Biomedical Eng.*, Vol 4, pp 129-153, 2002.
- [4] Lemarchand, K., L. Masson, R Brousseau, "Molecular biology and DNA microarray technology for microbial quality monitoring of water," *Critical Reviews in Microbiology*, Vol 30, Iss 3, pp 145-172, 2004.
- [5] Yoo, S.M., K.C. Keum, S.Y. Yoo, J.Y. Choi, K.H. Chang, N.C. Yoo, W.M Yoo, J.M. Kim, D. Lee and S.Y. Lee, "Development of DNA microarray for pathogen detection," *Biotech. and Bioprocess Eng.*, Vol 9, Iss 2, pp 93-99, 2004.
- [6] Hartmann, Michael, Johan Roeraade, Dieter Stoll, Markus F. Templin and Thomas O. Joos, "Protein microarrays for diagnostic assays," *Analytical and Bioanalytical Chem.* Vol 393, Iss 5, pp 1407-1416, 2009.
- [7] Saerens, Dirk, Lieven Huang, Kristien Bonroy, and Serge Muyldermans, "Antibody fragments as probe in biosensor development," *Sensors*, Vol 8, Iss 8, pp 4669-4686, 2008.
- [8] Hou, Chenlu, Amy E. Herr, "Clinically relevant advances in on-chip affinity-based electrophoresis and electrochromatography," *Electrophoresis*, Vol 29, Iss 16, pp 3306-3319, 2008.

- [9] Smith, David S. and Sergei A. Eremin, "Fluorescence polarization immunoassays and related methods for simple, high-throughput screening of small molecules," *Analytical and Bioanalytical Chem.*, Vol 391, Iss 5, pp 1499-1507, 2008.
- [10] Henares, Terence G., Fumio Mizutani and Hideaki Hisamoto, "Current development in microfluidic immunosensing chip," *Analytica Chimica Acta*, Vol 611, Iss 1, pp 17-30, 2008.
- [11] Shankaran, Dhesingh Ravi, K. Vengataj Alabathy Gobi and Norio Miura, "Recent advancements in surface plasmon resonance immunosensors for detection of small molecules of biomedical, food and environmental interest," *Sensors and Actuators B-Chem.*, Vol 121, Iss 1, pp 158-177, 2007.
- [12] Bilitewski U, "Protein-sensing assay formats and devices," *Analytica Chimica Acta*, Vol 568, Iss 1-2, pp 232-247, 2006.
- [13] Marquette C.A. and L.J. Blum, "State of the art and recent advances in immunoanalytical systems," *Biosensors & Bioelectronics*, Vol 21, Iss 8, pp 1424-1433, 2006.
- [14] Ekins, Roger P., "Ligand assays: from electrophoresis to miniaturized microarrays," *Clinical Chemistry* Vol 44, Iss 9, pp 2015-2030, 1998.
- [15] Harley, John, Donald Klein "Action of Antibodies," Lansing Prescott, *Microbiology*, fifth ed, pp 756-758, 2002.
- [16] Rowe, Chris A., Leonard M. Tender, Mark J. Feldstein, Joel P. Golden, Stephanie B. Scruggs, Brian D. MacCraith, John J. Cras, and Frances S. Ligler, "Array Biosensor for Simultaneous Identification of Bacterial, Viral, and Protein Analytes," *Anal. Chem.*, Vol 71, pp 3846-3852, 1999.
- [17] Ostroff, Rachel, Anna Ettinger, Helen La, Marynette Rihanek, Leora Zalman, James Meador, III, Amy K. Patick, Steve Worland and Barry Polisky, "Rapid multiserotype detection of human rhinoviruses on optically coated silicon surfaces," *Journal of Clinical Virology*, Vol 21, Iss 2, pp 105-117, 2001.

- [18] Weber, Bernard, Mahin Moshtaghi-Boronjeni, Michael Brunner, Wolfgang Preiser, Markus Breiner and Hans Wilhelm Doerr, "Evaluation of the reliability of 6 current anti-HIV-1/HIV-2 enzyme immunoassays," *Journal of Virological Methods*, Vol 55, Iss 1, pp 97-104, 1995.
- [19] Zymed Products: ELISA Kits, www.zymed.com/pindex/index80.html, November 2003.
- [20] Enzyme-Linked Immunosorbant Assay, http://vtpb-www.cvm.tamu.edu/vtpb/vet_micro/serology/elisa/, November 2003.
- [21] Harley, John and Donald Klein, "Antigens and the Antibody Binding Mechanism," Lansing Prescott, *Microbiology*, fifth ed, pp 731-744, 2002.
- [22] "ELISA Test Kits for Hormones, Steroids, Eicosanoids, and Cyclic Nucleotides," <http://www.neogen.com/pdf/research5.pdf>, November 2003.
- [23] Cho, Eun Jeong, Zunyu Tao, Elizabeth C. Tehan, and Frank V. Bright "Multianalyte Pin-Printed Biosensor Arrays Based on Protein-Doped Xerogels," *Anal. Chem.*, Vol 74, 6177-6184, 2002.
- [24] Liu, X., W. Farmerier, S. Schuster, W. H. Tan, "Molecular beacons for DNA biosensors with micrometer to submicrometer dimensions," *Anal. Biochem.*, Vol 283, Iss 1, pp 56-63, 2000.
- [25] Christodoulides, N., Tran, M., Floriano, P. N., Rodriguez, M., Goodey, A., Ali, M., Neikirk, D., and J. T. McDevitt, "A microchip-based multianalyte assay system for the assessment of cardiac risk," *Anal. Chem.*, Vol 74, Iss 13, pp 3030-3036, 2002.
- [26] Pease, Mark D., Lisa Shriver-Lake, and Francis Ligler, "Adaptation of a Fiber-Optic Biosensor for Use in Environmental Monitoring," *Biosensor and Chemical Sensor Technology*, edited by Kim R. Rogers, Ashok Mulchandani, and Weichang Zhou, pp 33-43, 1995.
- [27] Hunsperger, Robert G., "Integrated Optics: Theory and Technology," 5th ed, 2002.

- [28] "Handbook of Optical Fibre Sensing Technology", Ed Jose Miguel Lopez-Higuera, Wiley, 2002.
- [29] Rowe, C.A., S.B. Scruggs, M.J. Feldstein, J.P. Golden, and F.S. Ligler, "An array immunosensor for simultaneous detection of clinical analytes," *Analytical Chemistry*, Vol 71, pp 433-439, 1999.
- [30] Rowe, C.A., L.M. Tender, M.J. Feldstein, J.P. Golden, S.B. Scruggs, B.D. MacCraith, J.J. Crass and F. Ligler, "Array biosensor for simultaneous identification of bacterial, viral, and protein analytes," *Analytical Chemistry*, Vol 71, Iss 17, pp 3846-3852, 1999 .
- [31] Rowe-Taitt, C.A., Hazzard, J.W., Hoffman, K.E., Cras, J.J., Golden, J.P., Ligler, F.S., "Simultaneous detection of six biohazardous agents using a planar waveguide array biosensor," *Biosens. Bioelectron.* Vol 15, Iss 11-12, pp 579-589, 2000.
- [32] Chang-Yen, D. A., Gale, B. K., "Design, fabrication, and packaging of a practical multianalyte-capable optical biosensor," *Journal of Microlithography Microfabrication and Microsystems*, Vol 5, Iss 2, pp 8, 2006.
- [33] Ostroff, R.M., D. Hopkins, A.B. Haerberli, W. Baouchi, and B. Polisky, "Thin film biosensor for rapid visual detection of nucleic acid targets," *Clinical Chemistry*, pp 1659-1644, 1999.
- [34] Borrebaeck, C.A.K., "Antibodies in diagnostics – from immunoassays to protein chips," *Immunology Today*, Vol 21, Iss. 8, pp 379-382, 2000.
- [35] Huntington, S. T. and F. Ladouceur, "Evanescent fields - Direct measurement, modeling, and application," *Microscopy Research and Technique*, Vol 70, Iss 3, pp 181-183, 2007.
- [36] Plowman, T.E., S.S. Saavedra, and W.M. Reichert, "Planar integrated optical methods for examining thin films and their surface adlayers," *Biomaterials* Vol 19, pp 341-355, 1998.
- [37] Bernini, R., N. Cennamo, A. Minardo, and L. Zeni, "Planar waveguides for fluorescence-based biosensing: Optimization and analysis," *IEEE Sensors Journal*, Vol 6, Iss 5, pp 1218-1226, 2006.

- [38] Oudshoorn, R.G.C., R.P.H. Kooyman, and J. Greve, "Refractive index and layer thickness of an adsorbing protein as reporters of monolayer formation," *Thin Solid Films*, Vol 284, pp 836-840, 1996.
- [39] Yuan, G.W., M.D. Stephens, D.S. Dandy, and K.L. Lear, "Novel local evanescent field detection waveguide multianalyte biosensor," *SPIE Proc.*, Vol. 5557, pp 140–146, 2004.
- [40] Yuan, G.W., M.D. Stephens, D.S. Dandy, and K.L. Lear, "Direct Imaging of Transient Interference in a Single-Mode Waveguide Using Near-Field Scanning Optical Microscopy," *IEEE Photonics Technology Letters*, Vol. 17, No. 11, pp 2382-2384, 2005.
- [41] Benesch, J., A. Askendal, and P. Tengvall, "The determination of thickness and surface mass density of mesothick immunoprecipitate layers by null ellipsometry and protein (125)iodine labeling," *J. Colloid Interface Sci.*, Vol 249, pp 84–90, 2002.
- [42] Jung, L.S., C.T. Campbell, T.M. Chinowsky, M.N. Mar, and S.S. Yee, "Quantitative interpretation of the response of surface Plasmon resonance sensors to adsorbed films" *Langmuir*. Vol 14, pp 5636–5648, 1998.
- [43] Voros, Janos, "The Density and Refractive Index of Adsorbing Protein Layers," *Biophysical Journal*, Volume 87, pp 553–561, 2004.
- [44] Bernard, A., B. Michel and E. Delamarche, "Micromosaic immunoassays," *Analytical Chemistry* vol 73, pp 8-12 2001.
- [45] Juncker, D., B. Michel, P. Hunziker and E. Delamarche, "Simultaneous detection of C-reactive protein and other cardiac markers in human plasma using micromosaic immunoassays and self-regulating microfluidic networks," *Biosensors & Bioelectronics* vol 19, pp 1193-1202, 2004.
- [46] Delamarche, E., D. Juncker and H. Schmid, "Microfluidics for processing surfaces and miniaturizing biological assays," *Advanced Materials*, vol 17, pp 2911-2933, 2005.

- [47] Delamarche, E., A. Bernard, H. Schmid, B. Michel, H. Biebuyck, "Patterned delivery of immunoglobulins to surfaces using microfluidic networks," *Science*, vol 276, pp 779-781, 1997.
- [48] Delamarche, E., A. Bernard, H. Schmid, A. Bietsch, B. Michel, H. Biebuyck, "Microfluidic networks for chemical patterning of substrate: Design and application to bioassays," *Journal of the American Chemical Society*, vol 120, pp 500-508, 1998.
- [49] Chiu, D. T., N.L. Jeon, S. Huang, R.S. Kane, C.J. Wargo, I.S. Choi, D.E. Ingber and G.M. Whitesides, "Patterned deposition of cells and proteins onto surfaces by using three-dimensional microfluidic systems," *Proceedings of the National Academy of Sciences of the United States of America*, vol 97, pp 2408-2413, 2000.
- [50] Kane, R. S., S. Takayama, E. Ostuni, D.E. Ingber, and G.M. Whitesides, "Patterning proteins and cells using soft lithography," *Biomaterials*, vol 20, pp 2363-2376, 1999.
- [51] Yan, Rongjin, G. Yuan, M. D. Stephens, X. He, C. S. Henry, D. S. Dandy and K. L. Lear, "Evanescent field response to immunoassay layer thickness on planar waveguides," *App. Phy. Let.* Vol 93, Iss 10, article number 101110, 2008.
- [52] He, Xinya, David S. Dandy and Charles S. Henry, "Microfluidic protein patterning on silicon nitride using solvent-extracted poly(dimethylsiloxane) channels," *Sensors and Actuators B-Chem.*, Vol 129, Iss 2, pp 811-817, 2008.
- [53] Yan, Rongjin, S. P. Mestas, G. Yuan, R. Safaisini, D. S. Dandy, and Kevin L. Lear, "Label-free silicon photonic biosensor system with integrated detector array," *Lab on a Chip*, Vol 9, Iss 15, pp 2163-2168, 2009.
- [54] "Hamamatsu silicon photodiodes series S2386 for visible to IR, general-purpose photometry," Hamamatsu Photonics K.K., Solid State Division, Hamamatsu Corporation 360 Foothill Road, PO Box 6910, Bridgewater, NJ, 08807, USA, 2009.

- [55] Yuan, G.W., R. Pownall, P. Nikkel, C. Thangaraj, T. W. Chen, and K. L. Lear, "Characterization of CMOS compatible waveguide-coupled leaky-mode photodetectors," *IEEE Photon. Technol. Lett.*, vol. 18, no.15, pp 1657–1659, 2006.
- [56] Laghla, Y., E. Scheid, H. Vergnes, and J. P. Couderc, "Electronic properties and microstructure of undoped, and B- or P-doped polysilicon deposited by LPCVD," *Solar Energy Mater. Solar Cells*, vol. 48, pp. 303–314, 1997.
- [57] Poenar, D. P., and R. F. Wolffenbuttel, "Optical properties of thin-film silicon-compatible materials," *Appl. Opt.*, vol. 36, pp. 5122–5128, 1997.
- [58] Pownall, R., G.W. Yuan, W. Chen, P. Nikkel, and K.L. Lear, "Geometry Dependence of CMOS-Compatible, Polysilicon, Leaky-Mode Photodetectors," *IEEE Photon. Technol. Lett.*, Vol 19, NO. 7, 2007.

Appendix A: Cleanroom Procedures

A.1 Lithography for waveguide fabrication

The photoresist procedures used to mask the silicon nitride surface to form the waveguides used are as follows:

- 1) The wafer surface was cleaned with a series of washing steps in a laminar flow hood to remove any polar and non-polar contaminants. First the sample was cleaned with acetone. A small amount of acetone was allowed to remain to wet the sample surface and methanol was used to rinse the acetone away. While the sample was still wet with methanol, deionized water was used to remove any remaining soluble contaminants and any organic solvents. The sample was then dried using a jet of compressed nitrogen.
- 2) The sample was then heated on a hot plate set to 120°C for at least 2 min to completely dehydrate the sample.
- 3) The sample was then removed from the hot plate and allowed to cool and placed on the vacuum chuck of a spin-coating device. The speed of the spin coater was set to the appropriate setting. After the speed was set the sample was allowed to return to rest and photoresist was pipetted onto the sample surface.
- 4) The spin coater was activated for 30 s or until the photoresist had reached a uniform thickness across the width of the sample.
- 5) The sample was then removed from the spincoater and placed on a hot plate at 95°C for 2 min. The sample was then removed from the hot plate and allowed to sit for 5-30 min to allow for water diffusion into the photoresist film. Water is necessary for the reaction with UV light in the exposure process. For thicker photoresist films the rest time is longer to allow complete diffusion of water into the film. In some cases, the photoresist films were stored in deionized water to increase the water penetration into the film.

- 6) The sample is then dried and in the cases of photoresist that forms an edge bead, the edges of the sample were cleaned using a razor to allow the mask to properly contact the photoresist surface. The intensity of the mask aligner lamp is determined to calibrate the time required for exposure using a Karl Suss portable UV intensity meter Model 1000. The sample is then placed in the mask aligner (Karl Suss KSM MJB3) and adjusted to place the exposed regions in the correct area. The sample is then brought into contact with the mask and the lamp activated to expose the photoresist.
- 7) The sample is then removed from the mask aligner to develop the photoresist. A small amount of the appropriate developer is added to an open sample container. The sample is then added to the developer solution and the developer solution is swirled to wash away the developing photoresist. When the sample is observed to clear and developing resist is no longer observed, the sample is removed and the developer removed from the sample using deionized water. Usual developing times for a 1 to 2 μm thick photoresist film are 10 to 30 s.
- 8) The photoresist features are then examined using an optical microscope to determine if the mask features were reproduced successfully.

The photoresist used primarily for the fabrication of waveguides was the Rohm and Haas Microposit Shipley 1818 positive photoresist. A spin speed of 4000 to 5000 rpm produced a thickness of S1818 that was approximately 2 μm . The dose of light required to expose S1818 was 150 mJ/cm^2 at 405 nm. For the Karl Suss mask aligner used this indicated an exposure time of approximately 10 to 20 s depending on variations in the lamp power output. The developer used for this photoresist was AZ400K diluted in a 1:4 mixture of developer:water.

There were several factors that effected the probability of success of patterning features on the samples. The photoresist should be used before its expiration date. Older photoresist was observed to have inconsistent exposure and developing properties, which result in photoresist

features that have widths inconsistent with the mask. Care must be taken also with developing times. When observing the developing photoresist films the tendency is to allow the film to sit in the developing solution too long. If the sample is over developed, photoresist features may completely detach from the sample or be dissolved away. In some cases, to allow the narrow features to develop correctly, the samples were only exposed to the developing solution for 4 to 5 seconds.

A.2 Micro RIE Etching

In order to fabricate the waveguides once the appropriate lithography has been accomplished on the sample, the samples are placed in a Technics MICRO-RIE to etch the silicon nitride film. The procedure used to etch the film is as follows:

- 1) With the sample chamber empty the vacuum pump is turned on and the chamber is pumped down to < 100 mTorr.
- 2) The etching gasses are turned on and the flow rates for each are set using the mass flow control knobs. The etchant used in etching silicon nitride is CF_4 plasma. In addition to CF_4 , O_2 is also added to remove any organic contamination or CF_4 polymerization deposition on the photoresist during etching.
- 3) The plasma power is turned on and adjusted to the appropriate level. The etch rate of the silicon nitride increases as the plasma power is increased. A power of 50 watts was chosen to provide an etch rate on the order of a few nanometers of nitride etched per second.
- 4) Plasma power and gas flow rates are turned off and the sample chamber pressurized to allow samples to be placed inside the reactive ion etch chamber. Samples to be etched are surrounded by dummy wafer samples and are secured down using tape. The etch rate across the width of the sample was observed to be more uniform if the sample was surrounded by scrap wafer samples of the same height as the sample.

- 5) The chamber was closed and the vacuum pump was started and allowed to pump down until the chamber reaches a pressure < 100 mTorr.
- 6) The gasses are then turned on and the flow rates are observed until they reach a uniform value. Any additional flow rate adjustments are done before the power is activated. In some cases, an oxygen plasma etch was done to remove any surface organic contamination before the CF_4 plasma etch. In order to etch the nitride for the fabrication of waveguides, a flow rate of 40 sccm of CF_4 and 10 sccm of O_2 was used. Using a power of 50 watts, the usual etch time was between 7 and 10 s to form waveguide ridges. If a rib geometry was required the etch time was extended to remove all the silicon nitride from the sample surface.
- 7) The etching chamber was then pressured and the samples removed and waveguides were fabricated as described in chapter 2.

Appendix B: Matlab Code

B.1 Data plotting and background subtraction using Matlab

```
Topo1 = [...]; % 256 by 256 topography data array from the NSOM
ZScalefactor = 0.000305180437862873;
ZOffset = 140;
Topo1 = (Topo1 + ZOffset) * ZScalefactor;

Light1 = [...]; % 256 by 256 light intensity data array from the NSOM

for i=1:256
    Light1(i,1)=Light1(i,2);
end

%Flip the images so light goes left -> right
Topo=Topo1;
Light=Light1;
for c=1:256
    Light(:,c)=Light(:,257-c);
    Topo(:,c)=Topo(:,257-c);
end

% Mean Column value with background subtraction
a=90;
b=170;
for c=1:256
    top(c)= mean(Light1(a-20:a,c));
    mid(c)= mean(Light1(a:b,c));
    bottom(c)= mean(Light1(b:b+20,c));
```

```

SumLight1(c)= mid(c) -(top(c)+ bottom(c))/2;

ZScalefactor = 2;

ZOffset = -0.5;

% Z Units = counts

SumLight1(c)= (SumLight1(c) + ZOffset) * ZScalefactor;

SumTopol(c)=mean(Topol(a:b,c));

end

x=(1:256)*(100/256);
y=(a:b)*(40/256);

figure (1)

subplot(4,1,1), pcolor(x,y,Topol(a:b,:)),axis ij, shading
interp,ylabel('um')

subplot(4,1,2), pcolor(x,y,Light1(a:b,:)),axis ij, shading
interp,ylabel('um')

subplot(4,1,3), plot(x,SumLight1),ylabel('Counts'), xlabel('um')

subplot(4,1,4), plot(x,SumTopol),ylabel('um'), xlabel('um')

```

B.2 Power modulation calculation code

```

% Calculation of the pattern thickness

Feature_Start=35;

Feature_Stop=75;

Fs=round(Feature_Start/100*256);

Fe=round(Feature_Stop/100*256);

Before_start=75;

Before_end=100;

Bs=round(Before_start/100*256);

```

```

Be=round(Before_end/100*256);
Thick1=(mean(SumTopol(Fs:Fe))-mean(SumTopol(Bs:Be)))*1000;
fprintf('Thickness of pattern 1 is %-.2f nm\n',Thick1)

% Calculation of power modulation
Feature_Start=35;
Feature_Stop=75;
Before_start=1;
Before_end=35;
Fs=round(Feature_Start/100*256);
Fe=round(Feature_Stop/100*256);
Bs=round(Before_start/100*256);
Be=round(Before_end/100*256);
DP1=abs((mean(SumLight1(Fs:Fe))-
mean(SumLight1(Bs:Be)))/mean(SumLight1(Bs:Be)))*100;
fprintf('The power modulation is %.1f %%\n',DP1)

```

B.3 Noise and S/N calculation code

```

% Calculation of noise on the input power signal
% Definition of RMS Noise:
%     defined as the square root of the absolute value of the sum of
%     variances from the signal region
Signal_Start=60; % starting X-axis location of input power
Signal_End=75; % ending X-axis location of input power
Ss=round(Signal_Start*(256/100)); % column location of start
Se=round(Signal_End*(256/100)); % Column location of end
Avg=mean(SumLight1(Ss:Se)); % Average light input signal

```

```

% variance of a random variable or distribution is the expected square
% deviation of that variable from its expected value or mean
for i=Ss:Se
    Variance(i)=(SumLight1(i)-Avg)^2; % array of variances
end
Variance=mean(Variance); % Variance of the input power
RMS1=sqrt(abs(Variance)) % RMS noise of the input power in counts
% Signal to noise ratio is defined as the signal or in this case the
% non normalized power modulation divided by the RMS noise level
SbyN=abs((mean(SumLight1(Fs:Fe))-mean(SumLight1(Bs:Fb)))/RMS1);
fprintf('The S/N is %.2f\n',SbyN)

```

B.4 Calculation of limit of detection

```

% Limit of detection calculation
H0=Thick1; % Feature height in nm
Xbar=mean(SumLight1(Bs:Be)) % Average light input signal
Xf=mean(SumLight1(Fs:Fe)) % Average signal inside feature
signal=Xf-Xbar % Non normalized signal
k=0.95; % Confidence factor
sb=std(SumLight1(Ss:Se)) % standard deviation of blank measurements
XL=abs(H0*(k*sb)/(Xf-Xbar)); % Height in nm corresponding to the limit
of detection
fprintf('The thickness corresponding to the LOD is %-.3g nm.\n\n',XL)

% Limit of detection calculation for CRP immunoassay with
% concentration calculated.
H0=Thick2; % Feature height in nm
C0=0.6; % Pattern concentration in ug/mL

```

```

Xbar=mean(SumLight2(Bs:Be)) % Average light input signal
Xf=mean(SumLight2(Fs:Fe)) % Average signal inside feature
signal=Xf-Xbar % Non normalized signal
k=0.95; % Confidence factor
sb=std(SumLight2(Ss:Se)) % standard deviation of blank measurements
XL=abs(H0*(k*sb)/(Xf-Xbar)); % Height in nm corresponding to the limit
of detection
fprintf('The thickness corresponding to the LOD is %-.3g nm.\n',XL)
% concentration corresponding to the limit of detection
C=abs(C0*(k*sb)/((Xf-Xbar)-(Xf-Xbar)*DP1/DP2)); % Signal from blank
subtracted
fprintf('The concentration corresponding to the LOD is %-.3g
ug/mL.\n\n',C)

```